National Technical University of Athens
School of Mechanical Engineering
Fluids Section
Parallel CFD & Optimization Unit

Application of the Continuous Adjoint Method for the Aerodynamic Optimization of a Passenger Car

Diploma Thesis

Panagiotis Koutsantonis

Advisor:

Kyriakos C. Giannakoglou, Professor NTUA

Athens, February 2018

National Technical University of Athens
School of Mechanical Engineering
Fluids Section
Parallel CFD & Optimization Unit

Application of the Continuous Adjoint Method for the Aerodynamic Optimization of a Passenger Car

Diploma Thesis

Panagiotis Koutsantonis

Advisor: Kyriakos C. Giannakoglou, Professor NTUA

Athens, February 2018

Abstract

This diploma thesis presents the application of the continuous adjoint method developed by the Parallel CFD & Optimization Unit (PCOpt/NTUA) of the School of Mechanical Engineering of the National Technical University of Athens, integrated in the OpenFOAM® environment, to the aerodynamic optimization of a Toyota passenger car. Aerodynamic drag is one of the major energy loss sources in vehicles today and its minimization is a primary target in the automotive industry. With gas emission regulations becoming stricter, along with the emerging electric, hybrid and hydrogen vehicles, the reduction of energy loss is of key significance for vehicle development.

In order to go through with the aerodynamic optimization of the vehicle i.e. the minimization of its drag coefficient, an analysis of the external flow development and structure is necessary. This comes down to the use of Computational Fluid Dynamics for the prediction of the velocity, pressure and turbulence fields around the surface of the vehicle, also known as the primal or flow problem. For this study, three different turbulence models are used; the $k-\epsilon$, $k-\omega$ SST and the Spalart-Allmaras one. The resulting flow fields from the three models are compared and validated with wind tunnel measurements. The ability of each turbulence model to correctly predict important features of the flow, such as flow separation and

reattachment is discussed.

The primal flow fields obtained from each model are used as an input for the solution of the adjoint equations. This yields the adjoint flow field, i.e. the adjoint pressure and velocity fields around the vehicle which are, in turn, used for the computation of sensitivity derivatives. The ability of the adjoint method to correctly compute the required sensitivities in a timely fashion is what makes it stand out. In drag minimization problems, the sensitivity derivatives are the derivatives of the drag force w.r.t. the surface normal displacement of the vehicle's outer surface points. Shape morphing of the geometry in the direction provided by the sensitivity derivatives will lead to the optimization of the vehicle's shape, according to the selected objective function, in this case the drag coefficient. A colorful representation of the surface sensitivities on the vehicle, also referred to as the sensitivity map, is provided. Also, the comparison of the three sensitivity maps resulting from the three primal solutions from the $k - \epsilon$, the $k - \omega$ SST and the Spalart-Allmaras models is carried out.

Finally, the sensitivity derivatives are used as an input to the automatic shape morphing and optimization software developed by the PCOpt/NTUA, which utilizes volumetric B-Splines to perform the morphing of the geometry. Convergence and stability issues of the primal and adjoint simulations are also addressed.

The major part of this diploma thesis was carried out in the premises of Toyota Motor Europe (TME) in Brussels, Belgium, during an 8 month long internship that took place from May until December 2017. On behalf of TME, the Industrial Advisor was Mr A. Delacroix.

Acknowledgements

First and foremost, I would like to express my deep gratitude to my professor, Kyriakos C. Giannakoglou for placing his trust in me and giving me the unique opportunity to take up this diploma thesis. It has been an experience of utmost interest and value for me. His guidance, advice and most of all his corrections were a life lesson for me.

I would also like to genuinely thank my industrial advisor, Mr. Antoine Delacroix. Throughout the time I spent working with him at Toyota Motor Europe, where major part of this diploma thesis was carried out, his advice, his coaching and his guidance taught me a lot. I am grateful for the rare opportunities I was given during my stay at TME. I would also like to thank my manager, Mr. Honda Masahide for guiding and assisting me throughout my work.

I would also like to deeply thank all the members of the Parallel CFD & Optimization Unit of NTUA. Most of all I would like to thank Dr. E. M. Papoutsis-Kiachagias for his continuous support and guidance, Kostas Gkaragkounis for his valuable lessons and precious help before and during the composition of this thesis and, finally, Kostas Samouchos for believing in me. Without them i would not have had the opportunity to take up and complete this diploma thesis.

My work at TME would have been much harder without the help of Mr. Tomoya Shinoda, and for this I would like to wholeheartedly thank him.

I would also like to express my gratitude to the engineers Aristotelis Iordanidis, Nikolaos Christodoulou and Vangelis Skaperdas of BETA CAE Systems for their support throughout my work at TME.

The completion of this diploma thesis also signals the completion of my studies at the National Technical University of Athens. At this point I would like to express my sincere gratitude to my friend Anastasios Papageorgiou without whom I would not have made it here. I would also like to thank my dear friends from my University and the infamous ”Omikron office” who helped me start and finish this work.

Last but not least I would like to thank my family for being here.

Acronyms

NTUA	National Technical University of Athens
PCopt	Parallel CFD & Optimization Unit
TME	Toyota Motor Europe
CFD	Computational Fluid Dynamics
CAD	Computer Aided Design
OpenFOAM	Open Field Operation And Manipulation
PDE	Partial Differential Equation
CPU	Central Processing Unit
GPU	Graphics Processing Unit
EFS	Equivalent Flow Solution
FD	Finite Differences
FAE	Field Adjoint Equation
ATC	Adjoint Transpose Convection
RANS	Reynolds-Averaged Navier-Stokes
LIC	Line Integral Convolution
w.r.t	with respect to

Contents

Contents

I Thesis in English

Part I

Thesis in English

Chapter 1

Introduction

1.1 Aerodynamic Drag

One of the main areas of focus of aerodynamic studies on cars is and always has been the accurate prediction and, on second notice, the minimization of the aerodynamic drag. Aerodynamic drag is one of the main forces applied to a body moving within a fluid. As the body advances through the fluid, it is subject to a pressure distribution applied normal to its surface, along with shear stresses applied tangentially to it, fig. 1.1. These are the two main sources responsible for the aerodynamic forces acting on the body, regardless of the complexity of its shape. Integration of the pressure and shear stress distributions over the complete body surface yields the resulting aerodynamic force $\overrightarrow{R}$ and moment $\overrightarrow{M}$, fig. 1.2.

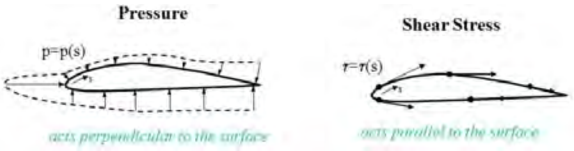

Figure 1.1: *Pressure and stress distribution applied on a body immersed in a fluid. [22]*

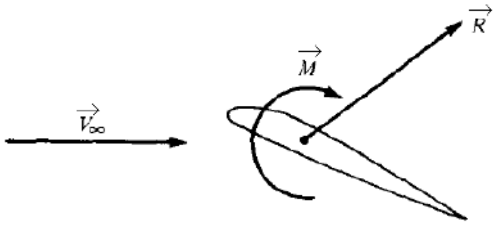

Figure 1.2: *Resulting Aerodynamic Force and Moment acting on the body. [3]*

The resulting force $\overrightarrow{R}$ and moment $\overrightarrow{M}$ can be split into three components each, according to the chosen coordinate system. Taking into account the free stream velocity vector $\overrightarrow{V_\infty}$, in a 2D problem two main forces, lift and drag are defined. Lift is the force acting perpendicular to $\overrightarrow{V_\infty}$ and drag is the force acting parallel to it. 1.3

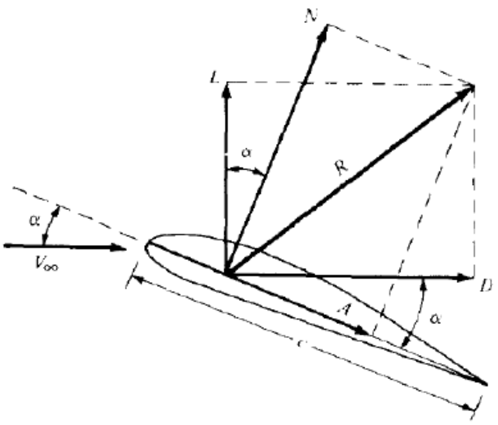

Figure 1.3: *Components of the aerodynamic force acting on the body. $\overrightarrow{L}$ is the lift i.e. the component of $\overrightarrow{R}$ perpendicular to $\overrightarrow{V_\infty}$ and $\overrightarrow{D}$ the drag force i.e. the component of $\overrightarrow{R}$ parallel to $\overrightarrow{V_\infty}$,[3].*

According to the former definition, aerodynamic drag is one of the forces a car must overcome in order to move forward. In other words, the higher the value of the drag force acting on the vehicle, the more power and energy the latter requires in order to move forward. It is therefore profound why the main target of aerodynamic studies on vehicles is the minimization of the drag force acting on it or, equivalently, its drag coefficient, C_D. When it comes to vehicle aerodynamics, the drag coefficient is one of the most important quantities used to define the aerodynamic quality of the vehicle. Let ρ_∞, be the freestream air density and S a reference area, in this case the frontal surface of the vehicle. The (freestream) dynamic pressure is then equal to $q_\infty = \frac{1}{2}\rho_\infty V_\infty^2$. The drag coefficient is defined as the magnitude of the drag force divided by the product of the freestream dynamic pressure and the reference area (eq. 7.2), which in this case is the frontal area of the car projected on the YZ plane. Thus,

$$C_D = \frac{D}{q_\infty S} \tag{1.1}$$

is a normalized value of the drag force, usually varying from 0.2 to 0.4 for passenger vehicles.

Normalized coefficients can be defined for all forces and moments acting on an arbitrary body, the most commonly used of which are the following:

- Lift coefficient $C_L = \frac{L}{q_\infty S}$
- Normal force coefficient $C_N = \frac{N}{q_\infty S}$
- Moment coefficient $C_M = \frac{M}{q_\infty S l}$, whereby l is a reference length

In fact, the last decades, with the introduction of electric vehicles with a limited power supply and the establishment of stricter waste gas emission regulations for passenger cars, there has been a remarkable effort in order to minimize the drag coefficient of vehicles. One can easily grasp the effort put into the reduction of the drag force, if we consider the quadratic relation of speed and drag, as shown in equation 7.2 [27].

1.2 CFD Techniques for Industrial Applications

Computational Fluid Dynamics (CFD)-based aerodynamic analysis is quickly gaining ground and is becoming a common way of conducting studies and optimization procedures in the industry. The radical increase in computational power together with the high availability and decreasing cost of CPUs today has led the majority of large industrial research and development units to adopt CFD and implement it routinely. What is more, the computational algorithms are continuously being improved, offering limitless potential to meet the need and requirements of the varying applications in the different fields of the industry. A key advantage is their competence to achieve an accurate prediction of the flow with a relatively low computational cost. The ability to decompose large scale problems in terms of memory and computational power into smaller, and to parallelize the solution process or even to employ the use of Graphics Processing Units (GPUs), drastically decreases the required time for the necessary procedures.

In order to perform an optimization process using CFD, certain prerequisites are necessary. The generation of a CFD mesh is an important aspect and plays a major role in the accuracy and the performance of the solution algorithms. A low quality mesh can significantly hinder the process and vice versa. The partial differential equations (PDEs) that model the physical problem are then discretized and numerically solved on this mesh. Solution of these equations yields the corresponding flow fields, which are used for the calculation of the target (or objective) function. This target function quantifies the criterion according to which the optimization is performed, for instance the drag force applied on a vehicle or the pressure losses of an engine's intake duct which needs to be minimized. For the optimization process carried out in this diploma thesis, a gradient–based optimization will be used. This method requires the computation of the derivatives of the objective function w.r.t the design variables. This computation can –depending on the problem– become extremely costly, to a point that the procedure might not be able to run on the existing computational platform. For example, this is the case when the number of design variables increases significantly, as in most industrial applications. To overcome this, the adjoint method [13], [15], [14] enables the aforementioned computation with a minimal cost, which does not scale with the number of design variables. As it will in detail be described and exhibited in the following chapters, the advantages of this method deem it suitable for a wide range of optimization problems. Regarding the continuous adjoint method [16], [19], [4], the mathematical formulation and software programming used in this thesis has been performed by the PCOpt/NTUA, in the OpenFOAM® environment.

This diploma thesis focuses on the application of the continuous adjoint method for the shape optimization of a passenger car. The term aerodynamic shape optimization implies the modification of the outer surface of the car in order to minimize its drag coefficient (and in fact, finally, the drag force applied to it, since the reference area of the car remains practically constant throughout the optimization). In order to do this, a flow analysis is initially performed, using three turbulence models. Subsequently, the solution of the adjoint problem will enable the computation of the required sensitivity derivatives based on which the sensitivity maps will be drawn. These are, in turn, used for the optimization of the car shape.

Chapter 2

The CFD Analysis and Optimization Process

The main features of the process followed to compute the drag coefficient, solve the adjoint problem and obtain the sensitivity map and, finally, perform the morphing and optimization are presented in this chapter.

2.1 The Primal Problem

2.1.1 Flow equations and discretization

The primal or state problem involves the solution of the governing equations of the flow around the car written along the three Cartesian coordinates to numerically compute the corresponding flow fields, i.e. the three components of the velocity, the pressure and the turbulent viscosity. In this case the state equations are the Reynolds–Averaged Navier–Stokes (RANS) equations for incompressible, steady flows coupled with the turbulence model equations which vary depending on the selected turbulence model. In this study, three different turbulence models were used for the closure of the mean-flow equations. The simulation was performed using second–order discretization schemes in order to predict the drag coefficient with acceptable accuracy. Given the fact that the ultimate target of this study is the aerodynamic shape optimization of the vehicle, i.e. the minimization of its drag coefficient, the accuracy and stability of the primal evaluation need to be adequate and capable to predict the drag coefficient within a few Cd counts [1]. Although a transient analysis would confidently result in a solution of higher accuracy, the

---

[1] One C_D count is equal to 0.001

computational burden is significantly increased and, therefore, steady-state analyses are exclusively performed.

2.1.2 Turbulence Modeling

The flow around a car is highly turbulent and is, therefore, governed by random, unsteady fluctuations of the pressure and velocity in a very small time scale. In order to take into account all these fluctuations, an unbearably small cell size is necessary, as well an infinitesimally small discretization of the time domain. Such a computation is practically unfeasible with the computational resources available in the industry today and a steady–state computation was carried out instead, whereby the unsteady term in the Navier–Stokes equations is omitted. In order to properly take the random fluctuations of the flow into account, starting from the instantaneous Navier–Stokes flow equations a decomposition in a mean and a fluctuating part is performed. Time -or Reynolds- averaging the emerging equations gives rise to the RANS equations 7.3, 7.4.

The system of the RANS equations for an incompressible fluid flow are shown below, where repeated indices denote summation, according to the Einstein's convention.

Conservation of Mass

$$R^p = -\frac{\partial v_j}{\partial x_j} = 0 \tag{2.1}$$

Conservation of Momentum

$$R_i^v = v_j \frac{\partial v_i}{\partial x_j} - \frac{\partial}{\partial x_j}\left[\left(\nu + \nu_t\right)\left(\frac{\partial v_i}{\partial x_j} + \frac{\partial v_j}{\partial x_i}\right)\right] + \frac{\partial p}{\partial x_i} = 0 \qquad i = 1, 2, 3 \tag{2.2}$$

In equations 7.3 and 7.4, v_i are the components of the velocity in the three cartesian coordinates and p the static pressure divided by the constant density of the fluid. A new term is introduced in these equations, the Reynolds non-linear stress term which according to the Boussinesq hypothesis [13] is equal to

$$\tau'_{ij} = -\rho\overline{v'_i v'_j} = \rho\nu_t(\frac{\partial v_i}{\partial x_j} + \frac{\partial v_j}{\partial x_i}) - \frac{2}{3}k\delta_{ij} \tag{2.3}$$

whereby

$$k = \frac{1}{2}\overline{v_i' v_i'} \tag{2.4}$$

The Reynolds stress term essentially describes the turbulent vertical advection of streamwise turbulent momentum or, in simple terms, the vertical flux of streamwise momentum and plays a similar role to the viscous stresses, hence its name. ν_t is the kinematic turbulent viscosity or kinematic eddy viscosity and has the same units as the kinematic viscosity of the fluid, m^2/s. The introduction of this new variable into the averaged Navier-Stokes equations yields a new complication for the solution of the problem, since the necessity of more equations to close the system arises. This issue, also referred to as the 'closure problem', is overcome by the introduction of the so-called 'turbulence models', which attempt to model the turbulence using different approximations, constants and variables. These are directly linked to the turbulent properties of the flow and are the result of extensive experimental data and analysis of the past decades. Finally, a new set of equations that describe the turbulent behavior of the flow are introduced.

This results in a significant decrease in the computational time. Particularly, in areas of high adverse pressure gradients where turbulent structures of very small and large scales govern the flow, the ability of the different models to predict the pressure and velocity fields accurately is challenged. As mentioned above, three different turbulence models are used in the analysis performed within this diploma thesis, the $k-\epsilon$ [10], [11], the $k-\omega$ SST [6], [7], [8] and the Spalart-Allmaras [5]. Their PDEs and main features will be discussed below, [9].

The k-ϵ Turbulence Model

The k-ϵ [10], [11] is one of the most commonly used turbulence models, in a wide range of applications today. This is mainly due to its relative simple implementation, generally stable convergence and, on average, reasonable flow predictions in many different flow conditions. It is a two-equation turbulence model, meaning that it introduces two new transport PDEs in order to model turbulence via two quantities, the turbulent kinetic energy k and the turbulent energy dissipation rate ϵ. In the standard High–Re k-ϵ formulation for incompressible fluid, the equations are written as follows [26]

$$\frac{\partial(kv_j)}{\partial x_j} = \frac{\partial}{\partial x_j}[\frac{\nu_t}{\sigma_k}\frac{\partial k}{\partial x_j}] + 2\nu_t E_{ij}E_{ij} - \varepsilon \tag{2.5}$$

$$\frac{\partial(\epsilon v_j)}{\partial x_j} = \frac{\partial}{\partial x_j}[\frac{\nu_t}{\sigma_\varepsilon}\frac{\partial\varepsilon}{\partial x_j}] + C_{1\varepsilon}2\frac{\varepsilon}{k}\nu_t E_{i\mathrm{j}}E_{i\mathrm{j}} - C_{2\varepsilon}\frac{\varepsilon^2}{k} \tag{2.6}$$

whereby $C_\mu = 0.09, C_{1\varepsilon} = 1.44, C_{2\varepsilon} = 1.92, \sigma_k = 1.0, \sigma_\varepsilon = 1.3$ are specific constants of this turbulence model and $E_{i\mathrm{j}}$ are the components of the rate of deformation tensor. Finally, ν_t is computed via the following equation $\nu_t = C_\mu \frac{k^2}{\varepsilon}$.

Wall Treatment

Since the average distance of the first cell center from the wall boundaries is higher than that required for a boundary layer resolution, wall functions are used to model and approximate the value of the turbulent variables at this area [6]. With the use of wall functions, the grid point adjacent to the wall can be placed well away from the wall ($y^+ = 40 - 100$) and the shear stress at the wall τ_w can be inferred from the velocity at that point. y^+ is the non-dimensional distance and is defined as $y^+ = \frac{v_\tau y}{\nu}$ where $v_\tau = \sqrt{\tau_w}$ is the friction velocity and y the distance of the cell center from the wall. Another variable used for the formulation of the wall treatment is the non-dimensional velocity $v^+ = \frac{v}{v_\tau}$. The computation of the velocity profile of the flow varies depending on the area of the boundary layer in which it is performed. The velocity profile in the characteristic areas of the boundary layer can be seen in figure 2.1.

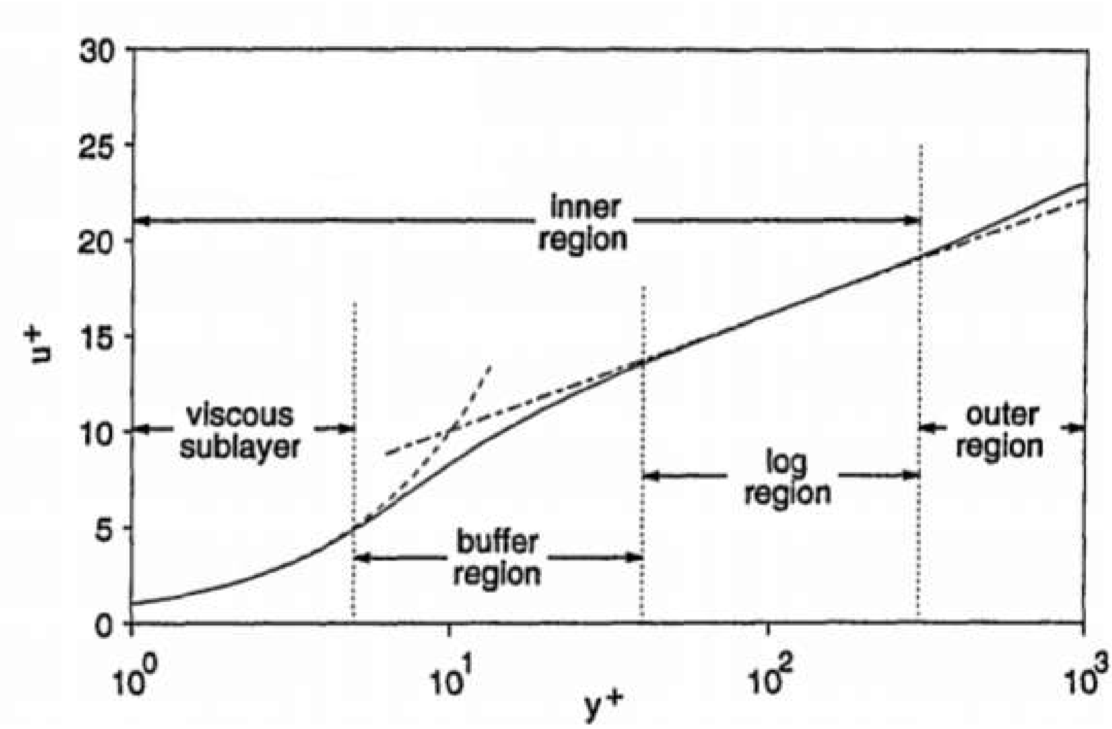

Figure 2.1: *Velocity profile in the characteristic regions of a turbulent boundary layer, [6].*

In the viscous sublayer we have that

$$v^+ = y^+ => \frac{u}{v_\tau} = \frac{v_\tau y}{\nu} \tag{2.7}$$

whereas in the logarithmic region, the following equation holds

$$v^+ = \frac{1}{\kappa} ln(y^+) + C => \frac{v}{v_\tau} = \frac{1}{\kappa} ln(\frac{v_\tau y}{\nu}) + C \tag{2.8}$$

where $C = 5$.

If we neglect the buffer zone [1], exactly at the intersection of the two previously mentioned regions, both equations 2.7 and 2.8 hold. We therefore get that at that point

$$y_c^+ = \frac{1}{\kappa} ln(y_c^+) + C \tag{2.9}$$

Equation 2.9 can be solved using the Newton-Raphson method and the value of y_c^+ can be extracted. Following this, we have to identify the region in which the point where the computation is performed resides. To do this, an initial assumption that it lies in the viscous sublayer is made. Using the velocity field computed at the previous iteration, from equation 2.7 we obtain the value of v_τ and we can then compute the value of y^+. If the computed y^+ is smaller than y_c^+ then our initial assumption is was correct. Otherwise, the point lies in the logarithmic region and equation 2.8 should be used to obtain the value of v_τ.

Following this, if the point adjacent to the wall lies within the logarithmic region (which should be the case when using a High-Reynolds turbulence model) where the production and dissipation of the turbulent kinetic energy are approximately equal [6], the turbulence model-specific variables can be computed using the following equations

$$k = \frac{v_\tau^2}{\sqrt{C_\mu}} \tag{2.10}$$

and

$$\epsilon = \frac{v_\tau^3}{\kappa y} \tag{2.11}$$

where κ is the von-Karman constant and is equal to 0.41.

These equations are derived by taking into account the fact that in the logarithmic region, the shear stress at the wall is equal to

$$\tau_w = (\nu + \nu_t)|\frac{\partial v_i}{\partial x_j} n_j| \tag{2.12}$$

Wall Treatment in OpenFOAM®

In the OpenFOAM® environment, wall functions for k and ϵ are applied using the same equations, but with a manipulation that results in a slightly different formulation [7], [8]. This is presented in short in what follows. It should be noted here, that there is a major difference between the computation performed in OpenFOAM® and the formulation described previously in section "Wall Treatment" of 2.1.2 for the computation of ν_t. OpenFOAM® utilizes Finite Differences (FD) to compute the gradient of the velocity at the wall which is used to compute the friction velocity v_τ, i.e. $[\frac{\partial v_i}{\partial x_j}]^f n_j = [\frac{\partial v_i}{\partial n}]^f = \frac{v_i^f - v_i^c}{y}$ whereby $\vec{n}$ is the normal to the wall vector with a direction from the fluid to the wall. v_i^c is the velocity at the center of the cell adjacent to the wall (which is considered to be parallel to the wall) and v_i^f the parallel to the wall velocity at the cell's face (thus v^f is equal to zero). This method can give erroneous results for the computed derivative when performed on a High-Re mesh as in this diploma thesis. Equation $\tau_w = v_\tau^2 = (\nu + \nu_t)|\frac{\partial v_i}{\partial n}|$ is therefore used to ensure that the value obtained for ν_t is such that the prediction of the wall stress is correct.

Initially, a zero Neumann boundary condition is imposed to the turbulent kinetic energy k. For the turbulent energy dissipation ϵ, a weighting factor W is initially computed, which depends on the number of the faces of the cell under consideration to which the boundary condition will be applied. Then, the value at the center of each cell which is adjacent to the wall is set equal to:

$$\epsilon = \frac{1}{W}\sum_{f=i}^{w}(\frac{C_\mu^{3/4}k^{3/2}}{\kappa y_i}) \tag{2.13}$$

where k is the value of the turbulent kinetic energy at the same cell center.

The value of y^+ depends on the turbulent kinetic energy and is computed from

$$y^+ = C_\mu^{0.25} y\sqrt{\frac{k}{\nu}} \tag{2.14}$$

Finally, ν_t is computed depending on the cell's distance from the wall. The value of y_c^+ is first computed from equation 2.9 If the adjacent to the wall cells' center resides in the viscous sublayer i.e. if $y_c^+ > y^+$, then ν_t is set to zero. Otherwise, the following equation is used

$$\nu_t = \nu(\frac{\kappa y^+}{ln(Ey^+)} - 1) \tag{2.15}$$

where E=9.8.

Equation 2.15 is used to compute an artificial value for ν_t, which, when multiplied with the gradient of the velocity at the wall computed with FD (equation 2.12) will yield the correct value for the shear stress at the wall.

The $k-\omega$ SST Turbulence Model

The $k-\omega$ SST turbulence model [6], [7], [8] is also a two equation model which uses two variables to model the effect of turbulence on the mean flow. These are the turbulent kinetic energy k, which is also used in the $k-\epsilon$ model, and the specific dissipation rate ω. As far as the specific dissipation rate is concerned, it describes the rate at which turbulence kinetic energy is converted into thermal internal energy per unit volume and time. The Shear Stress Transport - (SST) formulation is a variant of the original Wilcox $k-\omega$ turbulence model whereby a switch from $k-\omega$ to $k-\epsilon$ is performed when solving for the free-stream flow, avoiding issues regarding the sensitivity of the standard k-ω model to the freestream value of ω and the often false prediction of separation in severe adverse pressure gradient flows. Moreover, the limiting factor of the Shear Stress formulation helps to avoid a build-up of excessive turbulent kinetic energy near stagnation points and other regions with large normal stress.

The variables k and ω are computed via the two following PDEs

$$\frac{\partial(kv_j)}{\partial x_j} = P_k - \beta^* k\omega + \frac{\partial}{\partial x_j}[(\nu + \sigma_k \nu_t)\frac{\partial k}{\partial x_j}] \tag{2.16}$$

$$\frac{\partial(\omega v_j)}{\partial x_j} = \alpha S^2 - \beta\omega^2 + \frac{\partial}{\partial x_j}[(\nu + \sigma_\omega \nu_t)\frac{\partial \omega}{\partial x_j}] + 2(1 - F_1)\sigma_{\omega 2}\frac{1}{\omega}\frac{\partial k}{\partial x_i}\frac{\partial \omega}{\partial x_i} \tag{2.17}$$

and, upon computation of these, ν_t can be computed as follows

$$\nu_t = \frac{\alpha_1 k}{max(\alpha_1 \omega, SF_2)} \tag{2.18}$$

whereby

$$\begin{gathered} F_2 = \tanh((max(\frac{2\sqrt{k}}{\beta^*\omega y},\frac{500\nu}{y^2\omega}))^2), P_k = min(\tau_{ij}\frac{\partial u_i}{\partial x_j},10\beta^* k\omega), \\ F_1 = \tanh((min(max(\frac{\sqrt{k}}{\beta^*\omega y},\frac{500\nu}{y^2\omega}),\frac{4\sigma_{\omega 2}k}{CD_{k\omega}y^2}))^4), CD_{k\omega} = max(2\rho\sigma_{\omega 2}\frac{1}{\omega}\frac{\partial k}{\partial x_i}\frac{\partial \omega}{x_i}, 10^{-10}), \\ \phi = \phi_1 F_1 + \phi_2(1 - F_1), \beta^* = \frac{9}{100} \end{gathered} \tag{2.19}$$

with $\alpha, \beta, \sigma_k, \sigma_\omega$ depending on whether the k-ϵ or k-ω formulation is used at the point of the domain that the computation takes place.

Again, wall functions are used to approximate the values of k and ω at the cell adjacent to the wall [7], [8]. A zero Neumann boundary condition is imposed on the turbulent kinetic energy as in the k-ϵ model. The value imposed to the turbulent specific dissipation ω differs, depending on whether the cell center resides in the viscous sublayer where $\omega = \omega_{vis} = \frac{6\nu}{\beta_1 y}$ or the logarithmic region where $\omega = \omega_{Log} = \frac{k^{0.5}}{C_\mu \kappa y}$. In the buffer zone (the area between the two) the blending function $\omega = \sqrt{\omega_{vis}^2 + \omega_{Log}^2}$ is used. In the above equation, $\beta_1 = 0.075$.

The Spalart-Allmaras Turbulence Model

The Spalart-Allmaras [5] is a one equation mixing-length turbulence model for incompressible flows. It uses a single transport equation to model the kinematic eddy viscosity by introducing a new viscosity-like variable, known as the Spalart-Allmaras variable, or $\widetilde{\nu}$,

$$\nu_t = \widetilde{\nu} f_{v1} \tag{2.20}$$

where

$$f_{v1} = \frac{X^3}{X^3 + C_{v1}^3}, \qquad X = \frac{\widetilde{\nu}}{\nu} \tag{2.21}$$

It is very popular among CFD applications of external aerodynamics, due to its ability to accurately predict the flow developement is areas of high adverse pressure gradients, which often occur in external aerodynamics applications. It is shown to give good quality results for attached flows, or flows with mid-high separation and recirculation. In order to obtain the Spalart-Allmaras variable $\widetilde{\nu}$ a single PDE is iteratively solved, which is the following

$$\frac{\partial(\tilde{\nu} v_j)}{\partial x_j} = C_{b1}(1 - f_{t2})\tilde{S}\tilde{\nu} - [C_{w1} f_w - \frac{C_{b1}}{\kappa^2} f_{t2}](\frac{\tilde{\nu}}{d})^2 + \frac{1}{\sigma}[\frac{\partial}{\partial x_j}((\nu + \tilde{\nu})\frac{\partial \tilde{\nu}}{\partial x_j}) + C_{b2}\frac{\partial \tilde{\nu}}{\partial x_i}\frac{\partial \tilde{\nu}}{\partial x_i}] \tag{2.22}$$

Quantities $\sigma = 2/3, C_{b1} = 0.1355, C_{b2} = 0.622, \kappa = 0.41, C_{w1} = 3.239, C_{v1} = 7.1$ are turbulence model constants, d is the distance of the field point to the nearest wall, while $\tilde{S}, ft2, f_w$ are computed with the following equations

$$\begin{aligned} \tilde{S} &= \Omega + \frac{\tilde{\nu}}{\kappa^2 d^2} f_{v2}, \qquad \Omega = \sqrt{2 W_{ij} W_{ij}}, \\ W_{ij} &= \frac{1}{2}(\frac{\partial v_i}{\partial x_j} - \frac{\partial v_j}{\partial x_i}) \end{aligned} \tag{2.23}$$

Also,

$$
\begin{aligned}
f_{v2} &= 1 - \frac{X}{1 + X f_{v1}}, & f_w &= g[\frac{1 + c_{w3}^6}{g^6 + c_{w3}^6}]^{1/6}, \\
g &= r + c_{w2}(r^6 - 6), & r &= \min[\frac{\tilde{\nu}}{\tilde{S}\kappa^2 d^2}, 10], \\
f_{t2} &= c_{t3} e^{-c_{t4} X^2}
\end{aligned}
\tag{2.24}
$$

In the Spalart-Allmaras model, wall functions are also used to approximate the value of ν_t at the cell closest to the wall. The formulation for the computation of y^+ follows Spaldings Law [14], which models the inner sublayer and the logarithmic region of the boundary layer with one equation

$$
y^+ = u^+ + \frac{1}{E}[e^{\kappa u^+} - 1 - \kappa u^+ - \frac{1}{2}(\kappa u^+)^2 - \frac{1}{6}(\kappa u^+)^3]
\tag{2.25}
$$

ν_t is computed according to $\nu_t = \frac{u_\tau^2}{\frac{\partial U}{\partial n}} - \nu$, where the previously computed y^+ value is taken into account in the computation of u_τ.

2.1.3 Boundary Conditions

In order to iteratively solve the flow and adjoint equations, boundary conditions need to be imposed along all the boundaries of the domain for each variable of the problem. The boundaries include the inlet, the outlet, the two sides and the top of the simulated domain, the road, and, finally the car surface including the wheels, which due to their different motion will be treated separately from the rest of the vehicle. The proper specification of boundary conditions is a necessity to guarantee the wellposedness of the problem, as well as accordance with the physics that govern the flow in reality.

The variables for the primal problem are the static pressure and velocity as well as the selected turbulence variables depending on the turbulence model. As far as the turbulence models are concerned, in OpenFOAM® [7], [8], wall functions for the k, ϵ, ω and ν_t can be used to compute the near–wall values of the turbulent variables in case the distance of the first cell center from the wall dictates so, as previously described.

For the rest, the following boundary conditions are used.

- **Inlet**

  At the inlet of the computational domain, a Dirichlet boundary condition is imposed on the freestream velocity and a zero Neumann boundary condition on the static pressure. The Spalart-Allmaras variable $\tilde{\nu}$ is defined using a Dirichlet boundary condition depending on the value of the kinematic viscosity ν of the fluid. The variables k, ω and ϵ are approximated depending on the turbulence intensity I and the freestream velocity magnitude U at the inlet. So, for k we have

$$k = \frac{3}{2}(UI)^2 \tag{2.26}$$

and ϵ and ω are approximated depending on the user-defined eddy viscosity ratio $\frac{\nu}{\nu_t}$ [25] as follows

$$\epsilon = C_\mu \frac{k^2}{\nu}(\frac{\nu_t}{\nu})^{-1} \qquad\qquad \omega = \frac{k}{\nu}(\frac{\nu_t}{\nu})^{-1} \tag{2.27}$$

- **Outlet**

  Zero Neumann and zero Dirichlet boundary condition are imposed on the velocity and pressure fields, respectively, at the outlet of the domain. Zero Neumann boundary conditions imposed on all turbulent variables k, ϵ, ω and $\tilde{\nu}$.

- **Wall Boundaries**

  A no-slip condition is imposed on the velocity field at all the solid boundaries of the vehicle with the exception of the wheels, for which in case ground simulation is performed, a constant angular velocity is applied to the outer area of the wheels that ensured no-slip condition at meeting point of the wheel and the moving ground. Dirichlet boundary condition to the ground and zero Neumann boundary condition is imposed on the static pressure field. Wall functions are used for the turbulence variables at the wall.

- **Top and Sides of the Domain**

  The slip boundary condition is used for the velocity at the surrounding surfaces of the domain (the normal to the surface component is zero -zero Dirichlet condition-, whereas the parallel components are non-zero (i.e. zero Neumann condition)] [16] [15]. It, firstly, implies that no flow flux is able to pass through the wall and that there is zero wall shear stress applied from the wall surface to the fluid. This boundary condition is also used to model the symmetry of the domain when the simulations using the half car model were performed.

2.2 The Adjoint Problem

As previously stated, the main target of this diploma thesis is the minimization of the drag coefficient of the vehicle by modifying its shape. The required tools to perform this task are a CFD simulation software able to compute the velocity and pressure fields around the vehicle as well as the required objective function (evaluation tool), a space parameterization and shape morphing tool in order to optimize the geometry without remeshing (the former in order to parameterize the surface and volume mesh so that its points can be moved as required and the latter in order to move the mesh points) and, finally, a software capable of computing the gradient of the target function w.r.t. the design variables, according to which the shape change will be performed. One of the major issues when dealing with gradient–based shape optimization problems in industrial applications is the computational time required to compute the gradient. Accurate prediction of the gradient in a timely fashion is key to gradient-based optimization. The large number of design variables involved in the majority of such problems, in combination with the huge meshes that usually come, hand in hand with, real industrial applications render the use of gradient computation methods such as the Finite Differences or the Direct Differentiation [9] practically unfeasible. This applies to any gradient computation method whose required simulation time scales with the number of design variables. Among the possible ways to compute the derivative of the target function w.r.t. the design variables in shape optimization problems, the adjoint method [13], [15], [14], [16] has proven to be the optimal solution. It enables the computation of the sensitivity derivatives at a cost that is not dependent on the number of design variables, but is practically equal to one Equivalent Flow Solution (EFS). Note that a single EFS is representing the time required to achieve convergence of the corresponding primal problem.

2.2.1 Objective Function

The main concept of the adjoint problem is the following. The objective function is defined by the engineer. It represents the physical quantity that is the aim of the optimization problem. In our case, this is the drag force applied on the vehicle by pressure and viscous stresses exerted upon it by the surrounding fluid. The drag force in incompressible flow is the following:

$$F = \int_{S_W} [(p\delta_i^j - \tau_{ij})r_j]n_i dS \tag{2.28}$$

where n_i is the surface normal vector, r_j the direction vector of the force and δ_i^j the Kronecker symbol.

After the objective function has clearly been defined, as a next step it is augmented by the volume integrals of the flow equations multiplied by the newly introduced adjoint fields. These are the adjoint velocity u, pressure q and adjoint turbulence variables Ψ_k, $k = 1, M$, whereby M is the number of PDEs solved by the turbulence model. The flow (or state) equations are in this case the continuity and momentum conservation equations, which are -together with their boundary conditions- satisfied in each and every (internal or boundary) point of the computational domain adding, therefore, no contribution to the original objective function. The augmented objective function can be written as follows:

$$F_{aug} = F + \int_{\Omega} u_i R_i^v d\Omega + \int_{\Omega} q R^p d\Omega + \sum_{k=1}^{M} \int_{\Omega} \Psi_k R^k d\Omega \tag{2.29}$$

where Ω is the computational domain. The adjoint formulation that takes into account the contribution of the turbulence model has already been developed and implemented by the PCOpt/NTUA. This includes the continuous adjoint equations for the Spalart-Allmaras, the $k - \epsilon$, the $k - \omega$ and the $k - \omega$ SST turbulence models [12], [14], [16], [17], [18].

The resulting augmented objective function is, in turn, differentiated. This will give the total (or material) derivative of the augmented objective function w.r.t. the flow variables and the geometry variation i.e. how much is the influence on the objective function from a) change of the car shape on the vehicles boundary surface b) change in the flow fields which is, in turn, caused by this geometry variation

Differentiation of the objective function can be done in various ways one of which will be presented here. All of them yield the same Field Adjoint Equations and Adjoint Boundary Conditions but a different formulation of the sensitivity derivatives [12], [13], [15]. In the following development, in order to keep the mathematics as simple as possible, the adjoint method is presented by skipping the turbulence model PDEs.

Applying the delta operator on the augmented objective function we get:

$$\frac{\delta F_{aug}}{\delta b_n} = \frac{\delta F}{\delta b_n} + \frac{\delta}{\delta b_n} \int_{\Omega} u_i R_i^v d\Omega + \frac{\delta}{\delta b_n} \int_{\Omega} q R^p d\Omega \tag{2.30}$$

Then, the Leibniz theorem which is used for the differentiation of the volume integrals with variable boundaries, is applied

$$\frac{\delta F_{aug}}{\delta b_n} = \frac{\delta F}{\delta b_n} + \int_{\Omega} u_i \frac{\partial R_i^v}{\partial b_n} d\Omega + \int_{\Omega} q \frac{\partial R^p}{\partial b_n} d\Omega + \int_{S} (u_i R_i^v + q R^p) \frac{\delta x_k}{\delta b_n} n_k dS \tag{2.31}$$

where S is the boundary of the computational domain, $S = S_I \cup S_O \cup S_W \cup S_{W_P}$. The boundaries S_I, S_O, S_W and S_{W_P} refer to the inlet, outlet, fixed and parameterized boundaries of the domain, respectively. However, only the parameterized boundaries may change ($\frac{\delta x_k}{\delta b_n} n_k$ corresponds to the deformation velocity of the surface in the normal direction) so we have

$$\frac{\delta F_{aug}}{\delta b_n} = \frac{\delta F}{\delta b_n} + \int_{\Omega} u_i \frac{\partial R_i^v}{\partial b_n} d\Omega + \int_{\Omega} q \frac{\partial R^p}{\partial b_n} d\Omega + \int_{S_{W_P}} (u_i R_i^v + q R^p) \frac{\delta x_k}{\delta b_n} n_k dS \tag{2.32}$$

Since the state equations together with their boundary conditions are satisfied at each and every point of the computational domain, $F = F_{aug}$ and, consequently, $\frac{\delta F}{\delta b_n} = \frac{\delta F_{aug}}{\delta b_n}$.

The total differentiation of the objective function $\frac{\delta F}{\delta b_n}$ yields a number of surface integrals.

$$F = \int_{S_W} F_S dS = \int_{S_W} F_{S,i} n_i dS = \int_{S_W} [(p\delta_i^j - \tau_{ij}) r_j] n_i dS \tag{2.33}$$

By applying the total derivative operator to the objective function we get

$$\begin{aligned}
\frac{\delta F}{\delta b_n} &= \frac{\delta}{\delta b_n} \int_{S_W} F_{S,i} n_i dS \\
&= \int_{S_W} \frac{\delta F_{S,i}}{\delta b_n} n_i dS + \int_{S_W} F_{S,i} \frac{\delta n_i}{\delta b_n} dS + \int_{S_W} F_{S,i} n_i \frac{\delta (dS)}{\delta b_n} \\
&= \int_{S_W} \frac{\delta [(p\delta_i^j - \tau_{ij}) r_j]}{\delta b_n} n_i dS + \int_{S_W} [(p\delta_i^j - \tau_{ij}) r_j] \frac{\delta n_i}{\delta b_n} dS + \\
&+ \int_{S_W} [(p\delta_i^j - \tau_{ij}) r_j] n_i \frac{\delta (dS)}{\delta b_n}
\end{aligned} \tag{2.34}$$

and, if we take into account that [12],

$$\frac{\delta \Phi}{\delta b_n} = \frac{\partial \Phi}{\partial b_n} + \frac{\partial \Phi}{\partial x_k} \frac{\delta x_k}{\delta b_n} \tag{2.35}$$

we get

$$\begin{aligned}\frac{\delta F}{\delta b_n} =& \int_{S_W} \frac{\partial[(p\delta_i^j - \tau_{ij})r_j]}{\partial b_n} n_i dS + \int_{S_W} \frac{\partial[(p\delta_i^j - \tau_{ij})r_j]}{\partial x_k} \frac{\delta x_k}{\delta b_n} n_i dS + \int_{S_W} [(p\delta_i^j - \tau_{ij})r_j] \frac{\delta n_i}{\delta b_n} dS \ + \\ & + \int_{S_W} [(p\delta_i^j - \tau_{ij})r_j] n_i \frac{\delta(dS)}{\delta b_n} \\ =& \int_{S_W} \frac{\partial[(p\delta_i^j - \tau_{ij})r_j]}{\partial v_k} \frac{\partial v_k}{\partial b_n} n_i dS + \int_{S_W} \frac{\partial[(p\delta_i^j - \tau_{ij})r_j]}{\partial p} \frac{\partial p}{\partial b_n} n_i dS + \int_{S_W} \frac{\partial[(p\delta_i^j - \tau_{ij})r_j]}{\partial \tau_{kj}} \frac{\partial \tau_{kj}}{\partial b_n} n_i dS \\ & + \int_{S_W} \frac{\partial[(p\delta_i^j - \tau_{ij})r_j]}{\partial x_k} \frac{\partial x_k}{\partial b_n} n_i dS + \int_{S_W} [(p\delta_i^j - \tau_{ij})r_j] \frac{\delta n_i}{\delta b_n} dS + \int_{S_W} [(p\delta_i^j - \tau_{ij})r_j] n_i \frac{\delta(dS)}{\delta b_n}\end{aligned} \tag{2.36}$$

The final expression of the material derivative of the augmented objective function w.r.t. the design variables is formulated as follows

$$\begin{aligned}\frac{\delta F_{aug}}{\delta b_n} =& \int_{S_W} (u_i v_j n_j + \tau_{a,ij} n_j - q n_i + \frac{\partial[(p\delta_k^j - \tau_{kj})r_j]}{\partial v_i} n_k) \frac{\partial v_i}{\partial b_n} dS + \int_{S_W} (u_j n_j + \frac{\partial[(p\delta_i^j - \tau_{ij})r_j]}{\partial p} n_i) \frac{\partial p}{\partial b_n} dS + \\ & + \int_{S_W} (-u_i n_j + \frac{\partial[(p\delta_k^j - \tau_{kj})r_j]}{\partial \tau_{ij}} n_k) \frac{\partial \tau_{ij}}{\partial b_n} dS + \\ & + \int_{S_{W_p}} n_i \frac{\partial[(p\delta_i^j - \tau_{ij})r_j]}{\partial x_k} \frac{\delta x_k}{\delta b_n} dS + \int_{S_{W_p}} [(p\delta_i^j - \tau_{ij})r_j] \frac{\delta n_i}{\delta b_n} dS + \\ & + \int_{S_{W_p}} [(p\delta_i^j - \tau_{ij})r_j] n_i \frac{\delta(dS)}{\delta b_n} + \int_{S_{W_p}} (u_i R_i^v + q R^p) \frac{\delta x_k}{\delta b_n} n_k dS + \\ & + \int_\Omega \left\{ u_j \frac{\partial v_j}{\partial x_i} - \frac{\partial(v_j u_i)}{\partial x_j} - \frac{\partial}{\partial x_j} \left[(\nu + \nu_t) \left(\frac{\partial u_i}{\partial x_j} + \frac{\partial u_j}{\partial x_i} \right) \right] + \frac{\partial q}{\partial x_i} \right\} \frac{\partial v_i}{\partial b_n} d\Omega + \\ & + \int_\Omega (-\frac{\partial u_j}{\partial x_j}) \frac{\partial p}{\partial b_n} d\Omega\end{aligned} \tag{2.37}$$

Considering the partial derivatives of the objective function w.r.t. the flow variables and the stress tensor

$$
\begin{aligned}
&\frac{\partial F_{S,i}}{\partial v_k}n_i = \frac{\partial[(p\delta_i^j - \tau_{ij})r_j]}{\partial v_k}n_i = 0\\
&\frac{\partial F_{S,i}}{\partial p}n_i = \frac{\partial[(p\delta_i^j - \tau_{ij})r_j]}{\partial p}n_i = \delta_i^j r_j n_i = r_j n_j\\
&\frac{\partial F_{S,k}}{\partial \tau_{ij}}n_k = \frac{\partial[(p\delta_k^j - \tau_{kj})r_j]}{\partial \tau_{ij}}n_k = -\delta_i^k r_j n_k\\
&\frac{\partial F_{S,i}}{\partial x_k}n_i = \frac{\partial p}{\partial x_k}r_i n_i - \frac{\partial \tau_{ij}}{\partial x_k}r_j n_i = \frac{\partial p}{\partial x_k}r_i n_j \delta_i^j - \frac{\partial \tau_{ij}}{\partial x_k}r_j n_i = \frac{\partial p}{\partial x_k}r_i n_j \delta_i^j - \frac{\partial \tau_{ij}}{\partial x_k}r_i n_j
\end{aligned}
\tag{2.38}
$$

the final expression of the total derivative of the augmented objective function is derived

$$
\begin{aligned}
\frac{\delta F_{aug}}{\delta b_n} = &\int_{S_W}(u_i v_j n_j + \tau_{a,ij} n_j - q n_i)\frac{\partial v_i}{\partial b_n}dS + \int_{S_W}(u_j n_j + n_j r_j)\frac{\partial p}{\partial b_n}dS +\\
&+\int_{S_W}[-(u_i n_j + r_j n_i)]\frac{\partial \tau_{ij}}{\partial b_n}dS +\\
&+\int_{S_{W_p}}[n_j r_i \frac{\delta x_k}{\delta b_n}(\frac{\partial p}{\partial x_m}\delta_i^j - \frac{\partial \tau_{ij}}{\partial x_m})]dS + \int_{S_{W_p}}[(p\delta_i^j - \tau_{ij})r_j]\frac{\delta n_i}{\delta b_n}dS +\\
&+\int_{S_{W_p}}[(p\delta_i^j - \tau_{ij})r_j]n_i \frac{\delta(dS)}{\delta b_n} + \int_{S_{W_p}}(u_i R_i^v + q R^p)\frac{\delta x_k}{\delta b_n}n_k dS +\\
&+\int_{\Omega}\left\{u_j \frac{\partial v_j}{\partial x_i} - \frac{\partial (v_j u_i)}{\partial x_j} - \frac{\partial}{\partial x_j}\left[(\nu + \nu_t)\left(\frac{\partial u_i}{\partial x_j} + \frac{\partial u_j}{\partial x_i}\right)\right] + \frac{\partial q}{\partial x_i}\right\}\frac{\partial v_i}{\partial b_n}d\Omega +\\
&+\int_{\Omega}(-\frac{\partial u_j}{\partial x_j})\frac{\partial p}{\partial b_n}d\Omega
\end{aligned}
\tag{2.39}
$$

Field Adjoint Equations

The total differentiation of F_{aug} gave rise to the partial derivatives of the primal variables w.r.t. the design variables (namely $\frac{\partial v_i}{\partial b_n}$ and $\frac{\partial p}{\partial b_n}$). These terms are of very high computational cost and shall not be computed, which motivates their elimination by setting their multipliers to zero. As a result, the Field Adjoint Equations and their boundary conditions are formulated. Their final form is as follows

$$R^q = -\frac{\partial u_j}{\partial x_j} = 0 \tag{2.40}$$

$$R_i^u = u_j \frac{\partial v_j}{\partial x_i} - \frac{\partial (v_j u_i)}{\partial x_j} - \frac{\partial}{\partial x_j}\left[(\nu + \nu_t)\left(\frac{\partial u_i}{\partial x_j} + \frac{\partial u_j}{\partial x_i}\right)\right] + \frac{\partial q}{\partial x_i} = 0 \ , \ i = 1, 2(, 3) \tag{2.41}$$

where the adjoint turbulence model PDEs are omitted, for the reason explained previously.

A few notes on these equations are useful here, in order to give a better understanding of some procedures that took up a significant amount of time during this diploma thesis. The Field Adjoint Equations (FAEs) are very similar to the primal state equations. They both include a convective, a diffusive, and a pressure gradient term. They pose, however, very crucial differences. The first one being that these equations are linear, in contrast to the Navier–Stokes equations whose velocity convection term is non-linear. What is more, the adjoint velocity is convected backwards from the outlet to the inlet of the computational space, in this case from the wake towards the vehicle and the inlet. The most decisive difference, however, is the extra term that appears in the FAEs, which is known as the Adjoint Transpose Convection or ATC. This non-conservative source term has a great influence to the stability and convergence of the adjoint equations and is, often, the term that leads this linear system of equations to divergence.

In the formulation used in this thesis, the ATC term requires a vector-tensor multiplication which results in a cross coupling of the components of the adjoint velocity. This leads to a weak coupling between the adjoint velocity components within the system of equations, which, in combination with the unstable nature of this source term can often drive the adjoint system of equations to a gradual self-induced divergence[5]. Another term which has proven to be influential to the stability of the adjoint is the convection term of the turbulence model equations of the flow problem. When discretized with 2^{nd} order schemes, this term tends to drive the turbulence variables to enter an intense oscillation whereby they may even obtain unphysical values. This may, in turn, cause some of the eigenvalues of the system's left hand side matrix to become greater that unity, driving the system to become unsteady or even to diverge. Since the flow and adjoint problem share the same eigenvalues, the eigenvalues computed at the last iteration of the iterative solution of the flow problem will be given as input to the adjoint problem. The non-linearity of the primal system is protecting it against divergence, since its matrix (and hence, its eigenvalues) is recomputed on every iteration of the primal solver loop. This however does not hold for the adjoint system of equations which is linear and its eigenvalues are therefore constant throughout the iterative solution and are computed during the last iteration of the primal solution. This means that the existence of a single eigenvalue greater than 1 on the primal system will drive the adjoint equations to divergence. Among the numerous ways to counter this issue, a common practice is to reduce the discretization order of the turbulence equations which will effectively reduce the oscillation of the turbulent variables. In order for the convergence and stability of the problem to be ensured, a few measures were employed including mainly averaging of the primal solution along with relatively low relaxation factors –to reduce the fluctuation of the primal solution–, and the use of specific limiters and schemes for the treatment of the more unstable numerical terms. Under-relaxing the equations is essentially keeping part of the solution of the previous iteration and part of the one currently solved. This is used to control the stability and convergence rate of the iterative process. The under-relaxation factor generally increases the stability of the system and reduces its fluctuation, as it can be seen below, figure 2.2

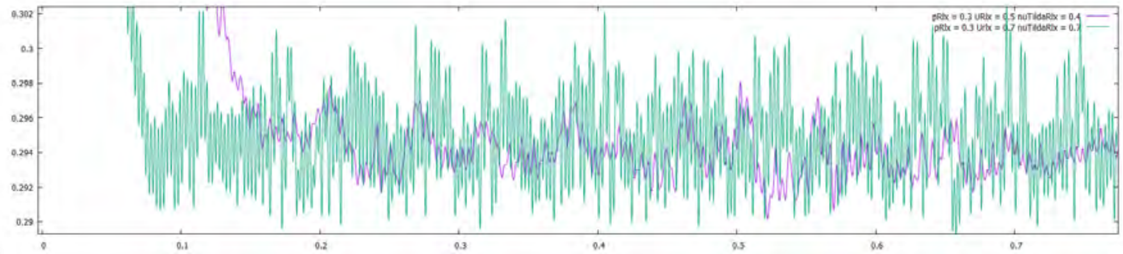

Figure 2.2: *Effect of lower relaxation factors on the oscillation of the drag coefficient. Green = high relaxation factors, purple = low relaxation factors.*

Adjoint Boundary Conditions

The adjoint boundary conditions are derived by setting the multipliers of the partial derivatives of the primal state variables w.r.t. the design variables in the surface integrals in equation 7.22 to zero. As a result, we obtain the following [12]

- Inlet

$$u_{\langle n\rangle} = u_j n_j = -\frac{\partial F_{S_{I,i}}}{\partial p} n_i \tag{2.42a}$$

$$u^{I}_{\langle t\rangle} = \frac{\partial F_{S_{I,k}}}{\partial \tau_{ij}} n_k t^{I}_{i} n_j + \frac{\partial F_{S_{I,k}}}{\partial \tau_{ij}} n_k t^{I}_{j} n_i \tag{2.42b}$$

$$u^{II}_{\langle t\rangle} = \frac{\partial F_{S_{I,k}}}{\partial \tau_{ij}} n_k t^{II}_{i} n_j + \frac{\partial F_{S_{I,k}}}{\partial \tau_{ij}} n_k t^{II}_{j} n_i \tag{2.42c}$$

whereby t^{I}_{i}, t^{II}_{i} are the components of the tangential to the surface vector and $u^{I}_{\langle t\rangle}, u^{II}_{\langle t\rangle}$ are the respective components of the adjoint velocity.

- Outlet

$$u_i v_j n_j + (\nu + \nu_t)\left(\frac{\partial u_i}{\partial x_j} + \frac{\partial u_j}{\partial x_i}\right) n_j - q n_i + \frac{\partial F_{S_{O,k}}}{\partial v_i} n_k = 0, \quad i = 1, 2(,3) \tag{2.43}$$

- Parameterized Wall Boundaries

$$u_{\langle n \rangle} = -\frac{\partial F_{S_{W_p,i}}}{\partial p} n_i \tag{2.44a}$$

$$u^{I}_{\langle t \rangle} = \frac{\partial F_{S_{W_p,k}}}{\partial \tau_{ij}} n_k t^{I}_i n_j + \frac{\partial F_{S_{W_p,k}}}{\partial \tau_{ij}} n_k t^{I}_j n_i \tag{2.44b}$$

$$u^{II}_{\langle t \rangle} = \frac{\partial F_{S_{W_p,k}}}{\partial \tau_{ij}} n_k t^{II}_i n_j + \frac{\partial F_{S_{W_p,k}}}{\partial \tau_{ij}} n_k t^{II}_j n_i \tag{2.44c}$$

Sensitivity Derivatives

The Field Adjoint Equations are to be solved, along with their boundary conditions, in order to yield the required fields which will, in turn, together with the primal fields be used for the computation of the sensitivity derivarives. Having satisfied the FAEs and the adjoint boundary conditions, the remaining terms of equation 7.22 are the following

$$\begin{aligned}\frac{\delta F_{aug}}{\delta b_n} = &- \int_{S_{W_p}} (\tau_{a,ij} n_j - q n_i) \frac{\partial v_i}{\partial x_k} \frac{\delta x_k}{\delta b_n} dS + \int_{S_{W_p}} [n_j r_i \frac{\delta x_k}{\delta b_n} (\frac{\partial p}{\partial x_k} \delta^j_i - \frac{\partial \tau_{ij}}{\partial x_k})] dS + \\ &+ \int_{S_{W_p}} [(p \delta^j_i - \tau_{ij}) r_j] \frac{\delta n_i}{\delta b_n} dS + \int_{S_{W_p}} [(p \delta^j_i - \tau_{ij}) r_j] n_i \frac{\delta (dS)}{\delta b_n} + \int_{S_{W_p}} (u_i R^v_i + q R^p) \frac{\delta x_k}{\delta b_n} n_k dS\end{aligned} \tag{2.45}$$

Chapter 3

Mesh Generation and Shape Morphing

3.1 Mesh Generation

In order to iteratively solve the discretized aforementioned RANS equations, an arbitrary space around the vehicle is created and broken into smaller sub-volumes of arbitrary shape, which are referred to as cells. Each cell of the domain consists of a number of points and edges depending on its geometrical shape, which all together form the mesh of the computational space. The PDEs are, then, solved at each point (or node) of the resulting discretized space using a variant of the SIMPLE algorithm, which is implemented in the environment of OpenFOAM®. Proper representation of the computational domain is crucial when it comes to simulating specific problems which will be compared with real life measurements, tests and experiments. Simulation of the flow around a car and estimation of its drag coefficient is very much in this category of problems, and the specification of the computational domain is not trivial. In every case, deviation of the simulated domain from the one which will be used as a reference for comparison should be known in order to estimate the expected error and to realize the validity of the results. In the simulations that were run during this diploma thesis, the domain is defined by an inlet, an outlet the sides and top of the domain and the ground. The car is positioned 15 m from the inlet and 25 m for the outlet, in order to ensure uniform distribution of the flow at the front of the vehicle and enough space for the wake to develop and dissipate at the rear. The height of the domain is approximately 11.6 m and the width 11 m.

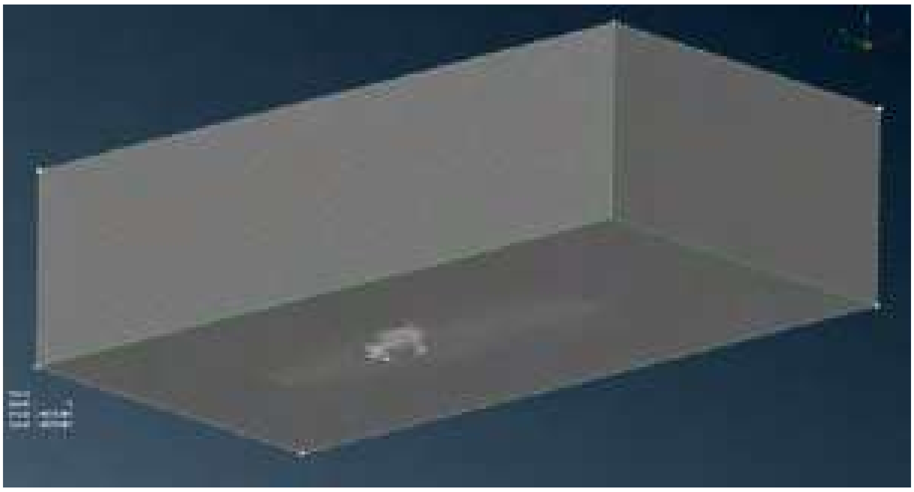

Figure 3.1: *Computational domain.*

The surface mesh consists of 5 million triangular surface elements. The car model features a detailed underbody and closed engine compartment. The volume mesh consists of 36.5 million elements, the majority of which were polyhedral [1].

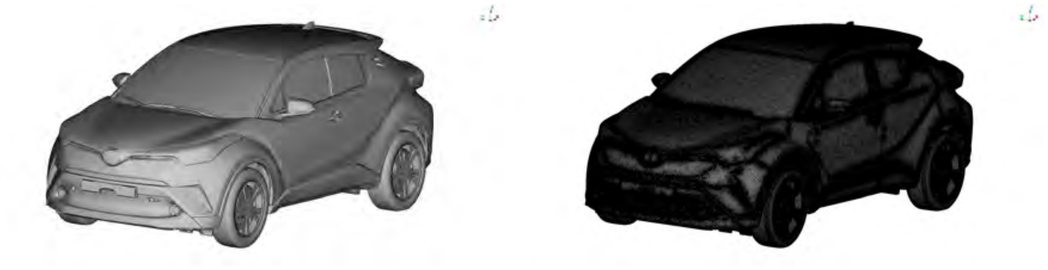

(a) Car geometry

(b) Surface mesh

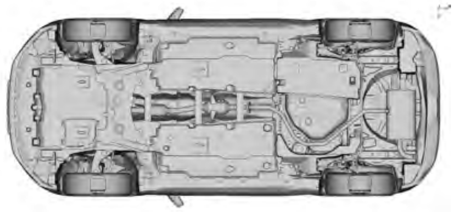

(c) Underbody

Figure 3.2: *Vehicle geometry and surface mesh.*

After the computation of the drag coefficient with three different turbulence models on the full car model was performed as it will in detail be described in the following chapters, a half car model was created. This was done for many purposes the main of

---

[1] The surface mesh was kindly provided by BETA CAE and the software for the necessary further manipulation of it was provided by TME.

which being the symmetry of the solution. When a full model of the vehicle was used, asymmetrical elements of it introduced intense asymmetries in the flow pattern, which of course was later on translated to asymmetries on the sensitivity map. Another issue when dealing with the full model of the vehicle was the simulation time. Especially, when performing optimization loops, the necessary runtime of each simulation deemed the use of a full car mesh almost prohibitive. The model featured also a detailed underbody and closed engine bay, but a significant difference from the original model was the exclusion of the front and read windscreen wipers.

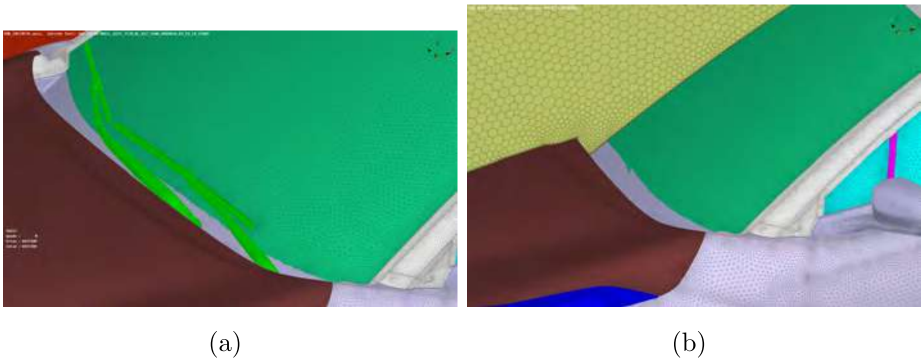
(a) (b)

Figure 3.3: *Car front windscreen detail on full and half car model. Left - full car with windscreen wipers, right - half car without windscreen wipers.*

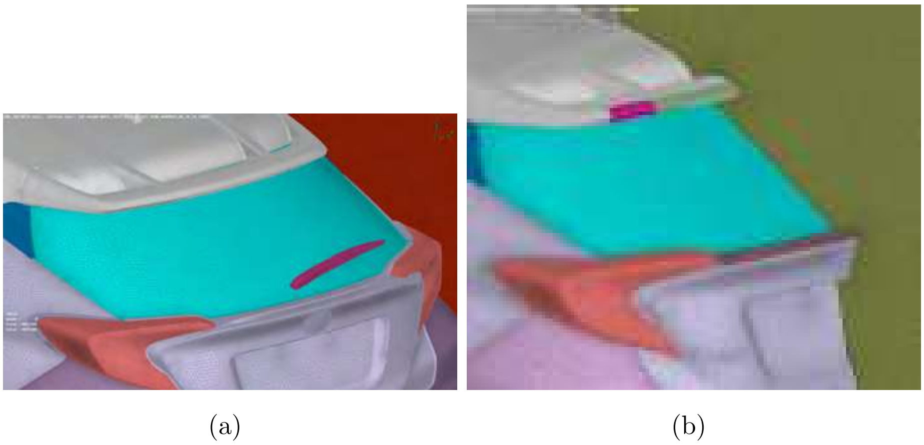
(a) (b)

Figure 3.4: *Car front windscreen detail on full and half car model. Left - full car with windscreen wipers, right - half car without windscreen wipers.*

The half car mesh featured 7 layers and a total of 50 million tetrahedral elements and the simulation time per iteration was reduced by approximately 55%, compared to the full car simulation, while the average y+ value on the surface of the vehicle was roughly 25.

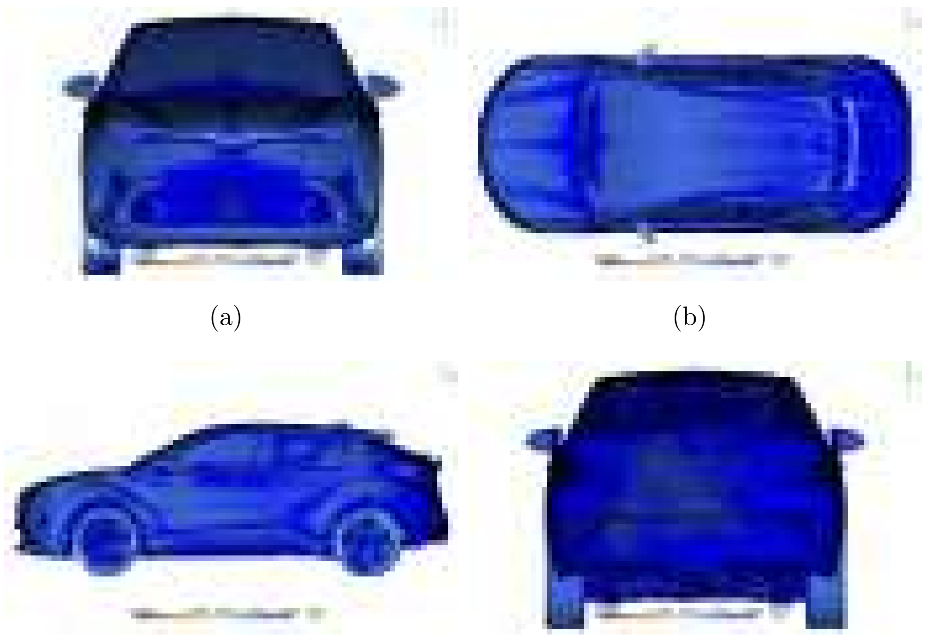

(a) (b)

(c) (d)

Figure 3.5: *Y+. Top Left - Front view, top right - top view, bottom left - left view, bottom right - rear view.*

Computation of the primal and adjoint problem were performed on this mesh as well as a number of optimization loops. Following that, a conversion of this mesh to polyhedral was performed in order to further reduce the required run-time. The polyhedral version of the half car model consists of around 25 million elements and the majority of the optimization loops were executed using this mesh. The mesh has been refined in areas of high importance for the development of the flow, the flow separation and reattachment and all the areas that are expected to have a significant influence on the drag coefficient. These are mainly the area around the whole body of the vehicle, the front and rear part where the wake is expected to appear, the A-Pillar, the side view mirrors and the side windows, the underbody and the spoiler.

3.2 Shape Morphing

The usefulness of the previously calculated sensitivity derivatives in shape optimization problems can be twofold. Firstly, they can be used to compute the sensitivity map i.e. a colorful representation of the derivatives of the objective function w.r.t. the surface-normal displacement of the surface points. This, in simple terms, visually identifies and pinpoints the areas of the body's surface that need to be "pulled" outwards (normal displacement from the solid surface towards the fluid) or "pushed" inwards, in order to minimize the objective function. The magnitude of the displacement is a matter of the engineers judgement in order not to overshoot the local or ultimate minima. Another efficient way to utilize the sensitivity derivatives is to input them in an automated shape morphing tool. The tool needs to have the ability to morph the geometry according to the direction suggested by the sensitivities, from which point the mesh can either be deformed and the nodes will be relocated to their optimal coordinates, or the surface and volume mesh will be regenerated according to the newly suggested shape. The latter highly increases the computational cost of each shape deformation. When the former strategy is applied, i.e. displacement of the mesh nodes according to the direction provided by the sensitivity derivatives, a few important aspects need to be noted and dealt with carefully. Such are the continuity and smoothness of the mesh after the node displacement or even the possibility of mesh overlapping.

The optimization software is coupled with a shape morphing tool able to handle mesh deformation without the need for remeshing the geometry. Both were provided by the PCOpt/NTUA. To do this, a user defined domain confined by a rectangular box is parameterized with volumetric B-Splines. The control points of the B-Splines are also the control points for the mesh displacement, i.e. the Cartesian X,Y and Z displacement of the control points are the design variables in the optimization problem. The control points are then relocated according to the computed sensitivity derivatives and the parameterized space is morphed accordingly, utilizing the advantages of the B-Splines.

During the optimization cycle, the morphing is automatically applied to the geometry and after the algorithm has been initiated, there is no need for any further user input. The properties of the geometry morphing, the constraints for the movement of the control nodes and the step of the objective function optimization are all defined by the engineer prior to the calculation.

The theoretical background of the B-Spline representation and morphing of the domain will be described in detail below.

3.2.1 The Morphing Tool

Mathematical background

The FFD tool as presented in [20] makes use of B–splines defined in $3D$ space, the so–called volumetric B–splines. To understand its properties that give so many advantages to the morpher, a few mathematical details are explained, [40], [47], [20].

B–spline curves

A B–spline is a parameterized curve $x(u)$ that is defined as a linear combination of $b_i \in [0, n]$ control points and B–spline basis functions $U_{i,p}(u)$ with a degree of p [40]. The curve is described as

$$x(u) = \sum_{i=0}^{n} U_{i,p}(u) b_i \tag{3.1}$$

Equation 3.1 can also be used to obtain the $y(, z)$ coordinates of a monoparametric curve in $2D(, 3D)$. A B–spline is a piecewise polynomial function of degree p. In order to define the basis function $U_{i,p}$, a set of knots which is a non decreasing sequence, known as the knot vector, $\xi_i, i \in [0, m], m = n + p + 1$ must first be defined. The knots $\xi_{p+1}, \ldots, \xi_{m-p-1}$ are called internal knots. The uniform knot vector is given as

$$\xi = [\underbrace{0, \ldots, 0}_{p+1}, \frac{1}{N}, \ldots, \frac{N-1}{N}, \underbrace{1, \ldots, 1}_{p+1}] \tag{3.2}$$

where $N = n - p + 1$. This knot vector results to closed curves, this means that we get curves that pass through the first and last control points. The number of control points has to exceed the curve degree by at least one, i.e. $n \geq p$. The basis function is given by

$$U_{i,0}(u) = \begin{cases} 1 & \text{if } \xi_i \leq u < \xi_{i+1} \\ 0 & \text{elsewhere} \end{cases} \tag{3.3}$$

$$U_{i,p}(u) = \frac{u - \xi_i}{\xi_{i+p} - \xi_i} U_{i,p-1}(u) + \frac{\xi_{i+p+1} - u}{\xi_{i+p+1} - \xi_{i+p}} U_{i+1,p-1}(u) \tag{3.4}$$

During the computation of the basis functions values, the quotient $\frac{0}{0}$ may appear and its value is defined to be 0. Two consecutive knots define a knot span.

The degree p determines the extent of the effect of control points. In other words, each basis function (and consequently, each control point) is affecting only points with a parametric coordinate residing in the $p+1$ knot spans defined by $[\xi, \xi_{i+p+1})$. This gives B–splines curves the desirable property of local support, i.e. a certain part of the curve can be altered by keeping the rest of the curve intact. The range of locality can be controlled by changing the curve degree p, where smaller p values correspond to more localized support. So, control points have a stronger attraction to the curve corresponding to the lower degree basis functions, as it can also be seen in fig. 3.6.

Knots can have a multiplicity greater than one [40], i.e. equation 3.1 is therefore valid even if some of the knots occur several times. Since B–splines curves are piecewise polynomial functions, they are continuously differentiable in the interior of each knot span. The curve continuity is finite only at the knots. A curve is $p - k$ times differentiable at a point where k duplicate knot values occur. This means that if the knots are all distinct, then a linear spline will be continuous, a quadratic spline will also have a continuous first derivative, while for a cubic spline even the second derivative will be continuous. Predetermining the curve (or surface in $3D$) continuity is a very desirable property for a mesh movement algorithm as well, since the deformed shapes are guaranteed to have a user–defined level of surface continuity, facilitating the manufacturing process.

Volumetric B–splines

The volumes in B–spline form based on B–spline basic functions are now analyzed [20]. It is defined with all attributes as B–spline curve, however, here there are three parameters u, v, w and the definition is similar to the case of curves. The properties of B–spline volumes are similar to the properties of B–spline curves.

The cartesian coordinates $\mathbf{x} = [x_1, x_2, x_3]^T = [x, y, z]^T$ of a CFD mesh point that is chosen to be parameterized, which means that it is residing inside the boundaries defined by the control grid, are given by

$$x_m(u, v, w) = \sum_{i=0}^{I} \sum_{j=0}^{J} \sum_{k=0}^{K} U_{i,pu}(u) V_{j,pv}(v) W_{k,pw}(w) b_m^{ijk} \tag{3.5}$$

where $\mathbf{u} = [u_1, u_2, u_3]^T = [u, v, w]^T$ are the mesh point parametric coordinates,U, V, W are the B–splines basis functions and pu, pv, pw their respective degrees. $b_m^{ijk}, m \in [1, 3], i \in [0, I], j \in [0, J], k \in [0, K]$, signifies the cartesian coordinates of the ijk–th control point of the $3D$ structured control grid, where I, J and K are the number of control points per control grid direction.

As long as the parametric coordinates $\mathbf{u}$ of any parameterized point are known, the computation of its cartesian coordinates is straightforward, at a negligible computational cost. Mesh parametric coordinates can be computed with accuracy, since a mapping from $\Re^3(x, y, z) \rightarrow \Re^3(u, v, w)$ is required. This means that volumetric B–splines can reproduce any geometry to machine accuracy.

Given the control points position, the knot vectors and the basis functions degrees, the parametric coordinates (u, v, w) of a point with cartesian coordinates

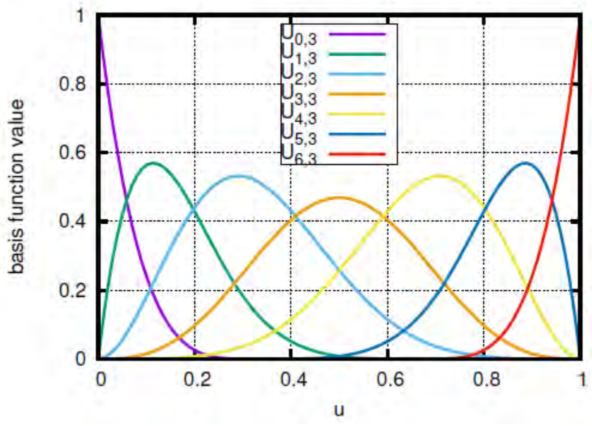

(a) Basis functions values of degree $p = 4$

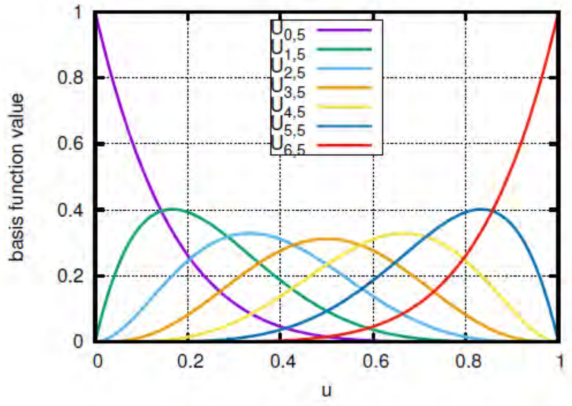

(b) Basis functions values of degree $p = 6$

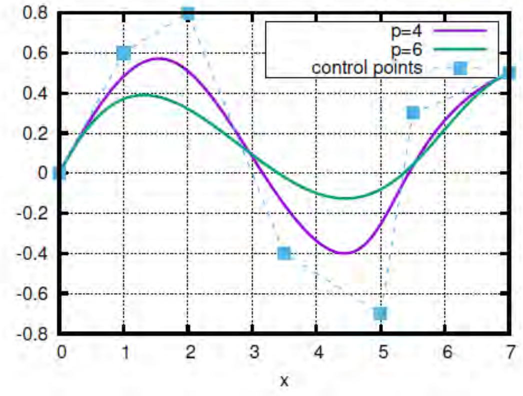

(c) B–splines curves generated by the top row basis functions for the given set of control points

Figure 3.6: *On the top row graphs, for each u, the sum of the basis functions values equals unity. On the third graph, two B–splines curves generated by multiplying the basis functions in the top graphs with the control points depicted by the control polyline. The cartesian coordinates of the curve are given by eq. 3.1, for* $b^i = [b^i_x, b^i_y]^T, 2D$ *vector of control points. The curve corresponding to higher degree basis functions is less strongly attracted by the control points, but a larger part of it is affected. Lower degree functions influence a smaller part of the curve, though more intensively.*

$\mathbf{r} = [x_r, y_r, z_r]^T$ can be computed by solving the system of equations

$$\mathbf{R}(u,v,w) = \begin{bmatrix} x(u,v,w) - x_r = 0 \\ y(u,v,w) - y_r = 0 \\ z(u,v,w) - z_r = 0 \end{bmatrix} \tag{3.6}$$

where $x_m(u,v,w)$ are computed through eq.3.5 based on the given $\mathbf{b}$ values. The 3×3 system of eq.3.6 can be solved independently for each parameterized mesh point numerically, using the Newton–Raphson method, for which is necessary to compute and invert the Jacobian $\frac{\partial x_m}{\partial u_j}, m, j \in [1,3]$. The Jacobian matrix is computed analytically through a closed form expression resulting by differentiating eq. 3.5 with respect to the components of $\mathbf{u}$. Since the evaluation of the parametric coordinates of each point is independent from any other mesh point, this phase may run in parallel.

The aforementioned process has to be done only once and can be seen as the "training phase" of the method. Then, after moving the control points, the cartesian coordinates of each (internal of boundary) mesh point that resides within the control grid can easily be computed through eq. 3.5 at a very low cost. In addition, since x_m depends only on (u,v,w) (which remain unchanged whatever the change in $\mathbf{b}$ might be) and $\mathbf{b}$, the deformed meshes are step–independent. This means that, for a given final control points position, the same mesh quality will be obtained independent of the number of steps taken to reach that position. This is not, for instance, the case for RBF–based or Laplacian–based mesh movement algorithms [20].

3.3 Optimization Algorithm

To perform an automated CFD shape optimization loop for the car shape, as it is mentioned before, the in–house adjoint solver coupled with the in–house morpher are used [20]. The steps of the shape optimization algorithm are listed below:

1. Define the $3D$ space (box) to enclose the part of the geometry to be optimized. Moreover, define the control points number and the basis functions degree according the logic explained above. A structured control grid is created.
2. Find the CFD mesh points residing within the control grid. These points are to be parameterized and then displaced, according to the control points displacement.
3. Compute the parametric coordinates for each of the points found in step 2. The computational cost of this step increases with the number of control points

and the number of the mesh points to be parameterized.

4. Solve the flow equations.
5. Compute the objective function value and apply the termination criterion.
6. Solve the adjoint equations.
7. Compute the objective function gradient w.r.t. the boundary CFD mesh nodes to be displaced, i.e. $\frac{\delta F}{\delta x_m}$ (surface sensitivities).
8. Project the surface sensitivities to control points in order to compute the control points sensitivities,

   $$\frac{\delta F}{\delta b_i} = \sum_{j=1}^{n_p} \sum_{m=1}^{3} \frac{\delta F}{\delta x_m^j} \frac{\delta x_m^j}{\delta b_i} \tag{3.7}$$

   where n_p is the number of boundary mesh points to be displaced. In the general case, the control points are allowed to move along all the three directions, however the user has the ability to confine the movement of specific points in specific directions. One of the beneficial properties of B–splines is that smoothing is included in the nature of the basis functions. Consequently, no smoothing of the computed sensitivities is required. The quantity $\frac{\delta x_m^j}{\delta b_i}$ is computed analytically by differentiating the linear eq. 3.5 w.r.t. b_i.
9. Update the control point coordinates. In this thesis, the steepest descent formula

   $$b_i^l = b_i^{l-1} - \eta \frac{\delta F}{\delta b_i}\bigg|_{l-1} \tag{3.8}$$

   is used where η is a positive number that defines the step of the descent and l is the current iteration.
10. Compute the new surface and volume mesh points positions through eq. 3.5, using the already computed parametric coordinates u associated with each one of them.
11. Move to step 4.

Chapter 4

Solution of the Flow Problem

In this chapter, the solution of the mean flow equations together with the turbulence model equations, i.e. the primal problem will be presented. The different flow fields obtained from the three different turbulence models (Spalarts-Allmaras, $k-\omega$ SST and $k-\epsilon$) used for the closure of the RANS equations will be presented and their ability to accurately predict the flow evolution around the car body will be discussed.

4.1 Comparison of the Three Turbulence Models

4.1.1 The Computed Drag Coefficient

As discussed in the previous chapters, each turbulence model is identifiable by a set of characteristics that deem it appropriate or not for certain applications. As such, the comparison of the obtained flow fields with experimental wind tunnel measurements that were conducted during this thesis [1] showed that two of the three turbulence models used in this study -the $k-\omega$ SST and the Spalart-Allmaras- proved to give results of good accuracy in this application. The $k-\epsilon$ turbulence model on the other hand appears to have some drawbacks when it comes to the accurate prediction of the shear stresses on the wall and consequently the flow separation, which is an important feature of the flow development around the car. In what follows, a comparison between the computed drag coefficient and flow fields from the three models will be made. With a quick glance at the comparison of the results between the three turbulence models one can clearly notice the similarities between the $k-\omega$ SST and the Spalart-Allmaras models, which is translated in a very close prediction of the drag coefficient from the two. In contrast, the picture is

---

[1] Measurements from the wind tunnel experiment conducted by TME are not included in this thesis due to confidentiality reasons.

much different with the $k-\epsilon$ turbulence model, in which case the flow pattern and consequently the predicted drag coefficient is notably different from the other two. In figure 4.1, comparison between the drag coefficient obtained by the three models is shown. The values have been normalized by the averaged C_D value obtained from the $k-\epsilon$ model.

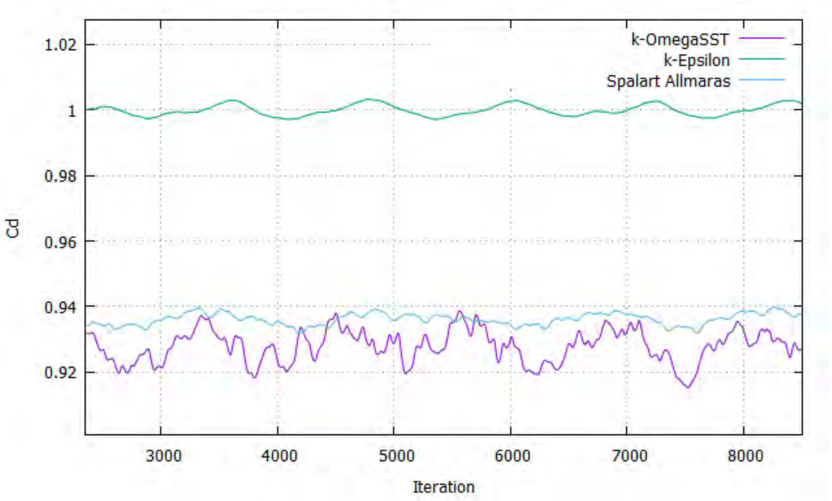

Figure 4.1: *Normalized drag coefficient of the three turbulence models over the last 5000 iterations of the solution. Averaging of the fluctuating value was done to obtain the final mean* C_D.

In what is shown in figure 4.2, the comparison between the three models in made on the prediction of the local drag coefficient along the length of the vehicle. The contribution of each part of the vehicle along its longitudinal axis can be seen for each of the three models. It appears that the $k-\omega$ SST and the Spalart-Allmaras results correlate very well along the whole length of the vehicle whereas the $k-\epsilon$ model, when compared with the other two, seems to under-predict the drag force close to bonnet, the cowl area and the A-Pillars of the vehicle, and to overshoot at the rear part. The final drag value acquired by the $k-\epsilon$ model is roughly 7% higher than the two other models. The experimental results, which cannot be disclosed, show that the $k-\omega$ SST and the Spalart-Allmaras models give quite accurate predictions wheras the $k-\epsilon$ model lags behind.

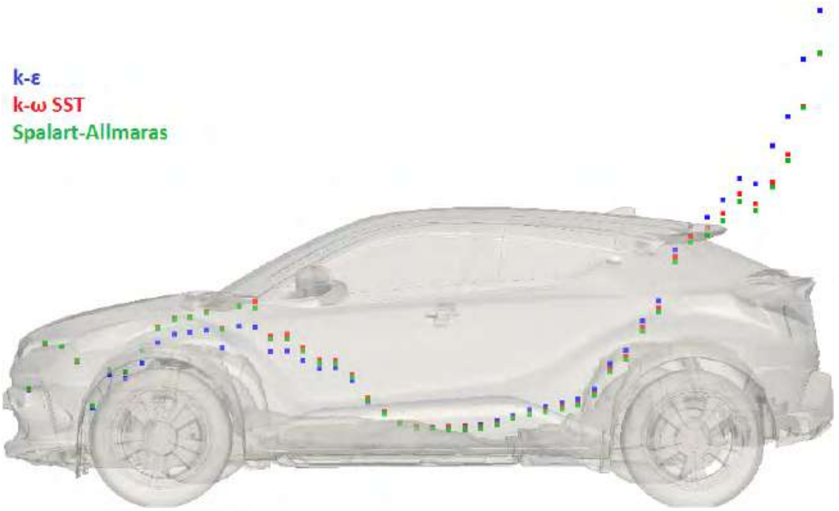

Figure 4.2: *Local drag coefficient comparison among the three turbulence models. Blue = $k-\epsilon$, Red = $k-\omega$ SST, Green = Spalart-Allmaras.*

As mentioned previously, the drag coefficient obtained from the $k-\omega$ SST model is within a 1% difference from the Spalart-Allmaras model and a 7% difference from the $k-\epsilon$ model. This was expected, since the $k-\omega$ SST model is a crossbreed of the original $k-\omega$ model established by Wilcox [6], [7], [8] and the standard $k-\epsilon$ model. The fact that the $k-\omega$ SST is able to compute a different flow pattern that is closer to the experimental results confirms the advantages of this mixing between the two models. The fluctuation of the converged drag coefficient value from this model is, however, slightly more intense than the other two cases. The magnitude of the C_D oscillation when calculated with the $k-\omega$ SST model is roughly 2% of its mean value, whereas the two other models converge with approximately a quarter of this oscillation (figure 4.3).

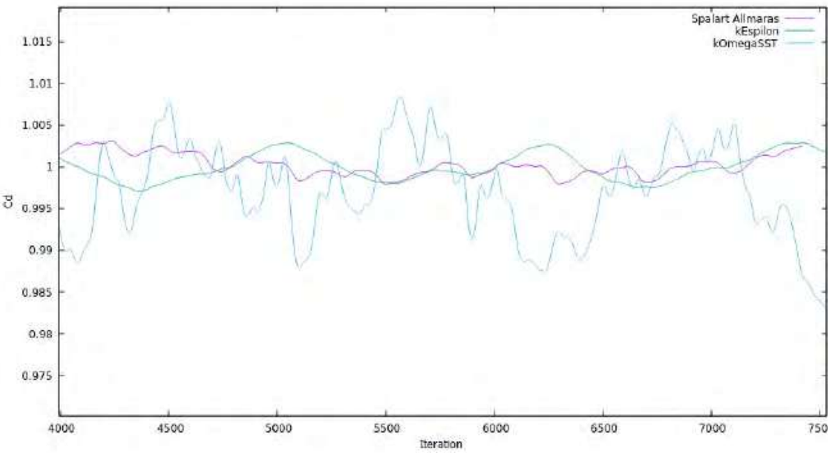

Figure 4.3: *Normalized drag coefficient over the iterations of the numerical solution - Comparison of the three turbulence models.*

The influence of this fluctuation to the adjoint calculation might prove to be important and the side effect to the optimization process is twofold. Firstly, it is linked to an analogous fluctuation of the turbulent variables which, as previously discussed can have a negative impact to the stability of the adjoint calculation and hinder its convergence. Secondly, the purpose of this study is the minimization of the drag coefficient, which is achieved by apt shape morphing as indicated by the sensitivity derivatives. In external aerodynamic optimization problems of cars and most other similar applications where design and styling is involved, the freedom and allowance for shape modification is extremely tight. This results in a small optimization margin from each cycle, around 1%. If the fluctuation of the computed drag coefficient is 2%, this can make it hard to identify the actual magnitude of the reduction of the objective function at each optimization cycle. A minimal fluctuation of the objective function is, therefore, desired. There are numerical techniques to minimize this fluctuation -which can however sometimes influence the accuracy of the solution-, but when it comes down to the comparison between two turbulence models with similar quality and accuracy of results, it is sensible to opt for the one with the least fluctuating solution.

4.1.2 The Computed Flow Fields

The computation of the drag force applied on the car is partly caused by the pressure difference between the front and rear part of the car. Results from this study indicate that the contribution of the pressure drag to the total drag of the car is approximately 90% (around one order of magnitude higher than the friction drag). The lower the value of the static pressure on the rear part of the car, the higher the aforementioned pressure difference. Consequently the drag force applied on the car increases. In figure 4.4, the static pressure on the rear surface of the car can be seen, whereby blue areas indicate high negative values of pressure.

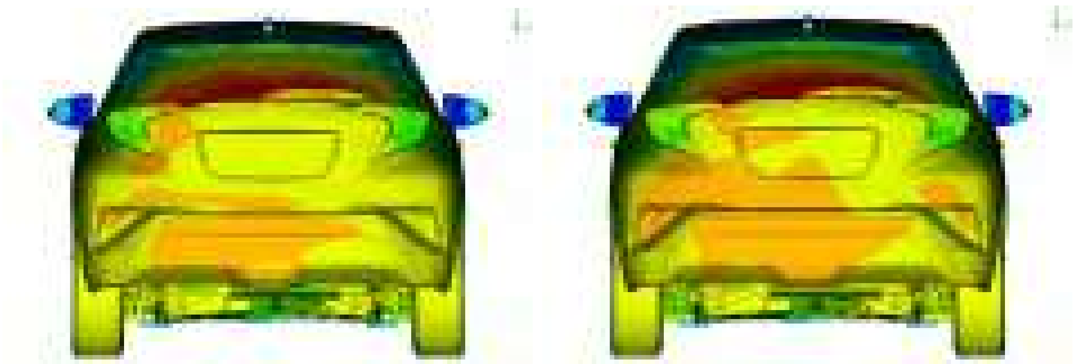

(a) Spalart-Allmaras (b) k-ω SST

(c) k-ϵ

Figure 4.4: *Static pressure on the back side of the vehicle. It can be seen that the pressure distribution in the rear part, as computed by the* $k-\epsilon$ *model, (bottom figure), is significantly lower, which explains the higher value of the computed* C_D. *Pressure range [0:-300Pa]*

In general, the flow field obtained from the Spalart-Allmaras model is in a relatively good agreement with that of the $k-\omega$ SST model and the wind tunnel results. Both model predictions of the separation at the rear part of the vehicle are very similar. In figures 4.5(a), 4.5(b) and 4.5(c), the shear stress on the surface of the car computed by the three models can be seen. This gives a good indication of where the flow separation takes place, which is where the wall shear stress becomes zero (the area where the transition from green to blue color occurs).

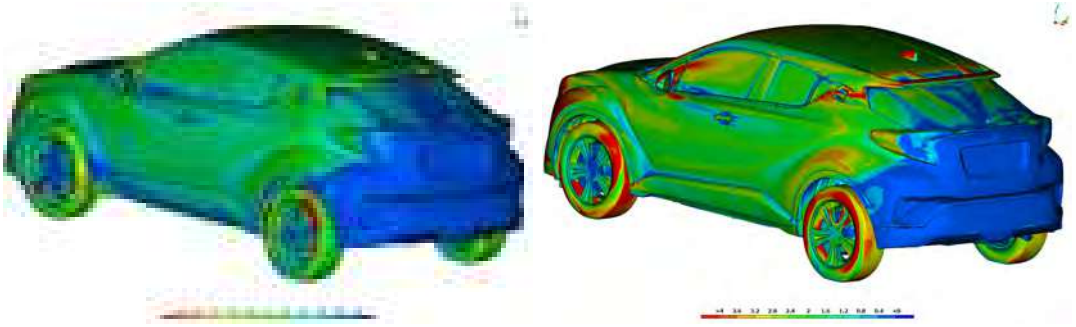

(a) Spalart-Allmaras (b) $k-\omega$ SST

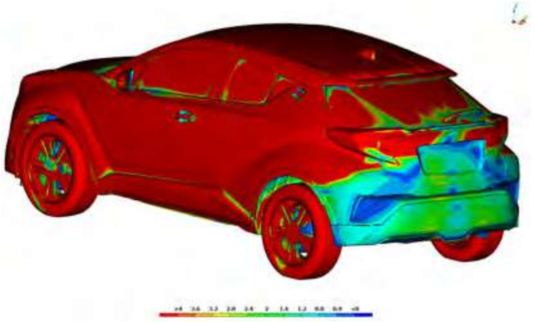

(c) $k-\epsilon$

Figure 4.5: *Wall shear stress, rear side view. High to low values - Red to blue.*

The same can be seen from the static pressure distribution on the rear part of the vehicle, figure 4.4, in which the separation of the flow appears to occur around the tail lights, from which point on the wake is formed.

From figures 4.6(a), 4.6(b) and 4.6(c) the formation of two clear, contra-rotating vortices on the YZ plane drawn 0.5m behind the vehicle can be observed. Further away, towards the rear of the car, these vortices can be seen moving closer to the ground. In figures 4.7(a), 4.7(b) and 4.7(c), the Line Integral Convolution (LIC) representation [2] of the streamlines of the flow field can be seen, in which the two vortices appear having a lower velocity magnitude and being closer to the ground.

---

[2] The LIC representation is a way of visualizing the flow field by coloring the pixels of the image that reside on the same streamline of the flow with similar levels of the greyscale palette [46].

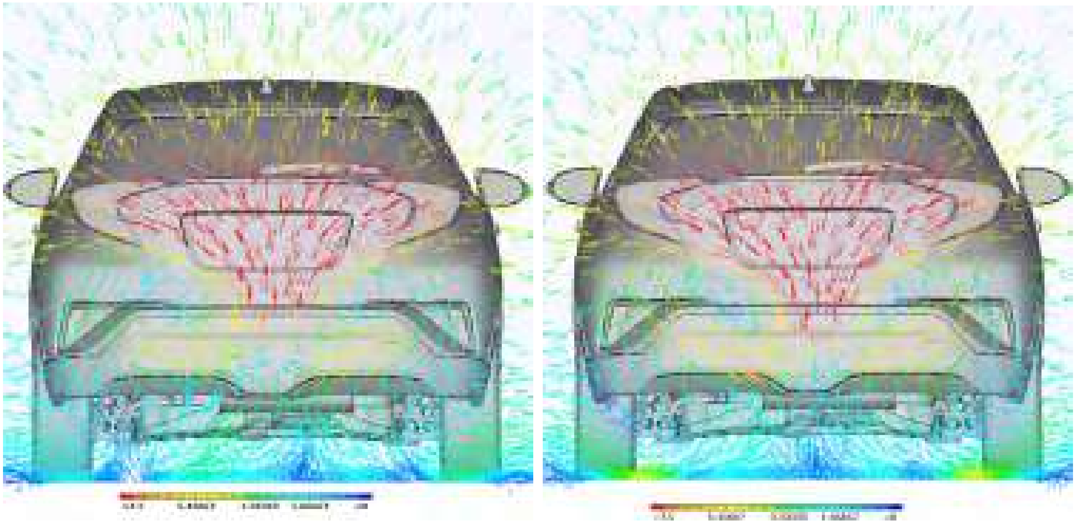

(a) Spalart-Allmaras (b) $k - \omega$ SST

(c) $k - \epsilon$

Figure 4.6: *Transversal velocity vector field on the YZ plane 0.5m behind the rear bumper.*

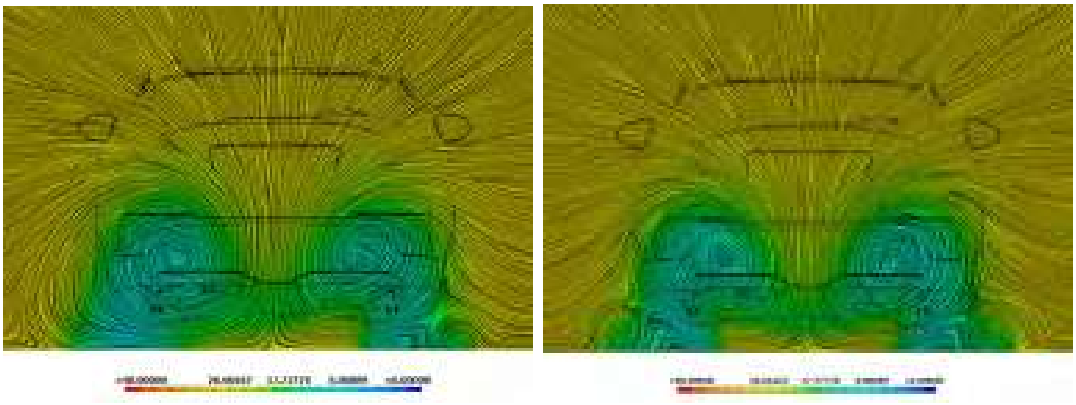

(a) Spalart-Allmaras

(b) $k-\omega$ SST

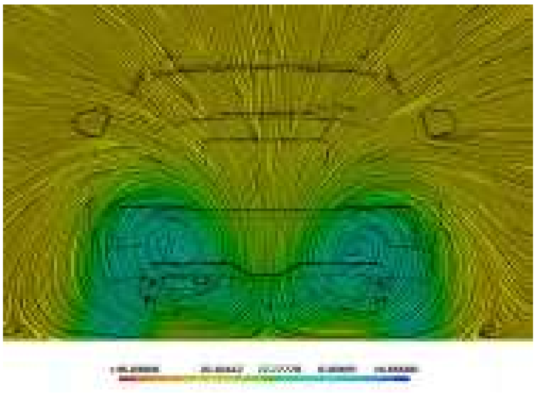

(c) $k-\epsilon$

Figure 4.7: *Transversal flow field on the YZ plane. LIC velocity stream 2.5m behind the rear bumper.*

On the ZX plane, the image of the dead air region immediately behind the tail of the vehicle is again that of two contra-rotating vortices, this time one being significantly larger than the other, as it can be seen in figures 4.8(a), 4.8(b), 4.9(a) and 4.9(b) of the computed velocity field from the Spalart-Allmaras and the $k-\omega$ SST models. This is the typical image for the flow behind a bluff body like the one used for this study, i.e. a hybrid between a notchback and a hatchback. For a vehicle of this type, as reported in [3] the results of the CFD analysis with the Spalart-Allmaras and $k-\omega$ SST turbulence models correlates very well with the theoretical expected flow pattern and the experimental measurements which, unfortunately, cannot be included in this thesis.

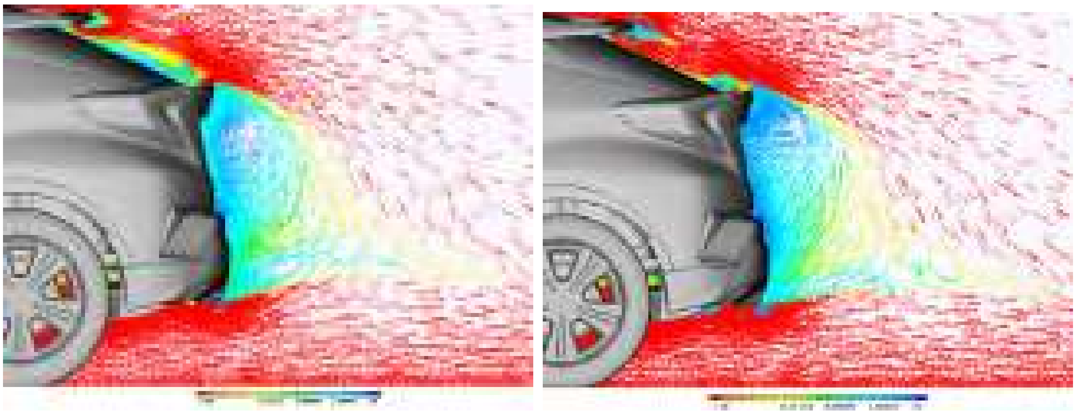

(a) Spalart-Allmaras (b) $k - \omega$ SST

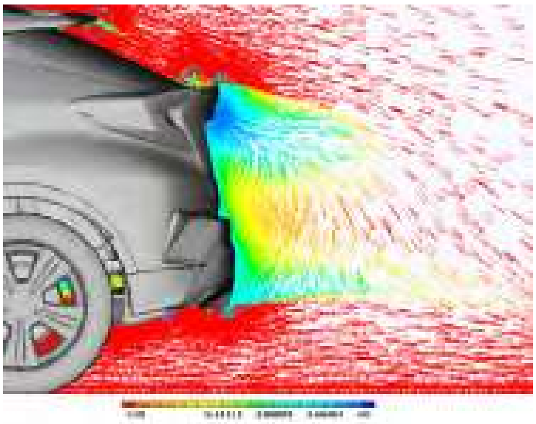

(c) $k - \epsilon$

Figure 4.8: *Transversal velocity vector field on the ZX plane.*

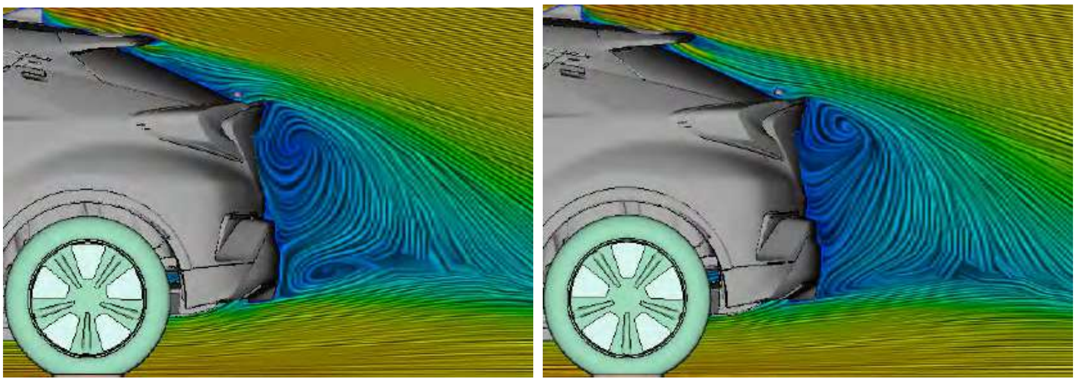

(a) Spalart-Allmaras

(b) $k-\omega$ SST

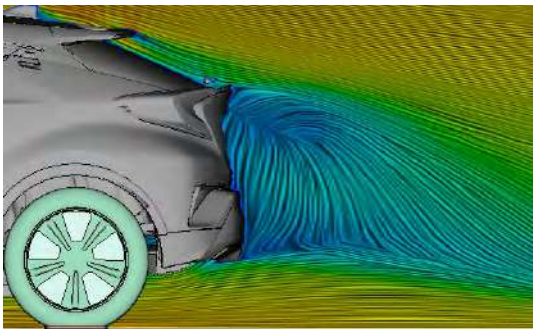

(c) $k-\epsilon$

Figure 4.9: *Transversal LIC velocity stream on the ZX plane.*

The slant angle ($\phi = 24°$) of the vehicle is such [1] that the flow coming from the roof is forced to separate relatively early, as it can be seen from figure 4.5, avoiding low static pressure to appear at the rear, as it can be seen in figure 4.4. This, in combination with the fact that the spoiler at the trailing edge of the roof is partly hollow, forces the complete separation to occur at a lower point, after the second spoiler located at the end of the trunk. As a result, the dead air region behind the vehicle and, subsequently, the volume of the two vortices, is much smaller and shorter, again as seen in the experimental measurements [2]. This fact has an immediate effect on the shape morphing suggestions by the adjoint calculated sensitivity derivatives, as it will be discussed later on.

In the case of the $k-\epsilon$ turbulence model, the flow evolution at the rear part of the vehicle is much different from the other two turbulence models and, also, from the wind tunnel test results and other experimental data from the literature [1], [2], [3]. The flow remains attached to the body of the vehicle along a significant part of the trunk and rear bumper including the taillights, as it can be seen in figure 4.5(c) of the wall shear stress. This results in the appearance of lower static pressure at these areas compared to the two other models, as it can be seen in figure 4.4, which partly explains the higher value of the drag coefficient obtained by the $k-\epsilon$ model.

Figure 4.4 features the static pressure distribution at the rear part of the vehicle in the pressure range of 300 Pascal. The intense blue areas are dominating a large part of the rear surface of the vehicle indicating an attached flow.
Also, as computed by the $k-\epsilon$ model, the wake appears much different in size and shape. The iso-surfaces for $Cp_t = 0$ from the three turbulence models, which are shown in figures 4.10(a), 4.10(b) and 4.10(c), give an image of the wake behind the car. It can be noticed that in the case of the $k-\epsilon$ model, the yellow surface takes up a smaller part of the domain, indicating a smaller area of pressure loss around the vehicle. This can be attributed to the higher shear stresses and, therefore, velocity computed close to the wall. The total pressure coefficient on the XZ plane in the wake behind the car can be seen in figures 4.11(a), 4.11(b) and 4.11(c).

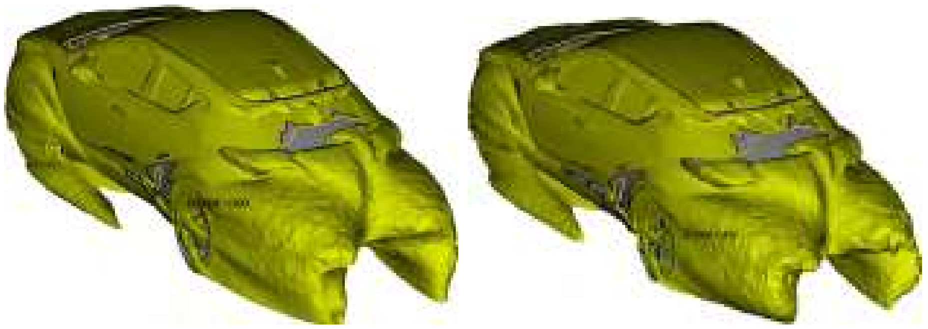

(a) Spalart-Allmaras (b) $k-\omega$ SST

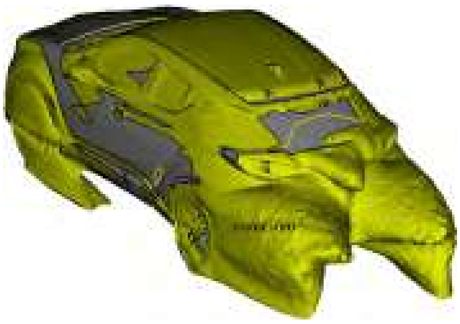

(c) $k-\epsilon$

Figure 4.10: *Iso-surface* $Cp_t = 0$.

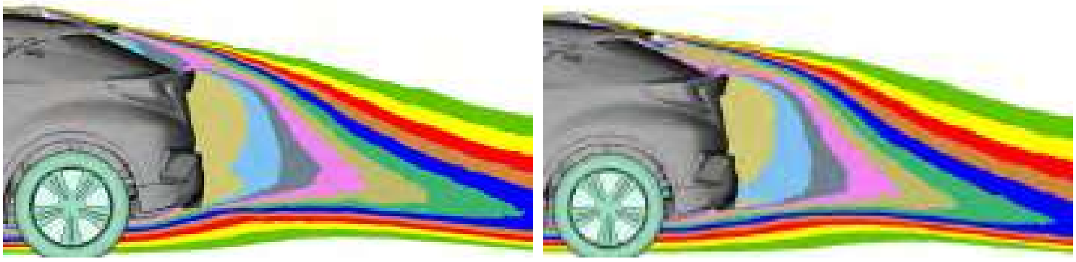

(a) Spalart-Allmaras

(b) $k-\omega$ SST

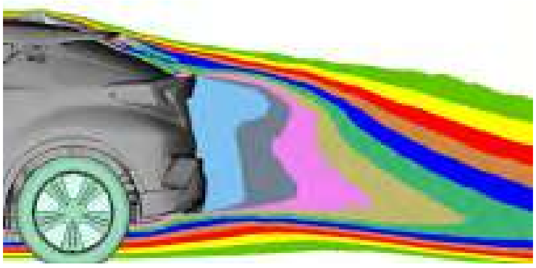

(c) $k-\epsilon$

Figure 4.11: *Total pressure coefficient on the XZ plane.*

In contrast to the $k-\omega$ SST and the Spalart-Allmaras models, the $k-\epsilon$ model computes a totally different vortex generation in the wake of the vehicle. On the ZX plane, where typically for this type of vehicle a pair of vortices are expected to appear, [1], [2], [3], this is not the case for the results obtained by the $k-\epsilon$ model.

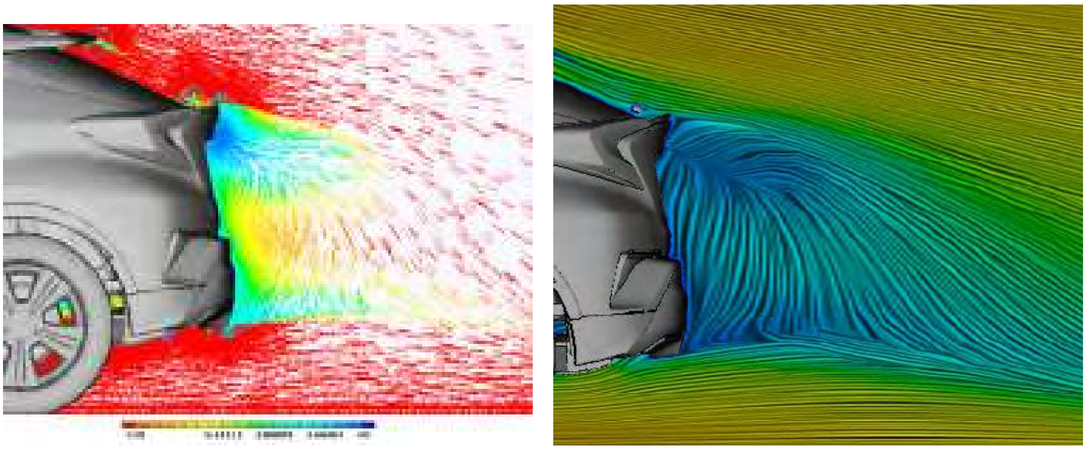

(a)

(b)

Figure 4.12: *Transversal flow field on the ZX plane. Left - Velocity vector field 0.5m behind the rear bumper. Right - LIC velocity stream 2.5m behind the rear bumper. Spalart-Allmaras turbulence model.*

The flow that remains attached for a larger part of the vehicle, figure 4.5(c), comes with a high velocity from the sides around the tail lights towards the center of the rear trunk. From this point, it is separated and one part of it moves upwards whereas the other part forms a downwash all the way to the lowest part of the rear bumper. A small, counter-clockwise vortex is, then, formed at the lower part of the rear bumper when this stream meets the flow coming from the diffuser.

According to the $k-\epsilon$ model, the flow remains partially attached to the rear bumper and, in general, the picture of the flow given is not realistic for this type of vehicle. This suggests that the $k-\epsilon$ model failed to accurately predict the separation and a not that correct pressure and velocity distribution around the vehicle is produced.

Chapter 5

Solution of the Adjoint Problem

5.1 Sensitivity Maps

The previously analyzed primal solutions from the three turbulence models were used as input to the adjoint problem in order to compute the sensitivity derivatives. The sensitivity map is a very useful way of utilizing of the surface sensitivities (sensitivity derivatives of the objective function w.r.t. the normal displacement of the surface mesh points) in optimization problems of external aerodynamics. It pinpoints the areas of the vehicle that exhibit the highest optimization potential, as well as the direction in which these areas need be morphed in order to minimize the target function. This information is very valuable in industrial shape optimization problems. In the implementation of OpenFOAM®, surface normal vectors of a boundary face are always pointed in the direction from the fluid to the solid surface. Taking this into account, a negative value of the derivative of the objective function w.r.t the surface normal displacement of the vehicle's surface indicates a decrease of the objective function if this surface is pushed inwards, i.e. in the direction from the fluid to the solid surface. The opposite applies if the sign of the sensitivity derivative is positive, indicating a decrease of the C_D if the face is pulled outwards, from the solid surface towards the fluid. The magnitude of the sensitivity derivative at each point quantifies the impact of the displacement to the objective function.

The sensitivity maps obtained from the three turbulence models have of course a significant variation, which is proportional to the variation of the three flow fields from the $k-\epsilon$, the $k-\omega$ SST and the Spalart-Allmaras models that were previously discussed. Given, therefore, the fact that the $k-\epsilon$ model gave, to some extent, a different flow pattern around the vehicle compared to the other two, the sensitivity maps are also expected to vary. In general, the most sensitive areas are expected to be around the area of the separation and reattachment of the flow. The results are presented in what follows.

What is more, the influence of turbulence in such flow problems is decisive for the quality and accuracy of the results and has an immediate impact on the sensitivity derivatives. An investigation is, therefore, also carried out between the resulting sensitivity map from a flow problem that was solved with 2^{nd} order discretization of the turbulence equations and one that was solved with 1^{st} order.
An aspect that will also be investigated using the three sensitivity maps is the impact of the adjoint computation on the diversity of the three flow solutions obtained from the different turbulence models. In other words, this will try to measure the extent to which the adjoint solution amplifies -or not- the differences in the flow fields that are used as input for its computation. Other influencing factors on the construction of the sensitivity map such as the symmetry of the results will also be addressed.

5.1.1 Comparison of the Sensitivity Maps from the Three Turbulence Models

A few observations can be made already by a glance at the back side view of the three sensitivity maps which can be seen in figure 5.1, the most obvious being the major differences between the one based on the $k - \epsilon$ model and the other two. In what follows, the figures of the sensitivity maps are in accordance with the "push/pull" terminology, whereby blue colored areas shall be pushed inwards for decreasing the drag and red areas shall be pulled outwards.

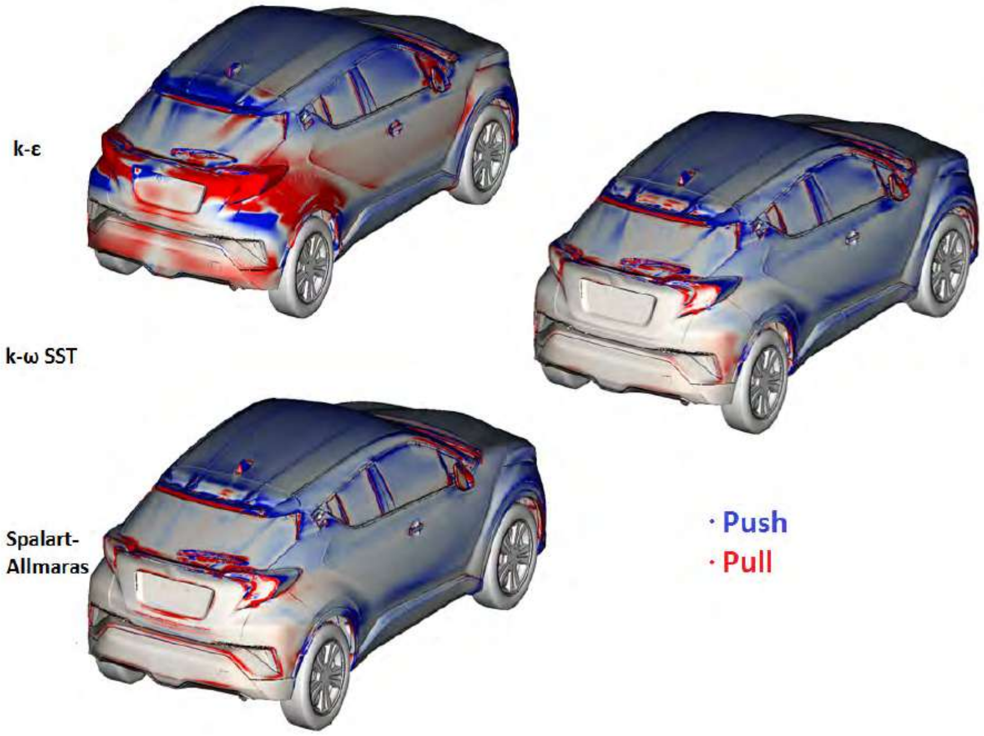

Figure 5.1: *Sensitivity map comparison of the three turbulence models - Back side view. Blue colored areas should be pushed inwards for drag reduction.*

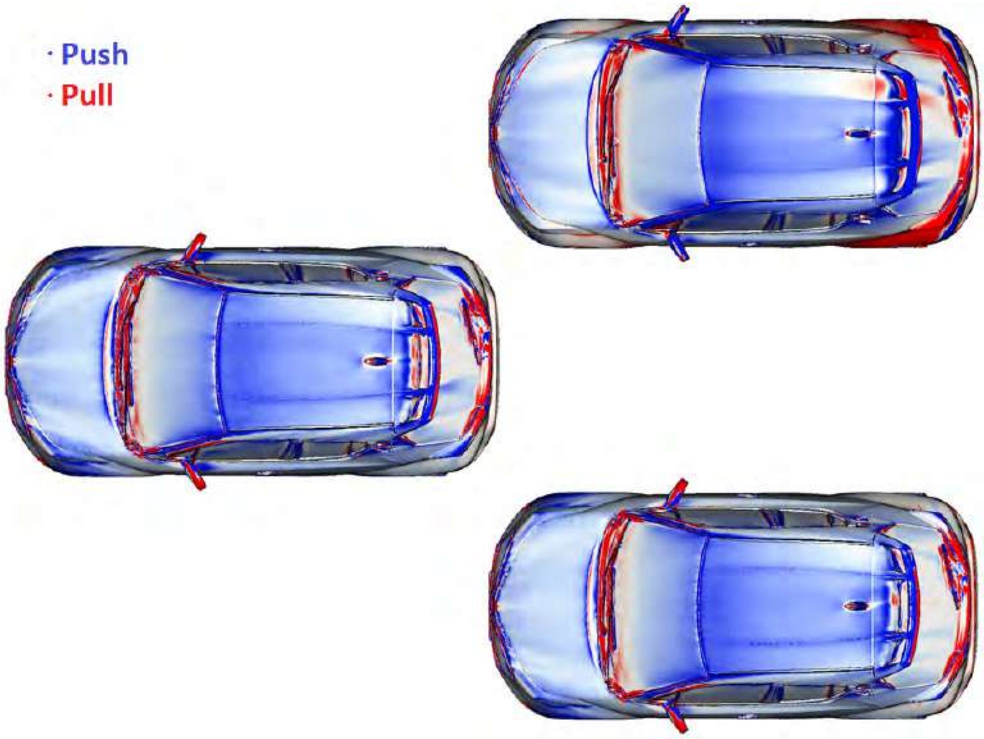

Figure 5.2: *Sensitivity map comparison of the three turbulence models - Top view. Blue colored areas should be pushed inwards for drag reduction.*

In figures 5.1 and 5.2, it is clear that the differences between them are not only quantitative but, also, qualitative. This means that in a significant portion of the vehicles surface the sensitivity derivatives have opposite sign and, therefore, suggest opposite directions for shape morphing. It is obvious that these differences emerge from the different primal flow fields and, particularly, the correct or erroneous prediction of flow attachment and separation, indicating the significance of the proper modeling and computation of turbulence. In general, the most profound differences appear on the sides and of course the rear part of the vehicle, where turbulent phenomena of all the length scales govern the flow and the ability of each model to accurately predict its evolution is challenged. On the front and top of the vehicle, differences are not so intense and obvious.

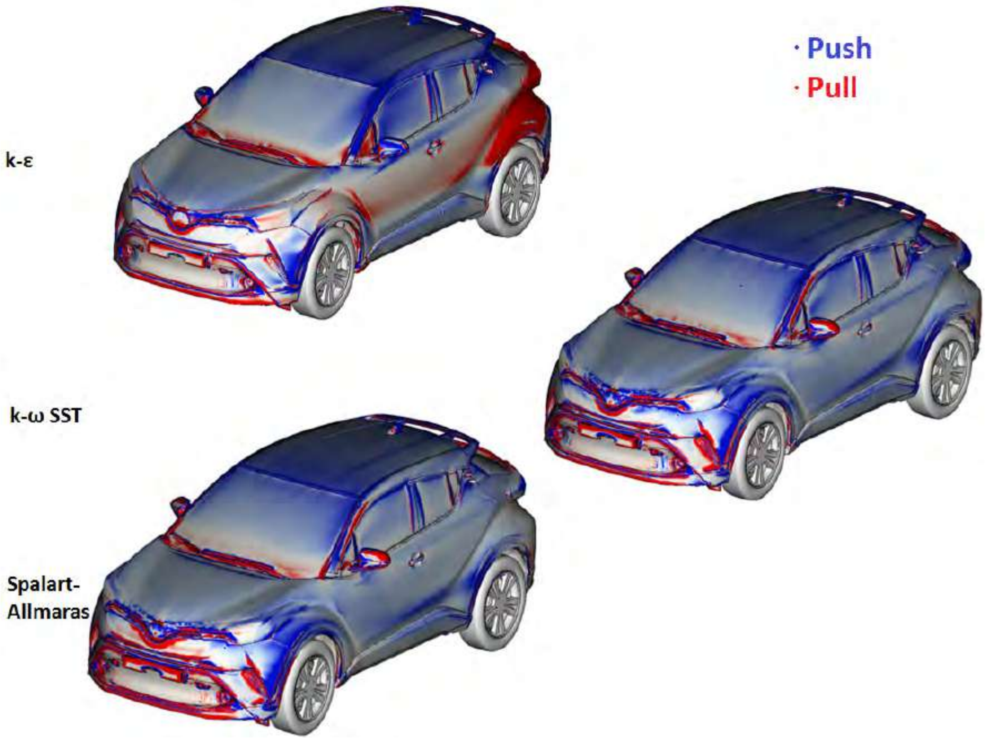

Figure 5.3: *Sensitivity map comparison of the three turbulence models - Front side view. Blue colored areas should be pushed inwards for drag reduction.*

Still the surface sensitivities in some areas with acute angles (such as minor portions on the headlights and the mirrors) have opposite sign. In general, though, they are in relative agreement.

5.1.2 Comparison of Sensitivity Maps from 1^{st} and 2^{nd} Order Discretization of the Primal Turbulence Equations

A robust and stable convergence of the primal and the adjoint problem can in many cases prove to be arduous to achieve without specific handling of certain terms. As it was described in chapter 2, one effective way to assist the adjoint system of equations to reach a stable convergence is to reduce the discretization order of the turbulence equations of the primal problem which is used as an input to it. This comes with some trade-off in accuracy. For this purpose, a comparison is carried out between the sensitivity maps obtained from a 2^{nd} versus a 1^{st} order discretization of the convection term for the k and ϵ PDEs during the solution of the primal problem. As it can be observed from a glance at figures 5.4(a) and 5.4(b), the general trend of the sensitivity derivatives is similar in the two cases.

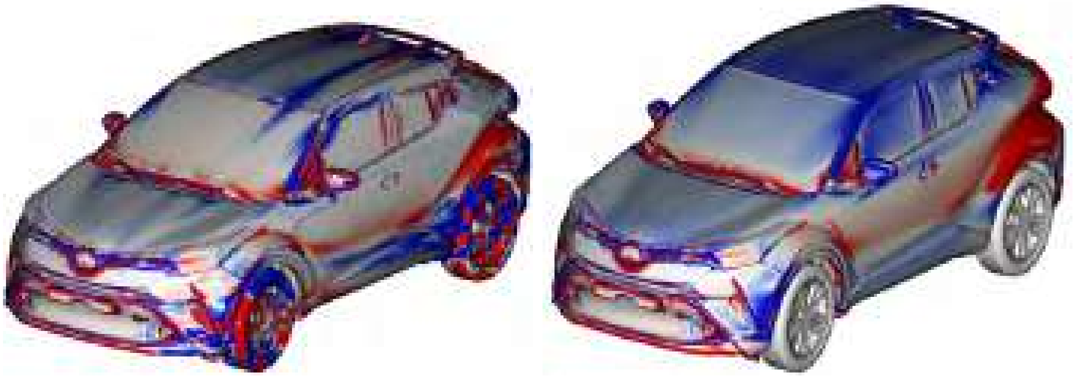

(a) (b)

Figure 5.4: *Sensitivity map side view, $k-\epsilon$ tubulence model. Left - 1^{st} order turbulent equations discretization. Right - 2^{nd} order turbulent equations discretization. Blue colored areas should be pushed inwards for drag reduction.*

Quantitative differences are present in most part of the vehicles surface but the sign generally remains the same. A few areas can be identified in figures 5.5(a) and 5.5(b) in which the color switches from one plot to another such as the mirrors and part of the roof, which are however limited.

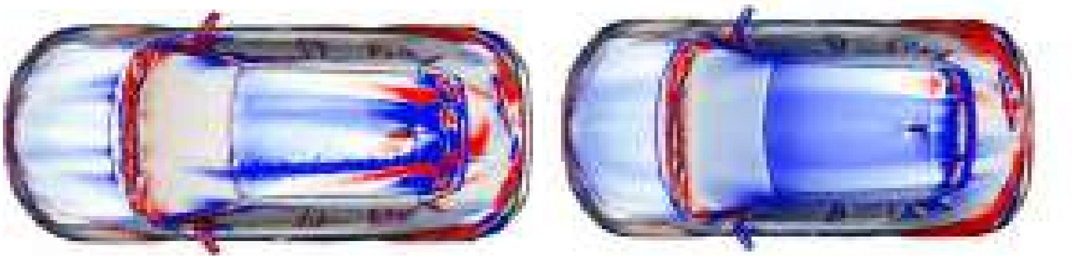

(a) (b)

Figure 5.5: *Sensitivity map top view, $k-\epsilon$ tubulence model. Left - 1^{st} order turbulent equations discretization. Right - 2^{nd} order turbulent equations discretization. Blue colored areas should be pushed inwards for drag reduction.*

In what can be seen in figures 5.6(a) and 5.6(b) on the rear of the car however, the picture is very different in the two cases. The sensitivity derivatives calculated from the two simulations bear few similarities on the back side of the car. Taking into consideration the fact that in both cases the adjoint problem was solved with identical discretization schemes, one can realize the significance of accurate computation of turbulence in such optimization problems. Neglecting the turbulent phenomena can lead to erroneous quantitative as well as qualitative computation of the sensitivities.

(a) (b)

Figure 5.6: *Sensitivity map back view, $k-\epsilon$ tubulence model. Left - 1^{st} order turbulent equations discretization. Right - 2^{nd} order turbulent equations discretization. Blue colored areas should be pushed inwards for drag reduction.*

A distinction between the two cases that is also very profound is the varying asymmetry of the two sensitivity maps. The 2^{nd} order map is generally rather symmetrical in the top but not in areas such as the sides of the front bumper and the rear part of the car. The sensitivity map from the 1^{st} order turbulence discretization on the other hand appears to be asymmetrical in a much larger part excluding the rear, in which, compared to the former, symmetry has increased. The fact that specific areas of the vehicle are symmetrical on one map and asymmetrical on the other, or even appear to have a totally different sensitivity distribution is mainly an indication of different prediction of the flow separation resulting from the wall shear stress computation during the primal solution. This difference could be caused by the reduction of the discretization order and, hence, the accuracy of the turbulence equations.

Particularly, in a vehicle with such a bluff shape as the one used in this study, the conclusion is that the turbulent phenomena play a key part in the flow evolution and need to be taken into account as accurately as possible. The accuracy of the turbulence equations can be vital for the correct prediction of the sensitivities. The differences between the 1^{st} and 2^{nd} order discretization of the turbulence equations are qualitative -i.e. the sensitivities have opposite sign- where turbulent phenomena govern the flow, such as the rear part.

5.2 Effect of the Primal and Adjoint Solution on the Symmetry of the Sensitivity Map

A remark that is quite evident is the fact the maps from the Spalart-Allmaras and the $k - \omega$ SST have a higher degree of symmetry compared to the one from $k - \epsilon$.

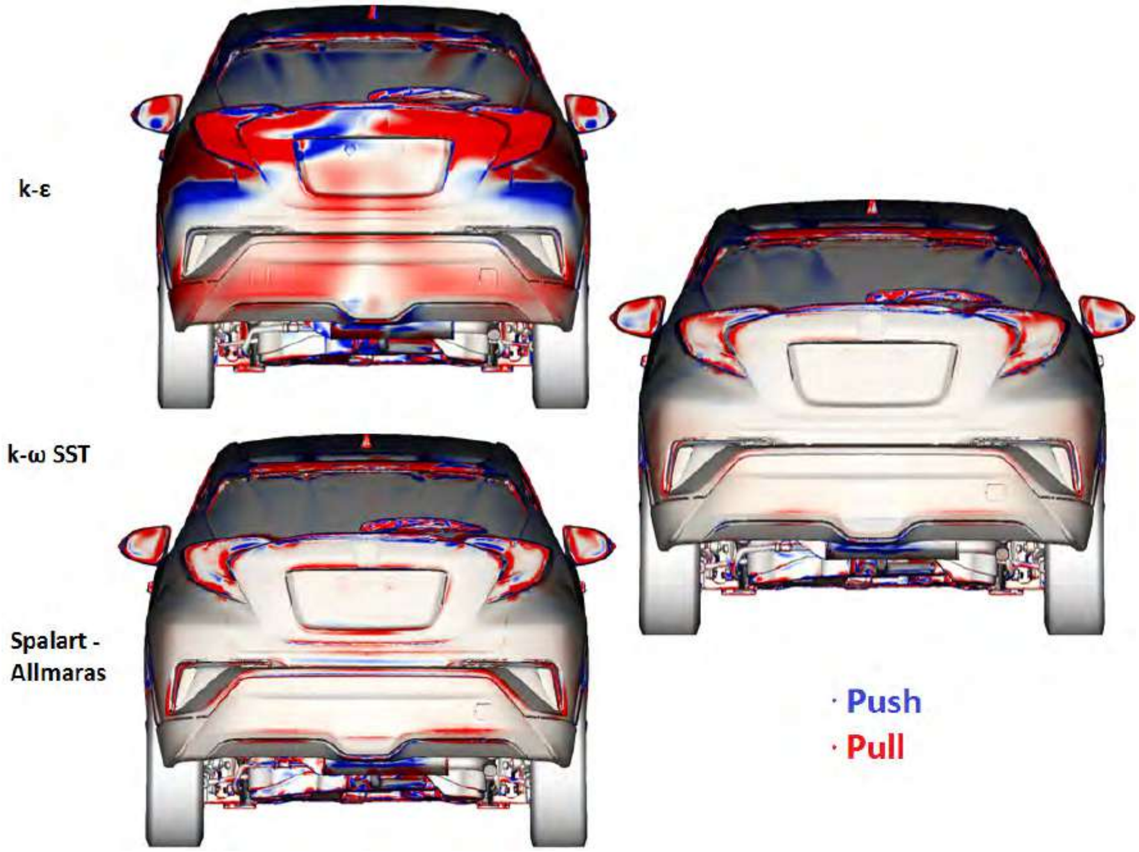

Figure 5.7: *Sensitivity map comparison of the three turbulence models - Rear view. Blue colored areas should be pushed inwards for drag reduction.*

This is an issue that needs to be taken into account and addressed when dealing with vehicle shape morphing. Any modification applied to the vehicles surface needs to be symmetrical about the YZ plane. The flow field obtained from the primal solution is however not entirely symmetrical, given the highly unsteady nature of the flow around the car and its geometrical features (detailed underbody, front and rear windscreen wipers) and as a result this asymmetry will be transferred to the sensitivity derivatives. As it was described in chapter 2, the adjoint problem is solved backwards in space and time, in this case in a direction from the wake towards the vehicle. As a result, the imbalance of the primal fields on the rear part of the vehicle -which is the “inlet” of the adjoint calculation- was passed on to the adjoint solution, and the adjoint fields ended up with an increased asymmetry compared to the primal ones, not only at the rear but at the entire surface of the body.

Since the velocity and static pressure computation from the $k-\epsilon$ model in the wake is much less symmetrical compared to the other two models, this asymmetry is much more profound on the sensitivity map from the $k-\epsilon$ model, as it can be noticed in figures 5.1 and 5.7.

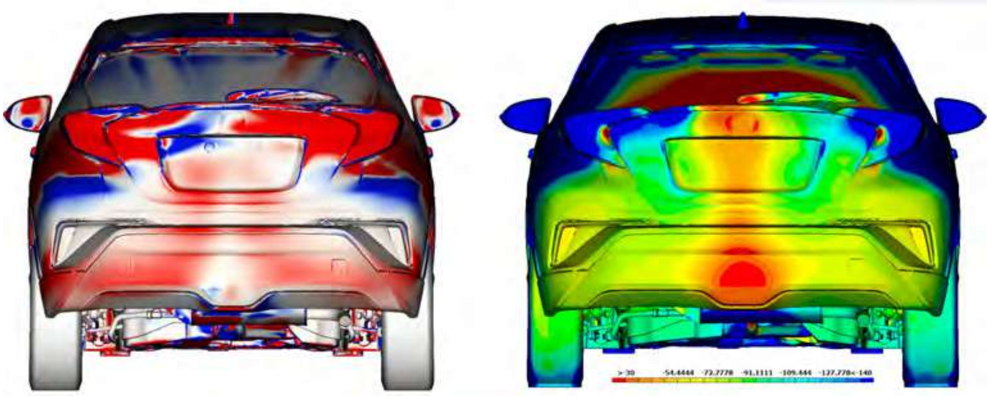

Figure 5.8: *Rear part of the car, $k-\epsilon$ tubulence model. Left: Sensitivity map, Right: Static pressure.*

As far as the $k-\omega$ SST model is concerned, the results appear to be very symmetrical in both the primal and the adjoint solution. This is demonstrated in figures 5.15, 5.16 and 5.17 where the primal and adjoint pressure distribution is compared.

Moreover, comparing the primal static pressure distribution between the $k-\epsilon$ model and the other two (fig. 4.4), the dissimilarities are mainly focused on the tail of the vehicle, particularly the area of the trunk and rear lights. For the rest of the surface, the variation of the primal fields between the models is not that intense (Figures 5.11, 5.14 and 5.17). Looking at the adjoint pressure of the three turbulence models on the other hand, the patterns are very different. The adjoint pressure distribution all over the body is significantly more dissimilar among the three, especially on the roof, the sides and the rear (figures 5.10, 5.13 and 5.16). This could indicate that a slight imbalance on the primal velocity and pressure is, in fact, amplified by the adjoint calculation.

- **k-**ϵ

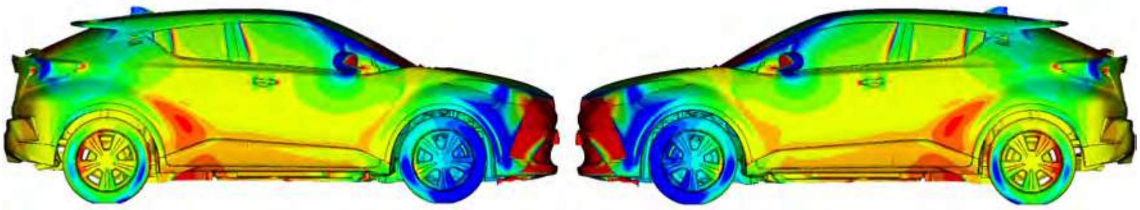

Figure 5.9: ***Static*** *pressure on the sides of the vehicle - $k-\epsilon$ turbulence model - Pressure Range [0,-300Pa].*

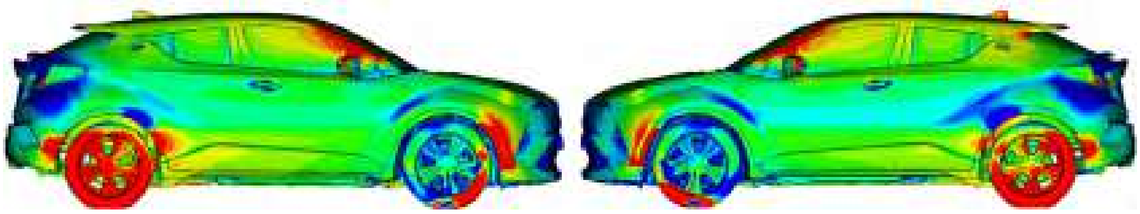

Figure 5.10: ***Adjoint*** *pressure on the sides of the vehicle -* $k - \epsilon$ *turbulence model.*

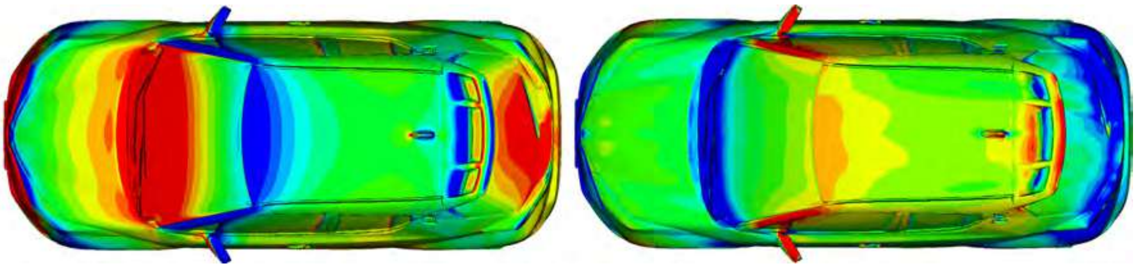

Figure 5.11: ***Static*** *(left) and* ***adjoint*** *(right) pressure on the top of the vehicle -* $k - \epsilon$ *turbulence model.*

- **Spalart-Allmaras**

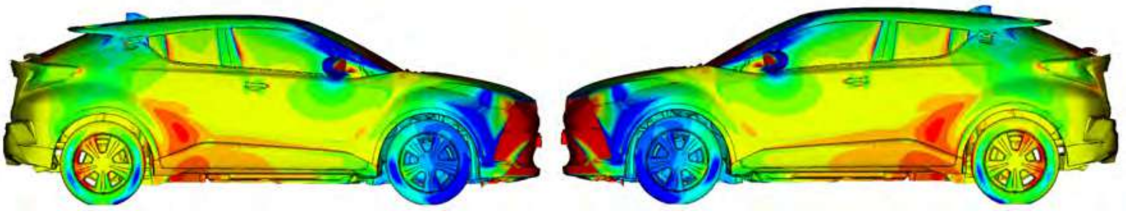

Figure 5.12: ***Static*** *pressure on the sides of the vehicle - Spalart-Allmaras turbulence model - Pressure Range [0,-300Pa].*

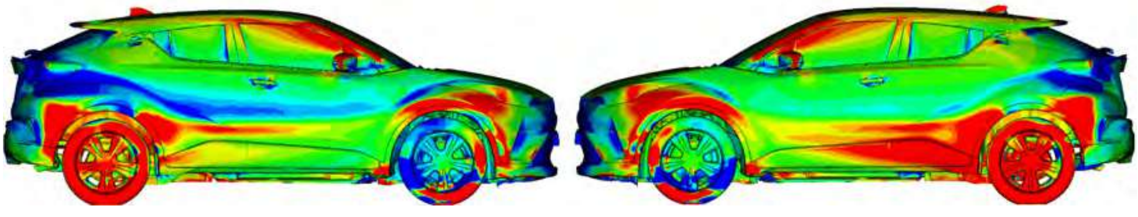

Figure 5.13: ***Adjoint*** *pressure on the sides of the vehicle - Spalart-Allmaras turbulence model.*

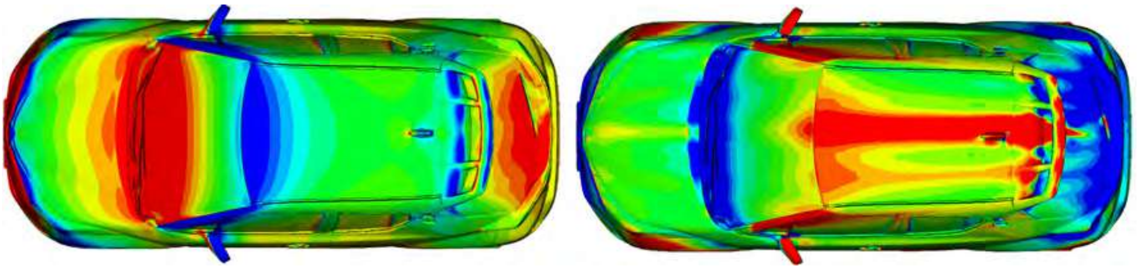

Figure 5.14: ***Static*** *(left) and* ***adjoint*** *(right) pressure on the top of the vehicle - Spalart-Allmaras turbulence model.*

- **k-ω SST**

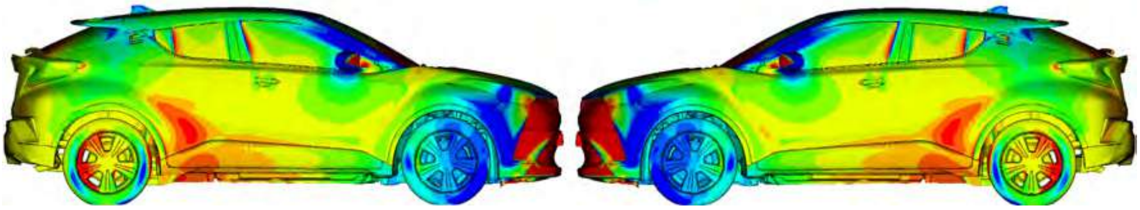

Figure 5.15: ***Static*** *pressure on the sides of the vehicle -* $k-\omega$ *turbulence model - Pressure Range [0,-300Pa].*

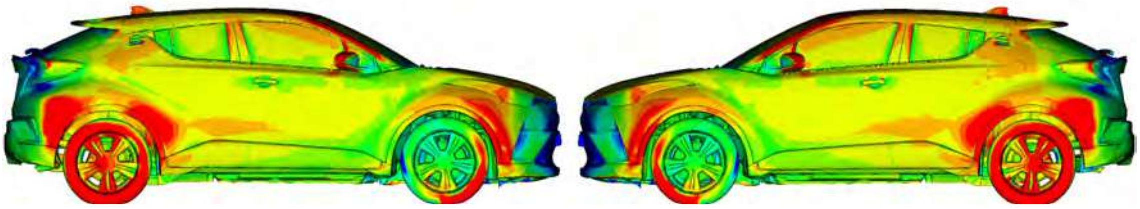

Figure 5.16: ***Adjoint*** *pressure on the sides of the vehicle -* $k-\omega$ *turbulence model.*

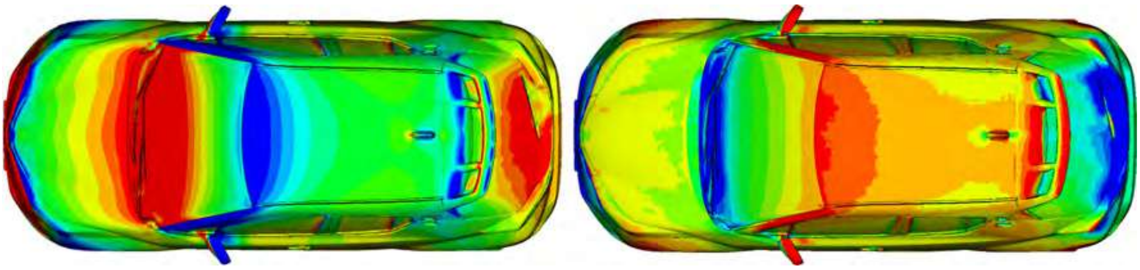

Figure 5.17: ***Static*** *(left) and* ***adjoint*** *(right) pressure on the top of the vehicle -* $k-\omega$ *turbulence model.*

It is clear that the $k-\omega$ SST and the Spalart-Allmaras models give -in general- much more symmetrical fields than the $k-\epsilon$ one. A reason for this can be that the two former models predict the separation of the flow at a much earlier part of the rear of the car than the $k-\epsilon$. This means that the flow is detached for the major part of the trunk where the flow is highly turbulent and eddies of all length-scales govern the flow. In case of attached flow at this area, this leads to highly alternating values of the shear stress at the wall along with intense fluctuation of the pressure field. This will cause vast asymmetries in the primal flow field and will, in turn, cause equally intense variation and asymmetry in the calculated sensitivity derivatives of the drag force w.r.t. the surface-normal displacement of the nodes at this area, as is the case in the $k-\epsilon$ turbulence model.

5.3 Averaging of the Solution

A software that performs automatic shape morphing based on the sensitivity derivatives of the objective function with respect to the symmetrical displacement of the control points of the morphing box has been developed by the PCOpt/NTUA. This tool was remarkably convenient for the morphing applied in this thesis.
Nevertheless, the attempt to further improve the symmetry of the results was made in all cases, initially by averaging the solution. The averaging was performed using the following formulation, whereby U stands for any arbitrary flow quantity,

$$U'_{Mean} = \frac{t_i - 1}{t_i} U_{Mean} + \frac{1}{t_i} U \tag{5.1}$$

where:

U'_{Mean} → Mean field calculated at current iteration
U_{Mean} → Mean field calculated at the previous iteration
t_i → Current iteration number
U → Instantaneous field calculated at current iteration

The averaging was initiated after the solution had reached a steady oscillation around a mean value both for the primal and the adjoint calculation, a fact that was ensured by monitoring the convergence of the drag coefficient and the primal and adjoint velocity and pressure at specific points of the domain. For example, in the case of the Spalart-Allmaras model, averaging of the pressure and velocity fields started at iteration 10000 and was performed until the end of the iterative solution. The convergence of the drag coefficient can be seen in figure 5.18.

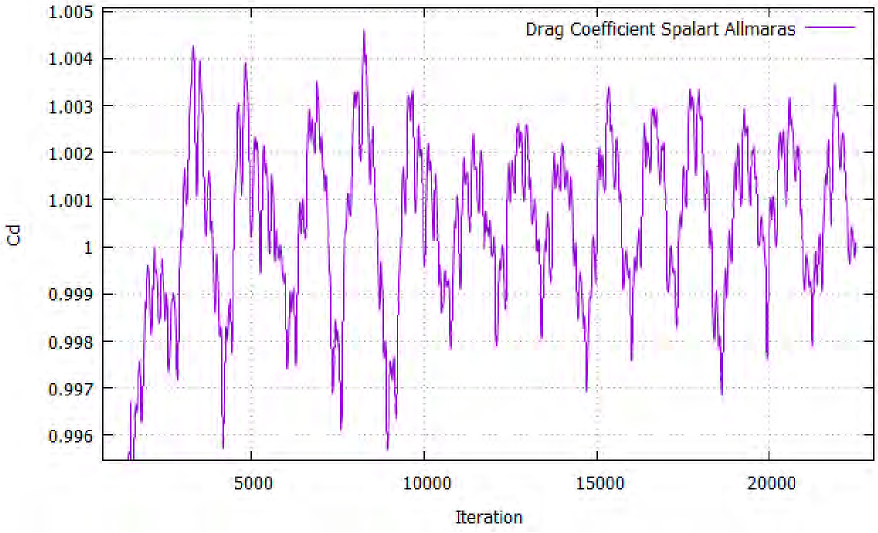

Figure 5.18: *Convergence of the Drag Coefficient - Spalart-Allmaras turbulence model.*

On all three cases averaging was done for a significant number of iterations to ensure maximum smoothness of the resulting fields. The effect of this to the solution is demonstrated in figures 5.19(a) and 5.19(b) of the pressure at the rear part of the car. The rear is a very important area of the vehicle and accurate prediction of the static pressure there is integral for the validity of the calculated drag coefficient. Most major differences between the three turbulence models occurred there, as did the resulting sensitivity maps.

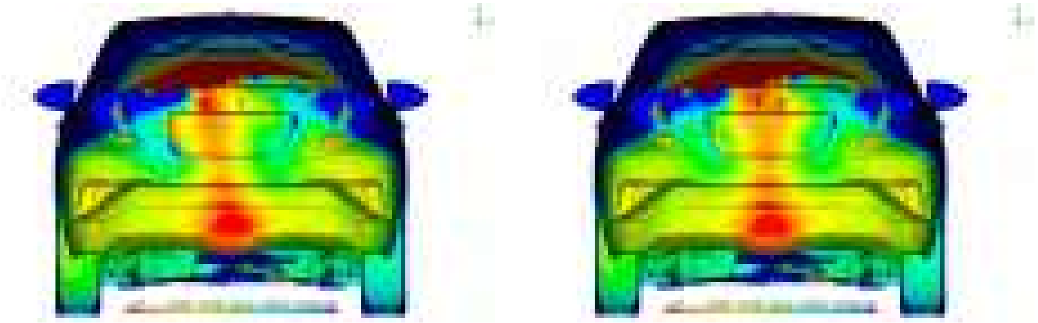

(a) Without averaging

(b) With averaging

Figure 5.19: *Static pressure on the back side of the vehicle - $k-\epsilon$ tubulence model.*

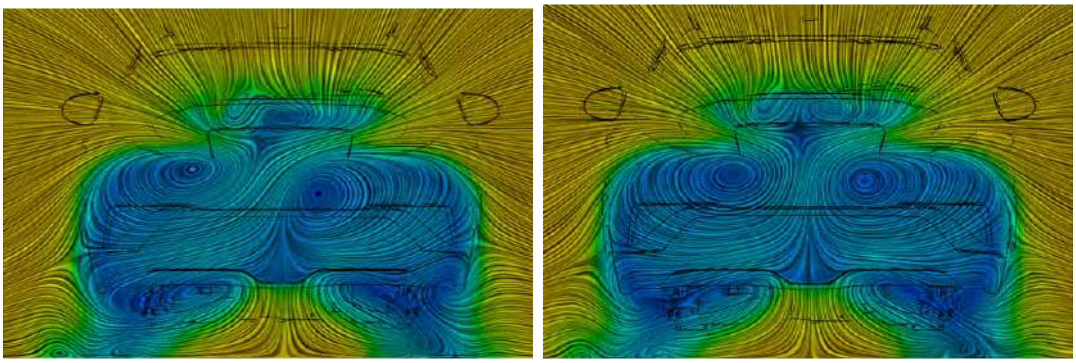

(a) Without averaging (b) With averaging

Figure 5.20: *Transversal LIC velocity stream 2.5m behind the rear bumper -* $k-\epsilon$ *turbulence model.*

The pressure distribution shown in figures 5.19 and 5.20 is within a 110 Pa range which is equivalent to a 2.5% of the total pressure range on the surface of the vehicle. This means that the asymmetry is strongly magnified and, given the natural asymmetry of the car due to its underbody and front and rear windscreen wipers, may be neglected. It does, however, lead to strong asymmetries on the resulting sensitivity map and is ideally eliminated. Furthermore, since a similar fluctuation is observed on the convergence of the adjoint problem, this led to the implementation of a similar process on the adjoint solution, i.e. averaging of the adjoint fields, which also helped achieve a more symmetrical sensitivity map, as it is demonstrated below on figures a 5.21 and 5.22.

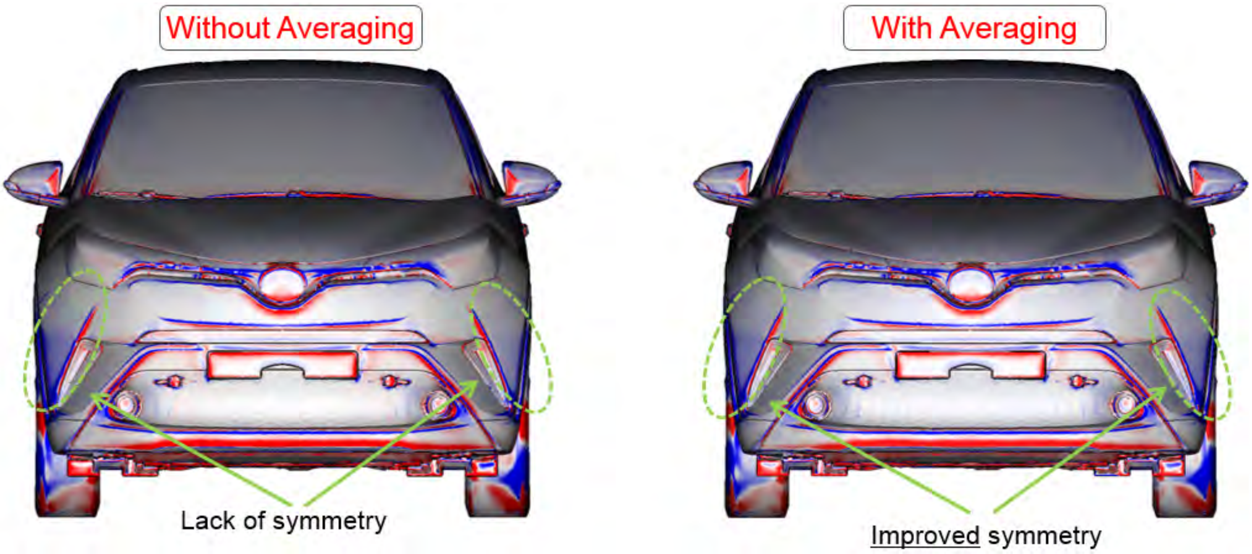

Figure 5.21: *Effect of averaging on the sensitivity derivatives,* $k-\epsilon$ *tubulence model. Front view.*

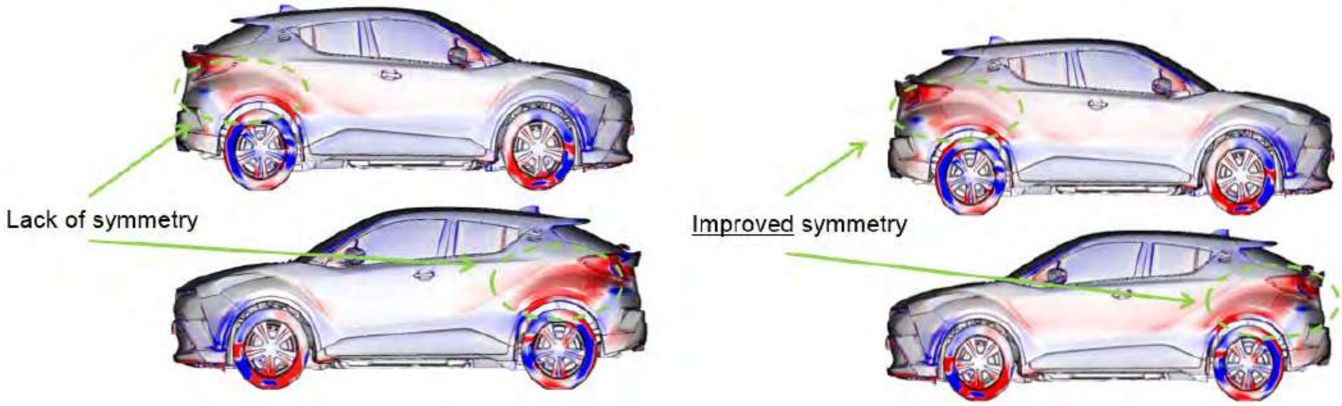

Figure 5.22: *Effect of averaging on the sensitivity derivatives, $k-\epsilon$ tubulence model. Side view.*

whereby the sensitivity map obtained from the $k-\epsilon$ turbulence model is presented with and without averaging of the adjoint fields. The asymmetries on the front bumper, between the left and right side, have been significantly reduced, as has the area on the sides of the rear part. In general the rear area of the vehicle remains asymmetrical, but this is mainly due to the equally imbalanced flow field that was "inherited" from the primal solution [1], and cannot be balanced out by a simple averaging of the solution. It should be mentioned here that averaging does not only serve as a means to increase the symmetry of the results, but also to filter the natural unsteadiness of the flow. Especially around a bluff body, such as that of the car used in this thesis, the flow field between consecutive time steps of simulation varies a lot. Averaging contributes in this case to smooth the final picture of the flow. Finally, in order to obtain an 100% symmetrical sensitivity map, a half car model was used and the simulations were rerun. The windscreen wipers were removed from the front and rear windscreen as previously mentioned, and the detailed underbody was maintained as before.

Apart from obtaining a flow solution that better depicts the average flow around the car and increasing the degree of symmetry of the computed fields, averaging of the primal velocity and pressure fields was also an important parameter in assisting the stability in the convergence of the adjoint solution. It is important to note that, as described in chapter 2 (2.2.1), the flow and adjoint problems share the same eigenvalues. The non-linear nature of the flow problem means that the eigenvalues of its left hand side matrix are recalculated during each iteration of the primal solver loop. The adjoint system on the other hand is linear and its eigenvalues are constant throughout the solution and depend on the solution of the primal problem

---

[1] Regardless of the measures that were used to increase the symmetry of the flow fields, a slight imbalance was always present.

provided to it. In a highly oscillating problem such as the one under question, the possibility of the appearance of an eigenvalue greater than one in the primal system of equations is high. Averaging the solution of the flow problem over a significant number of iterations and using this as an input to the adjoint instead of just using the solution obtained during the last iteration of the primal solver loop decreases the possibility of the existence of an eigenvalue greater than unity in the left hand side matrix of the discretized adjoint system of equations, thus helping the adjoint system avoid divergence.

Chapter 6

CFD-based Morphing and Optimization of the Geometry

In order to morph the geometry of the car and, finally, to minimize the drag coefficient the automated morphing tool developed and integrated within the adjoint software by the PCOpt/NTUA was used. The algorithm requires the setup of an initial control box which will include the to-be-morphed part of the CFD mesh. From that point, on it runs as many optimization cycles as it has been set to. One optimization cycle consists of the solution of the flow problem, the adjoint problem and a mesh deformation.

6.1 Introduction

When it comes to external aerodynamic optimization of vehicles where the limitations and restrictions of the allowed geometry deformation are very high, the proper and precise setup of a few important parameters of the morphing box are crucial. The setup of the box requires a number of parameters which are listed below:

- Number of control points at each direction of the control box
- Degree of the B-Splines Basis Functions
- Optional confinement of the displacement of control points located at the boundary of the control box in all directions or in specific user-defined directions

The last parameter comes in handy in many occasions as it allows the option of freezing specific layers of control points towards any arbitrary direction or even towards the positive or negative of a specific axis in order to maximize the freedom of morphing the geometry. This is a useful feature of the control box, both in external and internal aerodynamics, since it allows achievement of the maximum possible optimization margin while respecting specific important parameters. These can be, for instance, that the outer boundaries of a given duct do not exceed the dimensions of the fixed boundaries enclosing it, or to make sure that specific boundaries of the car's surface will not be pushed inwards when packaging constraints disallow it. What is more, when dealing with a half-car geometry, points located on the symmetry plane are of course required not to move about the Y axis for the sake of continuity of the CFD mesh and the vehicle's smoothness at this area.

Another important aspect when using volumetric B-Splines to parameterize and morph the geometry is the number of control points used. By increasing the number of control points allowed to move in each direction (i.e. the number of design variables), the optimization margin grows, alongside of which the freedom of local deformation of the geometry scales. The latter can result in "bumps" appearing on the morphed geometry which are, of course, not acceptable. A careful selection of the control points needs to be, therefore, made in order to achieve the optimal balance between acceptable geometry and maximal gain at each cycle.

In the extent of this thesis a number of optimization runs were carried out -mainly focusing on the front bumper-some of which will be presented here. In what follows, the term "single-step optimization" indicates the optimization runs during which a single shape change was performed, followed by an evaluation of the optimized geometry. The Spalart-Allmaras turbulence model was used for all the optimization runs that were carried out in this thesis, in its High-Re variation together with wall functions.

6.2 Single-Step Optimization

In order to identify the suitable positioning and setup of the control boxes for the optimization loops, several single-step optimization cases were run in numerous targeted areas of the vehicle although, finally, due to time limitations the optimization runs were focused only on the front bumper.

Initially, a number of shape morphing runs were carried out without any evaluation of the resulting geometry in order to visually inspect the new geometry and decide on the most suitable location and set-up of the morphing box for each area. As a second step, the optimized geometries that were selected (based on design criteria) were evaluated with one flow solution and the flow fields and drag coefficient were obtained. These single-step optimization runs were performed on the rear bumper, the rear spoiler, the second spoiler located between the tail lights and of course the front bumper of the car.

6.2.1 Front Bumper

The front bumper of the vehicle was the main focus of the optimization process carried out during this diploma thesis. Because of this, a number of one-step optimization test cases were run using different settings and positioning of the control box, in order to identify the appropriate setup as well as the optimal step for the steepest descent η coefficient [1], which in turn sets the maximum node displacement of the control grid points. One of these cases will be presented here. The resulting geometry can be seen below, in figure 6.1.

Figure 6.1: *Baseline vs Optimized Front Bumper. Optimized geometry on the left side of the figure.*

The result was a 1% C_D reduction, after one shape change, as it can be seen below in figure 6.2.

---

[1] The steepest descent algorithm multiplies the derivative of the objective function with a coefficient η that sets the magnitude of the step of the optimization, as follows. $b_{new} = b_{old} - \eta \frac{\delta F}{\delta b_n}$ whereby b_{new} is the design variable computed during the current step, b_{old} the design variable computed during the previous step and $\frac{\delta F}{\delta b_n}$ the derivative of the objective function w.r.t. the respective design variable b_n. The selection of η shall be done with caution as it may lead to an overshoot of the optimal solution [21].

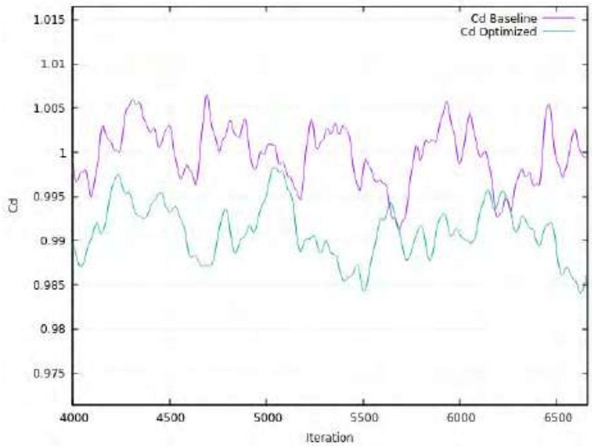

Figure 6.2: *Baseline vs Optimized Front Bumper - Drag Coefficient. Spalart-Allmaras turbulence model.*

The control box consisted of 5x5x5 control points in the X, Y and Z coordinates. [2]. The maximum displacement of the control grid nodes was limited to 2.5cm. In figures 6.3(a) and 6.3(b), the magnitude of the displacement of each CFD mesh point can be seen plotted on the surface of the vehicle, so as to identify the areas that were morphed more intensely (the areas deformed most are colored in red, and those that remained still are colored in blue).

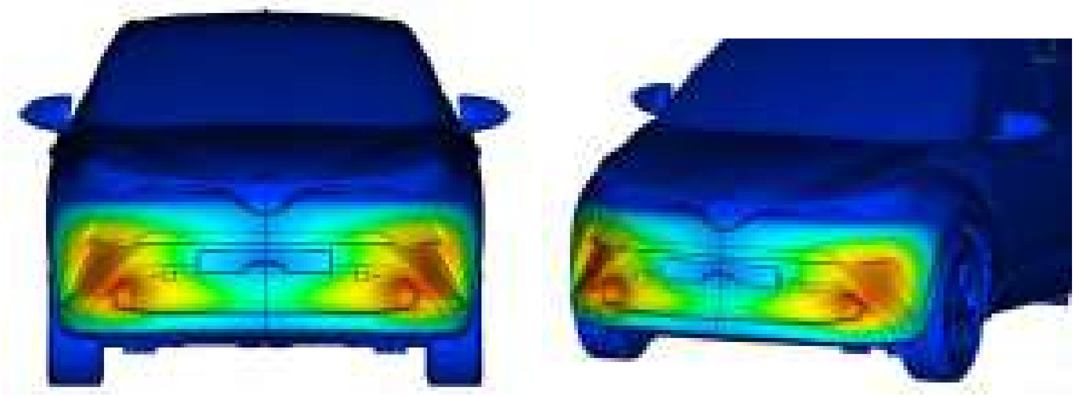

(a) (b)

Figure 6.3: *Magnitude of the displacement of the surface CFD mesh nodes. Spalart-Allmaras turbulence model. Left - Front view. Right - Side front view.*

The resulting shape was very smooth and the difference from the baseline model is hardly identifiable. Yet, 1% reduction of the C_D was achieved.

---

[2] The control boxes in all cases were aligned with the X, Y and Z Cartesian coordinates.

6.2.2 Main Spoiler

The main spoiler of the vehicle located at the rear end of the roof serves multiple purposes including reduction of the drag coefficient, reduction of the rear axle lift coefficient and elimination of the dirt and debris that fall on the rear part of the vehicle. Optimal design and positioning of the spoiler is crucial in order for the two former purposes to be successfully fulfilled. In this case, the sensitivity map of all turbulence models provided concrete and consistent measures for the optimization of the spoiler which was carried out via the automated morphing tool of PCOpt/NTUA through a one-step optimization cycle.
The general direction of the maps was to push the spoiler towards the ground and extend it towards the rear. Minor differences were of course present in the maps, but the general direction was similar as it can be seen in figure 6.4, and the prediction was correct, as it will be demonstrated below.

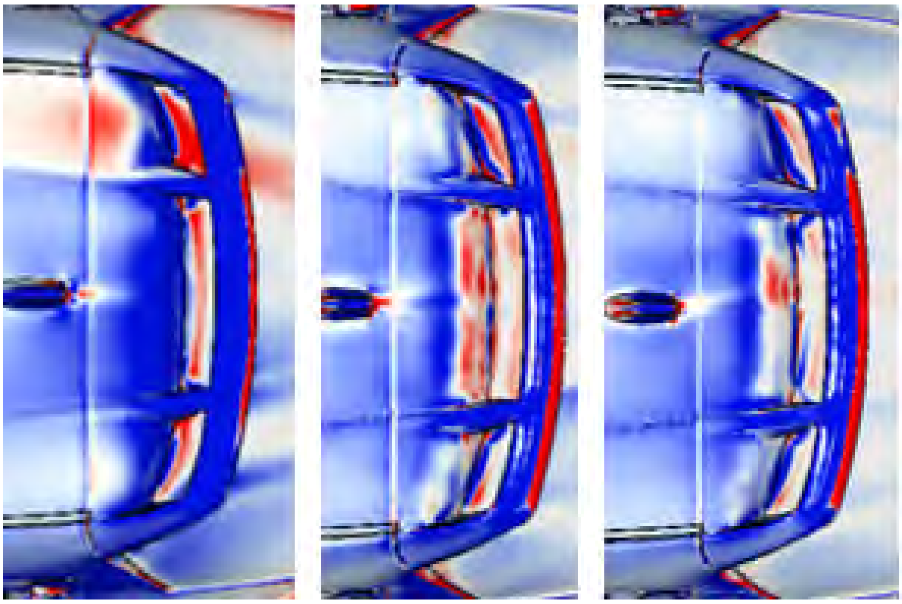

Figure 6.4: *Sensitivity maps of the spoiler from the three turbulence models. From left to right :* $k-\epsilon$, $k-\omega$ *SST, Spalart-Allmaras.*

In figure 6.5, the morphed geometry is shown, which resulted in a 0.5% C_D improvement.

Figure 6.5: *Baseline vs Optimized geometry. Optimized geometry on the right.*

A picture of the magnitude of the displacement that was applied to each point of the bumper plotted on the surface is shown in figure 6.6.

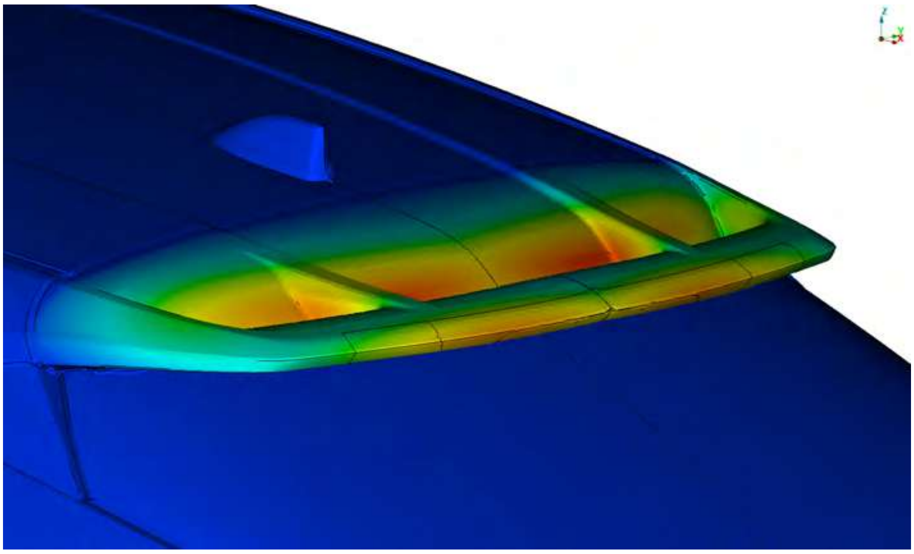

Figure 6.6: *Magnitude of the displacement of the surface CFD mesh nodes - Side view.*

6.2.3 Secondary Spoiler

As mentioned in chapter 3, section 4.1.2, the shape of the car's rear-end forces the flow coming from the roof through the spoiler and the flow from the sides to separate at the end of the rear windscreen after the second spoiler that connects the two taillights shown in figures 6.7(a) 6.7(b).

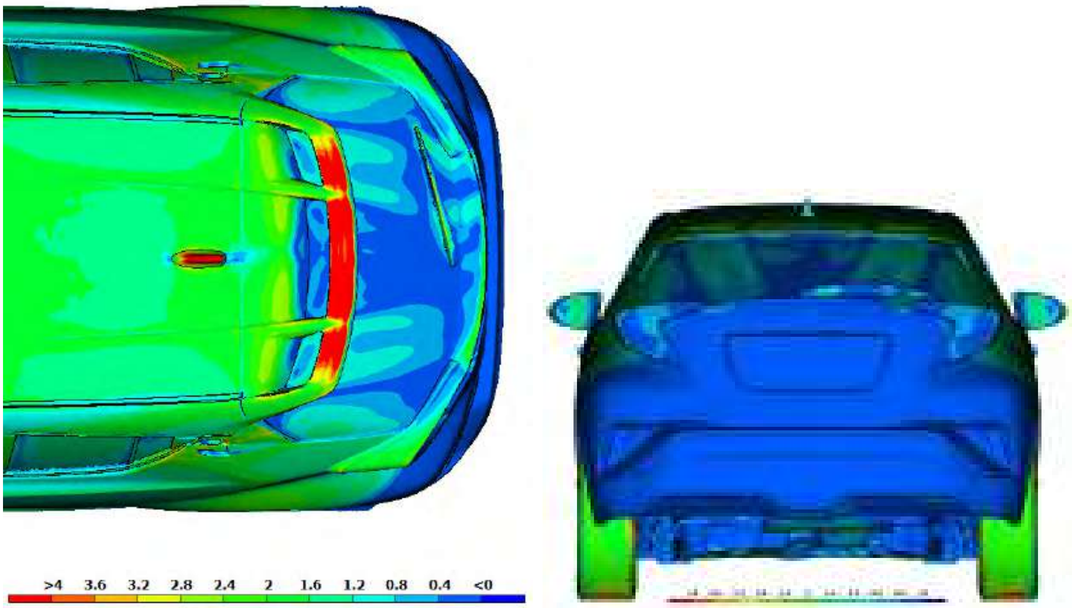

(a) (b)

Figure 6.7: *Shear stress on the surface of the baseline model. Spalart-Allmaras turbulence model. Flow is reattaching after the roof due to the hollow spoiler and separating again at the end of the second spoiler. Left - Top view. Right - Rear view.*

This immediately renders that "second spoiler" to become extremely sensitive to drag reduction and its shape is naturally crucial to the wake formation, shape and volume as it was demonstrated by the sensitivity maps of all turbulence models. An example of the sensitivity map can be seen in figure 6.8.

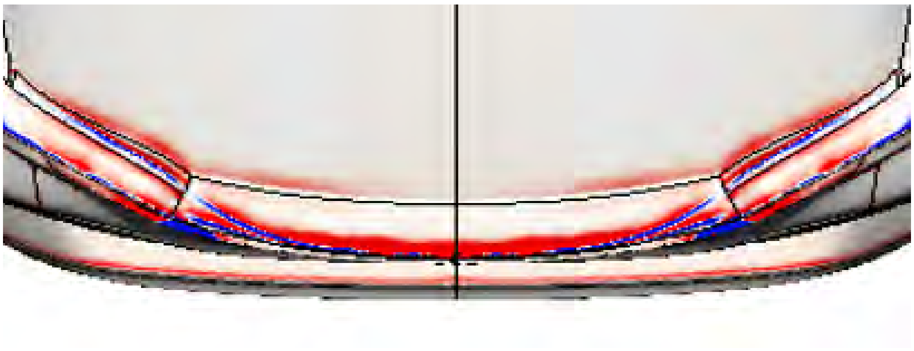

Figure 6.8: *Sensitivity map on the second spoiler.*

The map suggests extending the spoiler towards the rear and lifting it upwards.

The drag force sensitivity derivatives at this area are intense and it was therefore a canditate area for shape morphing. The result was a 0.5% C_D reduction and the final shape can be seen in figures 6.9(a) and 6.9(b).

(a) Baseline vs Optimized geometry. Optimized geometry on the right side of the figure. (b) Baseline vs Optimized geometry. Optimized geometry on the right side of the figure.

Figure 6.9

The magnitude of the displacement that was applied to each point of the bumper plotted on the surface is shown in figure 6.10.

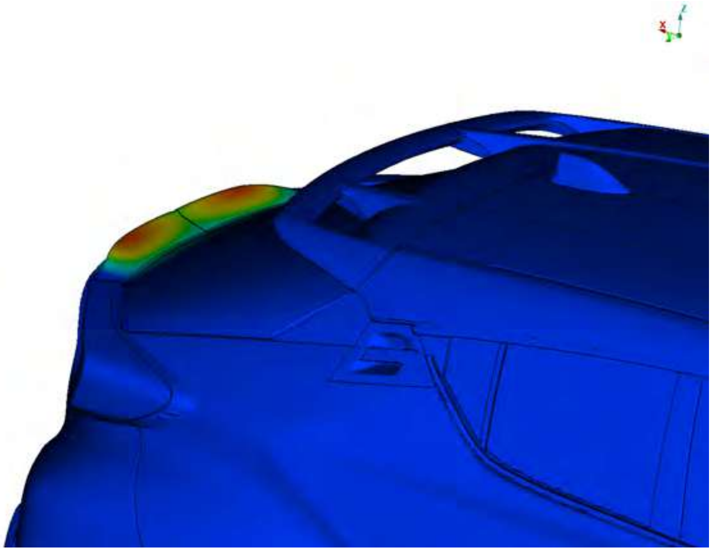

Figure 6.10: *Magnitude of the displacement of the surface CFD mesh nodes - Side view.*

6.2.4 Rear Bumper

A similar approach was followed for the rear bumper of the vehicle, which resulted in a 1% C_D reduction.

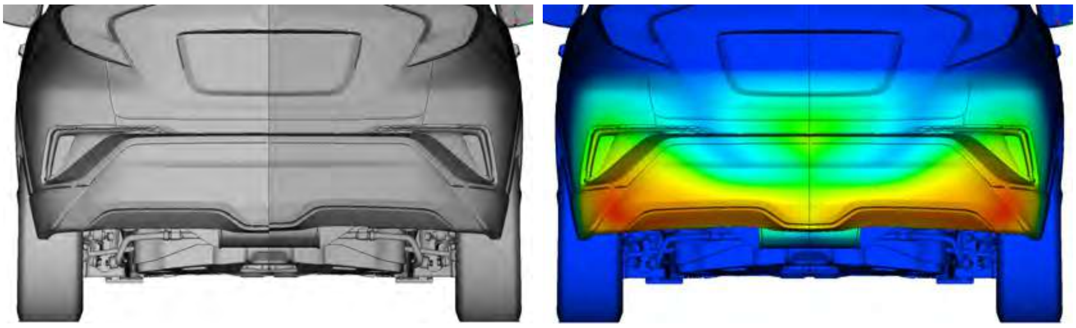

(a) Baseline vs Optimized rear bumper. Optimized geometry on the right side of the figure.

(b) Magnitude of the displacement of the surface CFD mesh nodes - Rear view.

Figure 6.11: *Optimization of the rear bumper. Left - Baseline vs. optimized geometry. Right - Magnitude of the displacement of the surface CFD mesh nodes.*

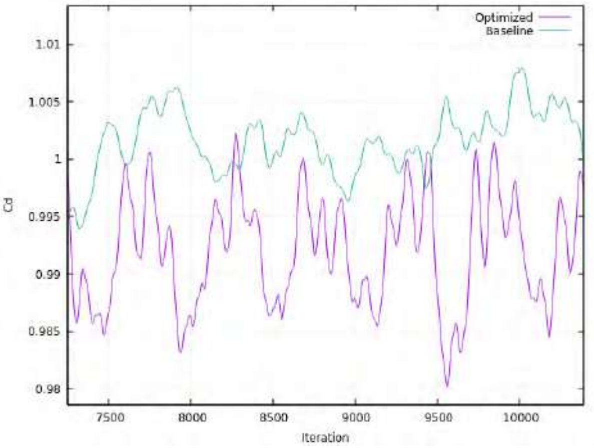

Figure 6.12: *Baseline vs Optimized Front Bumper - Drag Coefficient.*

The lower part of the bumper was lifted upwards, and the common ”Boat Tailing” drag reduction technique was applied by the automatic morphing tool.

6.3 Front Bumper Optimization – Run A

During the first optimization run, two control boxes where used to parameterize the space around the front bumper. The resulting grid of the control points can be seen in figures 6.13(a), 6.13(b), 6.13(c), 6.13(d)

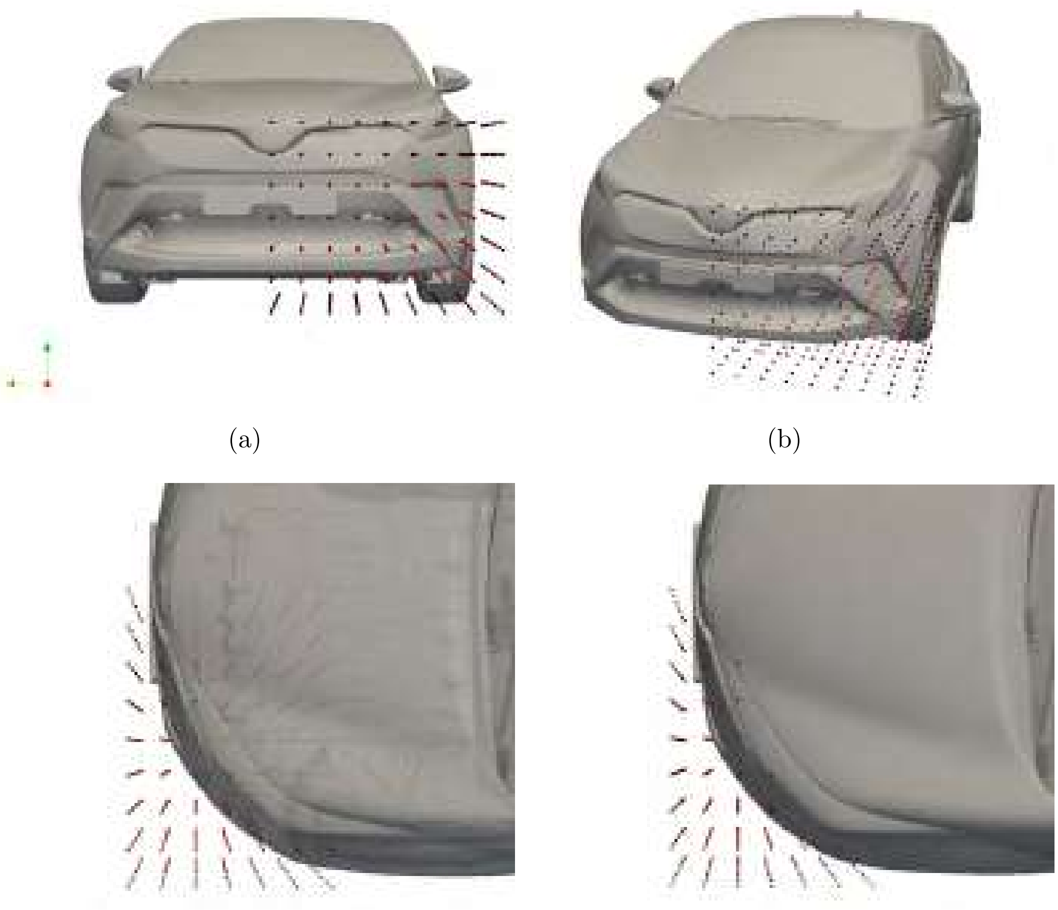

(a) (b)

(c) (d)

Figure 6.13: *Optimization run A. Volumetric B-Splines control grids. The control points are not connected with lines for better visual inspection of the enclosed space.*

whereby only the red control points are allowed to move. The rest (one outer layer) of the control points are frozen to ensure non-corruption of the CFD mesh at the boundary of parameterized and not parameterized points. In addition, one extra layer of control points was frozen at the maximum Z direction (top of the box) in order to conform with surface restrictions for the car's body on the symmetry plane, the headlights and the wheels, which should not be deformed. The control grid comprises of 7x9x7 control points in total in the X, Y and Z directions respectively. The basis functions' degrees were P_u=P_v=P_w=3. Two optimization cycles were run with 2^{nd} order discretization schemes for all the PDE's of the flow and adjoint problems. The total drag coefficient reduction was approximately 2%, as can be seen in figure 6.14.

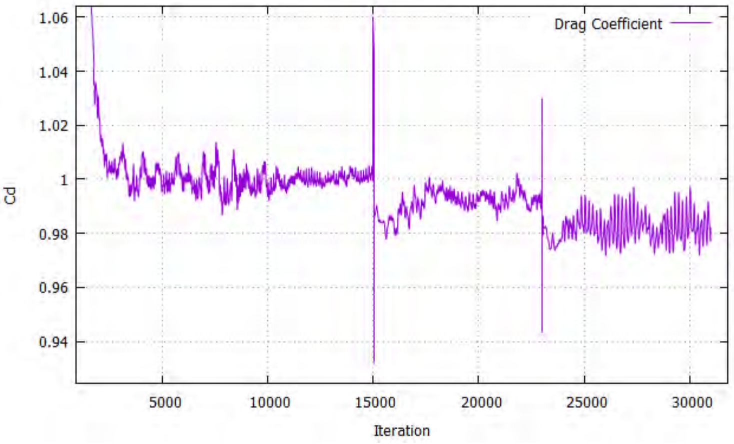

Figure 6.14: *Drag coefficient reduction over the optimization loops. The points of discontinuity in the graph indicate the iteration during which shape morphing was performed. Spalart-Allmaras turbulence model.*

The convergence of the primal and adjoint equations is shown in figures 6.15(a) and 6.15(b).

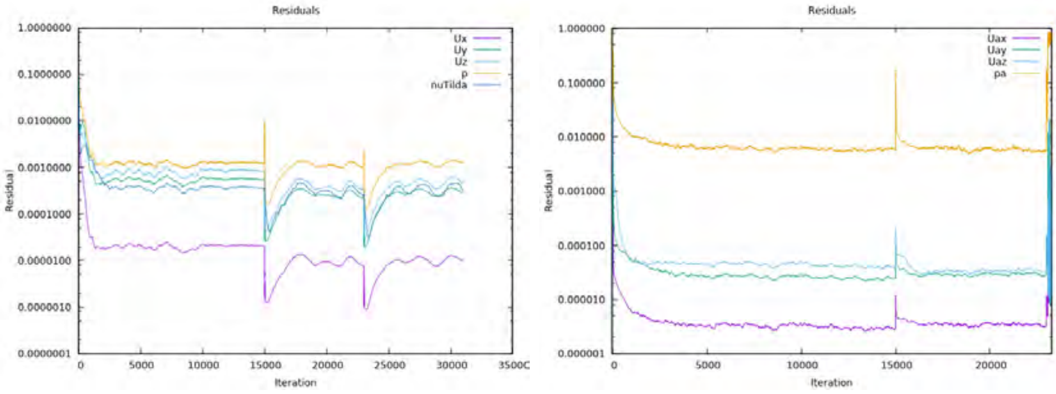

(a) (b)

Figure 6.15: *Residuals of the flow and adjoint equations during the optimization run A. Spalart-Allmaras turbulence model. Left - Primal. Right - Adjoint.*

The final shape was relatively smooth without any discontinuities and bumps and the maximum displacement of the CFD mesh nodes was approximately 2cm throughout the optimization procedure. The comparison of the baseline and optimized geometry can be seen in figure 6.16, whereby the optimized geometry is colored in dark grey. Two significant modifications can be identified in the optimized geometry, compared to the baseline, which can directly be linked to the flow evolution from the front bumper towards the rest of the vehicle. Firstly, the lower part of the bumper (skirt) was pushed downwards, in order to constrict and reduce the mass flow of air that is forced towards the underbody of the vehicle, thus reducing the drag. Secondly, the sides of the bumper if front of the wheels were pulled outwards in the Y direction, a modification which has a twofold impact on the drag force reduction.

1. The flow is driven away from the wheels and energy loss in the area in the proximity of the wheels is reduced and
2. flow separation from the sides of the bumper is reduced.

Figure 6.16: *Optimized vs Baseline geometry - Front view - Optimized geometry on the right side of the figure.*

In figures 6.17(a) and 6.17(b), the surface of the car is colored according to the magnitude of the displacement that was applied to it during the last optimization cycle.

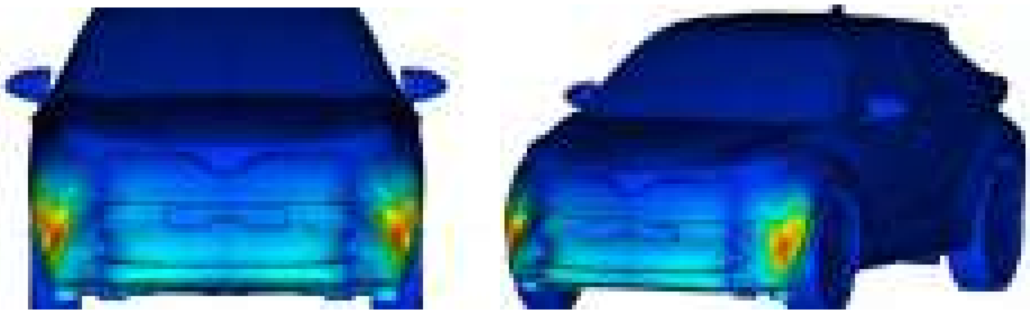

(a) (b)

Figure 6.17: *Magnitude of the displacement of the surface CFD mesh nodes. Left - Front view. Right - Side front view.*

Mesh quality checks are automatically performed after each deformation, as it was already implemented on the fully automated optimization algorithm of PCOpt/NTUA and was used for all the automated optimization cycles.

6.4 Front Bumper Optimization – Run B

In the second optimization run, a single box which wrapped the entire target space was used. The box consists of 7x7x8 control points and again the basis function were of degree p=3 in all directions. The control box can be seen in figures 6.18(a), 6.18(b), 6.18(c) and 6.18(d), where the red points are the ones that are allowed to move.

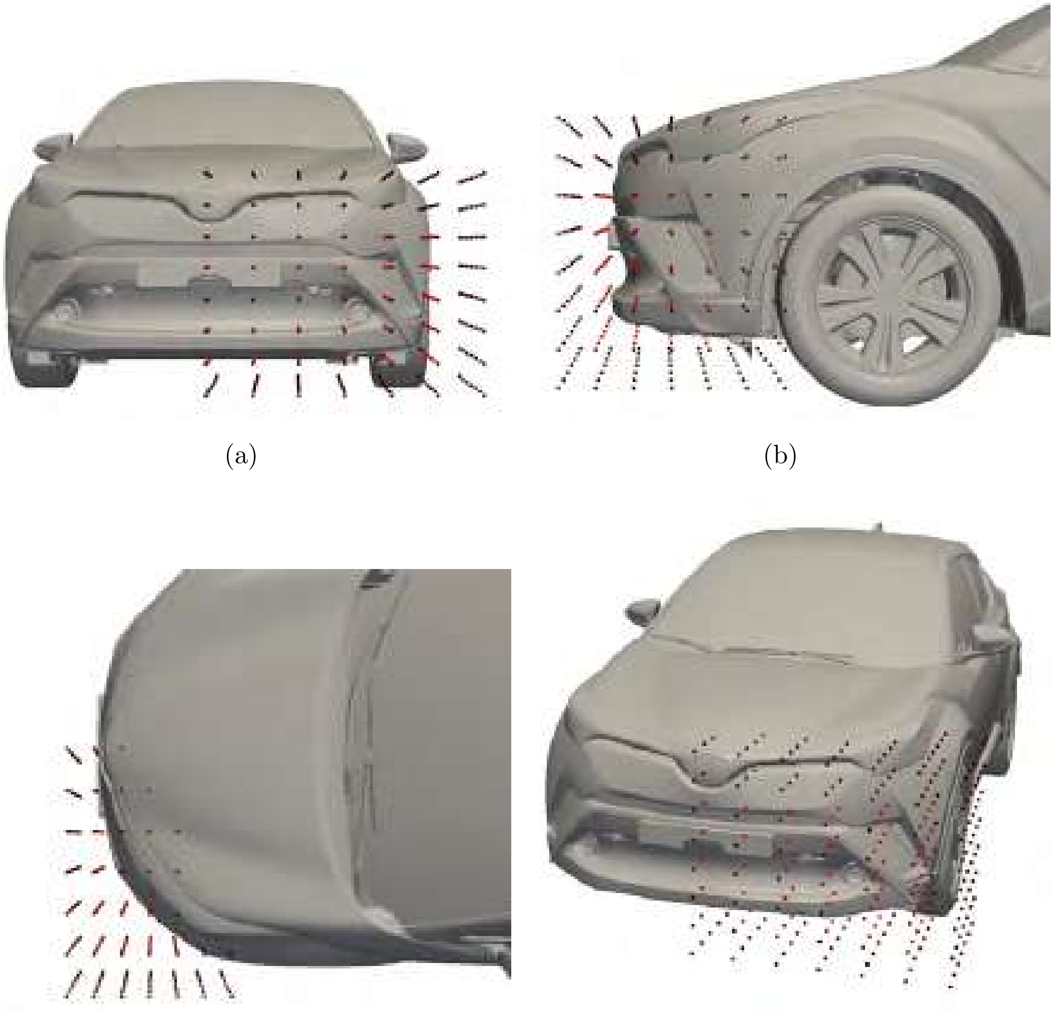

(a) (b)

(c) (d)

Figure 6.18: *Optimization run B. Volumetric B-Splines control grid.*

Two layers of control points at the maximum X direction of the box and two at the maximum Z direction were kept frozen, still for the accommodation of geometry constraints. Furthermore, the final layer of control points on the minimum X, Y and Z direction were movement–free for mesh continuity and quality purposes. In total, three optimization cycles were performed and the optimization history of the drag coefficient as well as the residuals of the equations can be seen in figures 6.19, 6.20(a) and 6.20(b).

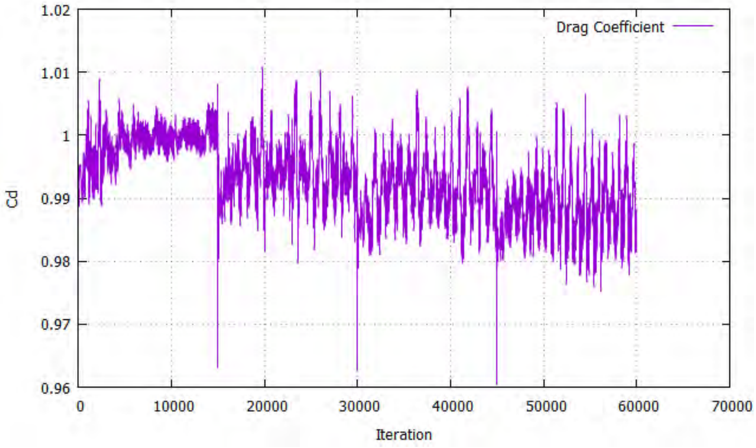

Figure 6.19: *Drag coefficient reduction over the optimization loops. Spalart-Allmaras turbulence model.*

whereby the total C_D reduction was 1.2%. In this case, it is clear from the oscillation of the drag that the solution was much more unstable than run A, which is mainly due to the way the CFD mesh was deformed. The shape of the last cycle of this optimization run was however much smoother and compliant with the design criteria as it can be seen in figures 6.21(a), 6.21(b), 6.21(c) and 6.21(d). Convergence for this case can be observed in figures 6.20(a) and 6.20(b).

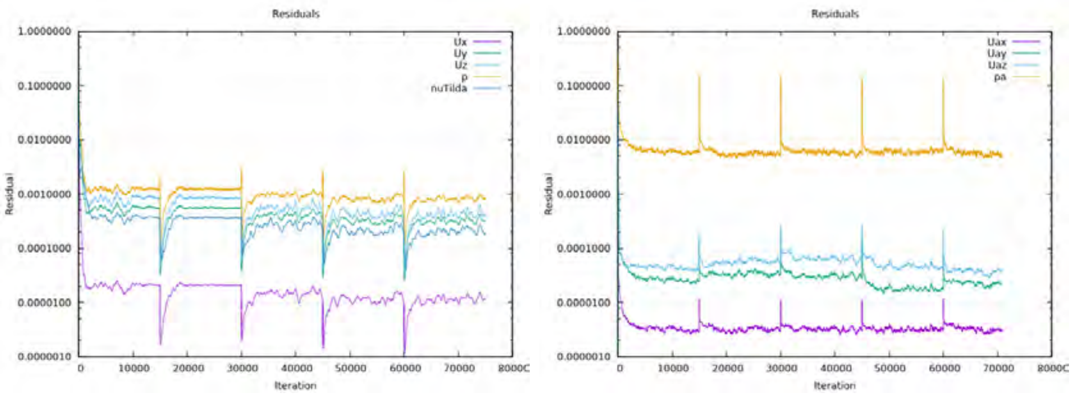

(a) (b)

Figure 6.20: *Residuals of the flow and adjoint equations during the optimization run B. Spalart-Allmaras turbulence model. Left - Primal. Right - Adjoint.*

(a) Baseline vs Optimized geometry. Optimized geometry on the left side of the figure.

(b) Baseline vs Optimized geometry. Optimized geometry on the left side of the figure.

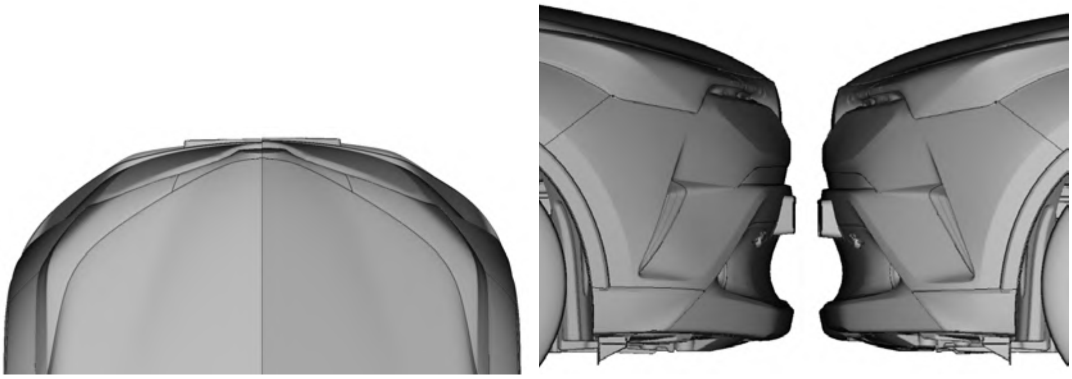

(c) Baseline vs Optimized geometry. Optimized geometry on the right side of the figure.

(d) Baseline vs Optimized geometry. Optimized geometry on the left side of the figure.

Figure 6.21

In figures 6.22, 6.23(a) and 6.23(b), the morphed surface is colored according to the magnitude of the displacement applied to it.

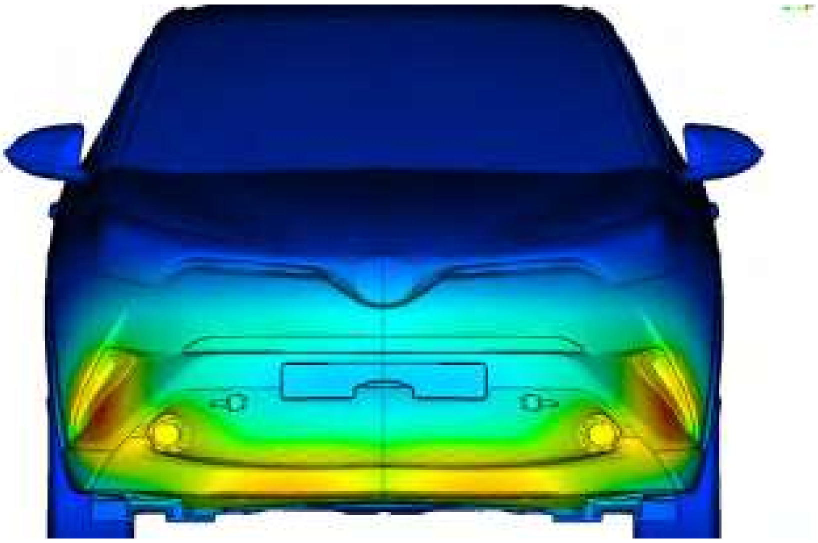

Figure 6.22: *Magnitude of the displacement of the surface CFD mesh nodes - Front view.*

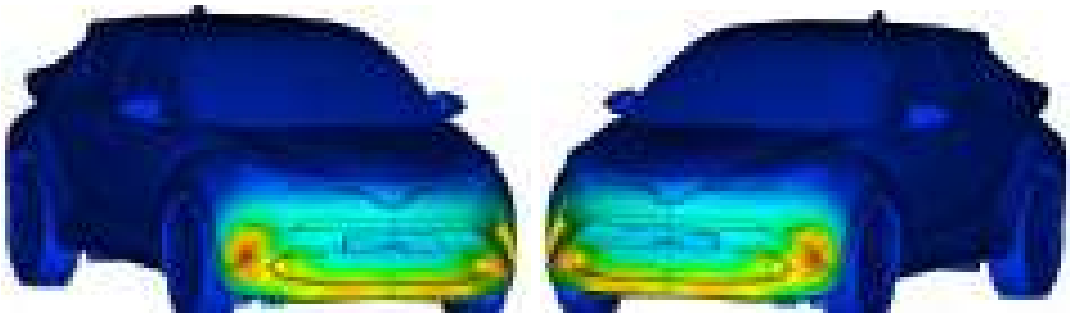

(a) (b)

Figure 6.23: *Magnitude of the displacement of the surface CFD mesh nodes. Side views.*

Figure 6.24 shows the maximum magnitude of the adjoint velocity and pressure over the iterations and optimization cycles. These provide a decisive indication of the convergence of the adjoint simulation and the instability of the solution is clear from this chart. Nevertheless, convergence is achieved in each cycle.

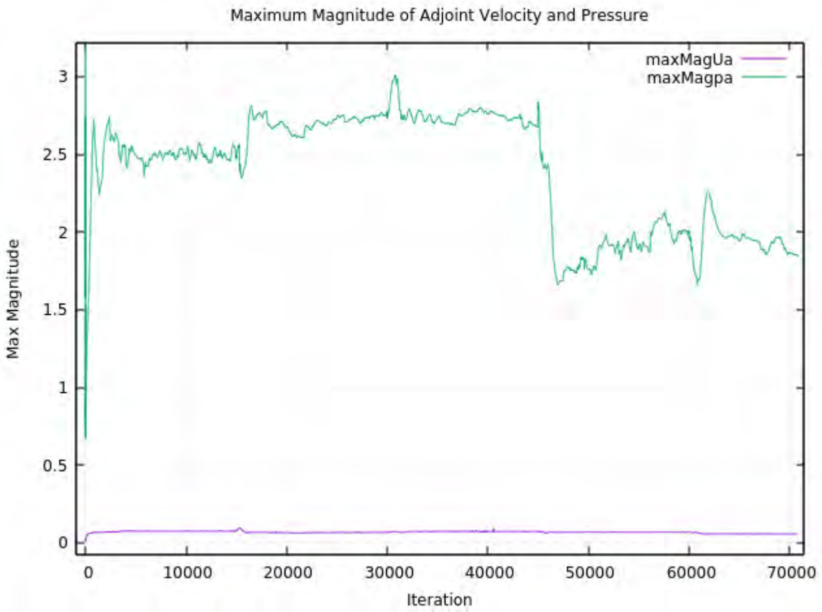

Figure 6.24: *Maximum magnitude of the adjoint velocity magnitude and pressure values obtained over the iterations of the solution. Monitoring them gives a good indication of the stability of the solution.*

Chapter 7

Summary - Conclusions

In this diploma thesis, the application of the continuous adjoint method developed by the PCOpt/NTUA to a Toyota passenger vehicle was investigated and the potential of this method for external aerodynamic optimization of passenger cars was examined and confirmed.

Initially, the flow problem was solved in the OpenFOAM$^{®}$ environment using the RANS equations for steady-state, turbulent flows of an incompressible fluid. Three turbulence models were used, namely the $k-\epsilon$, the $k-\omega$ SST and the Spalart-Allmaras, all of them with wall-functions. Their ability to accurately predict the drag coefficient and to compute the flow field around the car was tested and the results were discussed. To do this, a CFD mesh of the full model of the car with a detailed underbody and a closed engine compartment was used. Wind tunnel experiments that were conducted during the composition of this thesis led to the conclusion that the the $k-\omega$ SST and the Spalart-Allmaras models can give accurate flow predictions. On the other hand, the $k-\epsilon$ model appeared to be less satisfactory for this particular application. It computed high shear stresses on the surface and a delayed flow separation at the rear part of the car compared to the two other models, which resulted in a higher value of the drag coefficient (approximately 7%).

Following this, the adjoint problem was solved and the sensitivity derivatives were computed. The latter were used to create the sensitivity maps. These gave concrete and precise indications on the appropriate -inwards or outwards- morphing of the surface of the car in order to minimize the drag coefficient. The diversity of the patterns among the sensitivity maps computed from the three turbulence models was discussed and the maps were compared, taking into account the different flow fields that were used for their computation. What is more, the impact of the discretization order of the turbulence equations during the primal solution on the resulting sensitivity map was investigated. To do this, the flow problem was solved using the $k - \epsilon$ model with 1^{st} and 2^{nd} order discretization schemes for the turbulence PDEs and following that the sensitivity maps from the two cases were computed. The results indicate that accuracy in the modeling of turbulence is crucial in areas where the flow is governed by random, chaotic fluctuation and eddies, such as the rear part of the car. There, the sign of the sensitivity derivatives might change if the turbulence has not been properly modeled. Overall, the effect of turbulence in such applications is vital and should not be neglected.

Furthermore, issues on the stability of the primal and adjoint simulations were addressed together with measures in which it can be assisted. The symmetry of the solution was also discussed, and an effort to increase it in the primal and adjoint fields was made. Averaging the solution proved to positively influence both the symmetry of the solution and the convergence and stability of the adjoint solution. Finally, the degree in which the diversity between the three flow fields obtained from the $k-\epsilon$, the $k-\omega$ SST and the Spalart-Allmaras models was amplified by the adjoint solution was also investigated. As far as the latter is concerned, it appears that in this application, differences in the primal velocity and pressure fields were more evident in the computed sensitivity derivatives.

Finally, the shape optimization of the car was performed using the automatic shape morphing software provided by the PCOpt/NTUA. It shall be noted that, during the composition of this thesis, additions to the shape morphing software were made. These were focused on the freedom of the control points movement, the direction in which the shape morphing can be performed and the spacial set-up, movement and rotation of the control box. The areas on which the optimization was focused were selected according to the previously computed sensitivity maps. Specifically, these were areas that resided in parts of the car with high sensitivity w.r.t. shape deformation and that could be changed (shape changes cannot be performed in all parts of the car and priority was therefore given to areas of practical interest). These included the front and rear bumper, the spoiler and the second spoiler of the car located between the rear lamps. The decrease in the drag coefficient achieved during one optimization cycle of the front bumper reached 2% with a maximum displacement of the surface nodes of approximately 2cm.

Bibliography

[1] H. Tennekes and J. L. Lumley, *A First Course in Turbulence, Cambridge, Mass. :MIT Press*, 1972.

[2] D. C. Wilcox, *Turbulence Modeling for CFD, DCW Industries, Incorporated*, 1994.

[3] D. Hummel, *On the vortex formation over a slender wing at large angles of incidence*, AGARD-CP-247, Paper 15, 1978.

[4] S.r Ahmed, G. Ram, G. Faltin, *Some salient features of the time averaged ground vehicle wake*, Dokumentation Kraftfahrtwesen e.V. 1984.

[5] G. Karpouzas, E.M. Papoutsis–Kiachagias, T. Schumacher, E. de Villiers, K.C. Giannakoglou, C. Othmer, *Adjoint Optimization for Vehicle External Aerodynamics*, JSAE Annual Congress, 2015.

[6] D. L. Sondak, *Wall functions for the k-ϵ turbulence model in generalized nonorthogonal curvilinear coordinates*, Retrospective Theses and Dissertations. 9954. 1992.

[7] G. Kalitzin, G. Medic, G. Iaccarino, P. Durbin, *Near-wall behavior of RANS turbulence models and implications for wall functions*, Journal of Computational Physics, Volume 204, Issue 1, 2005.

[8] F. Liu, *A thorough description of how wall functions are implemented in OpenFOAM*, In proceedings of CFD with openSource software, 2016.

[9] D. A. Field, V. Komkov, *Theoretical Aspects of Industrial Design. Society for Industrial and Applied Mathematics Philadelphia, PA, USA*, 1992.

[10] J. D. Anderson, Jr. *Fundamentals of Aerodynamics, Second Edition. McGraw-Hill*, 1991.

[11] W. Anderson, V. Venkatakrishnan, *Aerodynamic design optimization on unstructured grids with a continuous adjoint formulation.*, Institute for Computer Applications in Science and Engineering (ICASE), 1997.

[12] L. Germanou, *Defroster nozzle shape optimization using the continuous adjoint method*, Diploma Thesis NTUA, 2016

[13] J. Boussinesq, *Essai sur la théorie des eaux courantes, Mémoires présentés par divers savants à l'Académie des Sciences 23*, 1887.

[14] D. B. Spalding, *A Single Formula for the "Law of the Wall"*, Journal of Applied Mechanics, vol. 28, issue 3, 1961.

[15] S. Prabhakara and M. D. Deshpand, *The No-Slip Boundary Condition in Fluid Mechanics*, Resonance, Volume 9, issue 5, 2004.

[16] L.L. Ferrás, J.M. Nóbrega, F.T. Pinho, O.S. Carneiro, *Implementation of a Slip Boundary Condition in a Finite Volume Code Aimed to Predict Fluid Flows. Conference: II Conferência Nacional de Métodos Numéricos em Mec ânica de Fluidos e Termodinâmica Universidade de Aveiro*, 2008.

[17] P. R. Spalart, S. R. Allmaras, *A One-Equation Turbulence Model for Aerodynamic Flows*, 30th Aerospace Sciences Meeting and Excibit, Reno, NV, U.S.A. , 1992.

[18] F. R. Menter, *Zonal Two Equation k-ω Turbulence Models for Aerodynamic Flows*, AIAA Fluid Dynamics Conference, Orlando, FL, U.S.A. , 1993.

[19] F. R. Menter, *Two-Equation Eddy-Viscosity Turbulence Models for Engineering Applications*, AIAA Journal, Vol. 32, No.8, 1994.

[20] D. C. Wilcox, *Formulation of the k–ω Turbulence Model Revisited*, AIAA Journal, Vol 46, No 11, 2008.

[21] H. K. Versteeg, W. Malalasekera, *An Introduction to Computational Fluid Dynamics: The Finite Volume Method. Harlow, England: Pearson Education Ltd*, 2007.

[22] E. A. Cowen *Canonical Turbulent Flows*, 2017.

[23] W. P. Jones, B. E. Launder, *The Prediction of Laminarization with a Two-Equation Model of Turbulence. International Journal of Heat and Mass Transfer, Volume 15, Issue 2*, 1972.

[24] B. E. Launder, B. I. Sharma, *Application of the Energy-Dissipation Model of Turbulence to the Calculation of Flow Near a Spinning Disc*, Letters in Heat and Mass Transfer, Vol. 1, Issue 2, 1974.

[25] *https://www.cfd-online.com*

[26] *https://www.openfoam.com*

[27] U. Aktas, K. Abdallah, *Aerodynamics Concept Study of Electric Vehicles Drag Reduction and Range Increase*, Master's Thesis, Department of Applied Mechanics, Chalmers University of Technology, Göteborg, Sweden, 1974.

[28] M. B. Giles, N. A. Pierce, *An Introduction to the Adjoint Approach to Design.*, SAE Technical Paper, 1992.

[29] C. Othmer, *CFD Topology and Shape Optimization with Adjoint Methods, Volkswagen AG, Wolfsburg*, 2006.

[30] E.M. Papoutsis–Kiachagias, *Adjoint Methods for Turbulent Flows, Applied to Shape or Topology Optimization and Robust Design.* PhD Thesis, NTUA, 2013.

[31] J. A. Samareh, *Aerodynamic Shape Optimization Based on Free–Form Deformation.* Multidisciplinary Optimization Branch, NASA Langley Research Center, Hampton, VA, 10th AIAA/ISSMO Multidisciplinary Analysis and Optimization Conference Albany, New York 2004.

[32] K.C. Giannakoglou, D.I. Papadimitriou, E.M. Papoutsis–Kiachagias, C. Othmer, *Adjoint methods in CFD-based optimization - Gradient computation & beyond.* ECCOMAS 2012–European Congress on Computational Methods in Applied Sciences and Engineering, pp. 8523-8539, 2012.

[33] E.M. Papoutsis–Kiachagias, K.C. Giannakoglou, C. Othmer, *Adjoint wall functions: Validation and application to vehicle aerodynamics Authors of Document.*. 11th World Congress on Computational Mechanics, WCCM 2014, 5th European Conference on Computational Mechanics, ECCM 2014 and 6th European Conference on Computational Fluid Dynamics, ECFD 2014, pp. 7593-7604, 2014.

[34] K.C. Giannakoglou, D.I. Papadimitriou, E.M. Papoutsis–Kiachagias, I.S. Kavvadias, *Adjoint methods for shape optimization and robust design in fluid mechanics.* OPT-i 2014 - 1st International Conference on Engineering and Applied Sciences Optimization, Proceedings, pp. 2252-2265, 2014.

[35] E.M. Papoutsis–Kiachagias, K.C. Giannakoglou, *Continuous Adjoint Methods for Turbulent Flows, Applied to Shape and Topology Optimization: Industrial Applications,* Archives of Computational Methods in Engineering, Volume 23, Issue 2, pp 255–299, 2014.

[36] E.M. Papoutsis–Kiachagias, A.S. Zymaris, I.S. Kavvadias, D.I. Papadimitriou, K.C. Giannakoglou *The continuous adjoint approach to the k–ϵ Turbulence model for shape optimization and optimal active control of turbulent flows.* Engineering Optimization, 47 (3), pp. 370-389, 2015.

[37] I.S. Kavvadias, E.M. Papoutsis–Kiachagias, G. Dimitrakopoulos, K.C. Giannakoglou, *The continuous adjoint approach to the k–ω SST turbulence model with applications in shape optimization.* Engineering Optimization, 47 (11), pp. 1523-1542, 2015.

[38] E.M. Papoutsis–Kiachagias, N. Magoulas, J. Mueller, C. Othmer, K.C. Giannakoglou, *Noise reduction in car aerodynamics using a surrogate objective function and the continuous adjoint method with wall functions.* Computers and Fluids, 122, pp. 223-232, 2015.

[39] E.M. Papoutsis–Kiachagias, K.C. Giannakoglou, *A parameterization and mesh movement strategy based on volumetric B-splines. Applications to shape optimization.* NTUA/PCOpt/2015/01 REPORT, Athens, Greece, 2015.

[40] L. Piegl, W. Tiller, *The NURBS book.* Springer, 1997.

[41] B.E. Launder, D.B. Spalding, *The numerical computation of turbulent flows.* Computer Methods in Applied Mechanics and Engineering 3 (2): 269-289, 1974.

[42] J. H. Ferziger, M. Peric, *Computational Methods for Fluid Dynamics.* 3rd Edition. Springer, 2001.

[43] K.C. Giannakoglou, *Design of optimal aerodynamic shapes using stochastic optimization methods and computational intelligence.* Progress in Aerospace Sciences 38 43–76, 2002.

[44] K.C. Giannakoglou, D.I. Papadimitriou, I.C. Kampolis, *Aerodynamic shape design using evolutionary algorithms and new gradient-assisted metamodels.* Comput. Methods Appl. Mech. Engrg. 195 6312–6329, 2006.

[45] K.C. Giannakoglou. Optimization Methods in Aerodynamics. Notes, National Technical University of Athens, 2005 (in Greek).

[46] *https://www.wikipedia.org*

[47] M. Samuelčík *Bézier and B–spline volumes Project of Dissertation.* Comenius University, Bratislava, 2005.

[48] D. Soban, *Review of Basic concepts*
The vocabulary of design

Part II

Extended summary in Greek

Εθνικο Μετσοβιο Πολυτεχνειο
Σχολή Μηχανολόγων Μηχανικών
Τομέας Ρευστών
Μονάδα Παράλληλης Υπολογιστικής Ρευστοδυναμικής
& Βελτιστοποίησης

Εφαρμογή της Συνεχούς Συζυγούς Μεθόδου στην Αεροδυναμική Βελτιστοποίηση Επιβατικού Αυτοκινήτου

Εκτενής Περίληψη Διπλωματικής Εργασίας

Παναγιωτης Κουτσαντωνης

Επιβλέπων:

Κυριάκος Χ. Γιαννακογλου, Καθηγητής ΕΜΠ

Αθήνα, Φεβρουάριος 2018

ΕΘΝΙΚΟ ΜΕΤΣΟΒΙΟ ΠΟΛΥΤΕΧΝΕΙΟ
Σχολή Μηχανολόγων Μηχανικών
Τομέας Ρευστών
Μονάδα Παράλληλης Υπολογιστικής Ρευστοδυναμικής
& Βελτιστοποίησης

Εφαρμογή της Συνεχούς Συζυγούς Μεθόδου στην Αεροδυναμική Βελτιστοποίηση Επιβατικού Αυτοκινήτου

Εκτενής Περίληψη Διπλωματικής Εργασίας

ΠΑΝΑΓΙΩΤΗΣ ΚΟΥΤΣΑΝΤΩΝΗΣ

Επιβλέπων: Κυριάκος Χ. ΓΙΑΝΝΑΚΟΓΛΟΥ, Καθηγητής ΕΜΠ

Αθήνα, Φεβρουάριος 2018

Περίληψη

Στη διάρκεια της διπλωματικής αυτής εργασίας πραγματοποιήθηκε εφαρμογή της συνεχούς συζυγούς μεθόδου η οποία αναπτύχθηκε από τη Μονάδα Παράλληλης Υπολογιστικής Ρευστοδυναμικής & Βελτιστοποίησης (ΜΠΥΡ&Β) της Σχολής Μηχανολόγων Μηχανικών του Εθνικού Μετσόβιου Πολυτεχνείου (ΕΜΠ) σε περιβάλλον ανοικτού λογισμικού OpenFOAM® για την αεροδυναμική βελτιστοποίηση επιβατικού αυτοκινήτου. Η αεροδυναμική αντίσταση ή οπισθέλκουσα είναι μια από τις κύριες πηγές απώλειας ενέργειας των αυτοκινήτων και, συνεπώς, η ελαχιστοποίησή της αποτελεί πρωτεύοντα στόχο της αυτοκινητοβιομηχανίας. Με τη θέσπιση αυστηρότερης νομοθεσίας σχετικά με τις εκπομπές καυσαερίων και την ανάπτυξη ηλεκτρικών και υβριδικών αυτοκινήτων καθώς και κινητήρων υδρογόνου, η ανάγκη για ελαχιστοποίηση των απωλειών ενέργειας είναι πλέον αδήριτη.

Η ανάλυση της ροής έγινε με αριθμητική επίλυση των εξισώσεων Navier-Stokes για ασυμπίεστο ρευστό και χρονικά μόνιμη, τυρβώδη ροή. Κατά την πραγματοποιηθείσα μελέτη έγινε χρήση τριών διαφορετικών μοντέλων τύρβης, του k-ε, του k-ω SST και του Spalart-Allmaras. Τα αποτελέσματα συγκρίθηκαν και έγινε ανάλυση της ικανότητας πρόλεξης αυτών των μοντέλων τύρβης σε περιοχές που παρουσιάζουν μεγάλες κλίσεις πίεσης και στις οποίες αναμένεται αποκόλληση της ροής. Το ενδιαφέρον επικεντρώνεται

στην αποτελεσματικότητα κάθε μοντέλου τύρβης στην ακριβή πρόλεξη του συντελεστή αντίστασης του οχήματος και των διαφόρων φαινομένων που σχετίζονται με αυτόν. Τα αποτελέσματα συγκρίθηκαν με πειραματικές μετρήσεις.

Κατόπιν πραγματοποιήθηκε επίλυση του συζυγούς προβλήματος χρησιμοποιώντας λογισμικό το οποίο δημιουργήθηκε από τη ΜΠΥΡ&Β/ΕΜΠ στο περιβάλλον OpenFOAM® και έγινε υπολογισμός των παραγώγων ευαισθησίας. Ιδιαίτερο ενδιαφέρον παρουσιάζει ο χάρτης ευαισθησίας πάνω στην επιφάνεια του αυτοκινήτου, ο οποίος αποτελεί μια γραφική αποτύπωση των παραγώγων της αντικειμενικής συνάρτησης ως προς την κάθετη μετατόπιση των κόμβων του επιφανειακού πλέγματος επάνω στο αυτοκίνητο και υποδηλώνει προς τα που πρέπει να μετακινηθεί η εξωτερική επιφάνεια του αυτοκινήτου ούτως ώστε να μειωθεί η αεροδυναμική αντίσταση αυτού. Πραγματοποιείται σύγκριση των υπολογισθέντων χαρτών ευαισθησίας από τα τρία μοντέλα τύρβης. Γίνεται επίσης ανάλυση της επιρροής της τάξης ακρίβειας της διακριτοποίησης των εξισώσεων του μοντέλου τύρβης κατά την επίλυση του πρωτεύοντος προβλήματος στους υπολογιζόμενους χάρτες ευαισθησίας. Εξετάζονται και άλλα θέματα, όπως η σύγκλιση και η ευστάθεια της αριθμητικής επίλυσης του πρωτεύοντος και συζυγούς προβλήματος.

Για τη βελτιστοποίηση μορφής του οχήματος, χρησιμοποιήθηκε μοντέλο μισού αυτοκινήτου. Για την παραμετροποίηση της γεωμετρίας του αυτοκινήτου έγινε χρήση λογισμικού το οποίο αναπτύχθηκε απο τη ΜΠΥΡ&Β/ΕΜΠ και βασίζεται στις ογκικές B-Splines. Στη συνέχεια, διερευνήθηκε η βέλτιστη μεταβολή της γεωμετρίας του αυτοκινήτου, ούτως ώστε το αποτέλεσμα της βελτιστοποίησης να αποτελεί ένα αποδεκτό για τη βιομηχανία σχήμα. Για το σκοπό αυτό εφαρμόστηκαν και εξετάστηκαν διάφορες παραλλαγές των ρυθμίσεων του μορφοποιητή με στόχο το βέλτιστο έλεγχο της προς σχεδιασμό επιφάνειας. Με τον τρόπο αυτό επιτεύχθηκε η μορφοποίηση συγκεκριμένων μεμονωμένων περιοχών του οχήματος, ικανοποιώντας τους περιορισμούς και τα όρια που θέτει η βιομηχανία -για σχεδιαστικούς κυρίως λόγους- σχετικά με τα περιθώρια μεταβολής της γεωμετρίας.

Ακρωνύμια

ΕΜΠ	Εθνικό Μετσόβιο Πολυτεχνείο
ΜΠΥΡ&Β	Μονάδα Παράλληλης Υπολογιστικής Ρευστοδυναμικής & Βελτιστοποίησης
ΥΡΔ	Υπολογιστική Ρευστοδυναμική
ΜΔΕ	Μερικές Διαφορικές Εξισώσεις

NTUA	National Technical University of Athens
PCopt	Parallel CFD & Optimization Unit
TME	Toyota Motor Europe
CFD	Computational Fluid Dynamics
OpenFOAM	Open Field Operation And Manipulation
CPU	Central Processing Unit
GPU	Graphics Processing Unit
FAE	Field Adjoint Equation
RANS	Reynolds-Averaged Navier-Stokes

Περιεχόμενα

7.1 Εισαγωγή

7.1.1 Αεροδυναμική Αντίσταση

Η αεροδυναμική αντίσταση ή οπισθέλκουσα αποτελεί μια από τις κύριες ποσότητες χαρακτηρισμού της αεροδυναμικής των επίγειων και εναέριων μεταφορικών μέσων. Στόχο της έρευνας στον τομέα αυτό αποτελεί η ακριβής πρόλεξη και, κατ'επέκταση, η ελαχιστοποίησή της. Η αεροδυναμική αντίσταση είναι μια από τις κύριες δυνάμεις που ασκούνται σε ένα σώμα το οποίο μετακινείται μέσα σε ρευστό. Καθώς το σώμα κινείται μέσα στο ρευστό, ασκείται σε αυτό πίεση κάθετη στην επιφάνεια του και διατμητική τάση εφαπτομενική στην επιφάνεια αυτού. Οι δύο αυτές κατανομές δυνάμεων είναι υπεύθυνες για τη συνολική δύναμη που ασκείται στο σώμα από το ρευστό, ανεξάρτητα από την πολυπλοκότητα του σχήματός του. Με την ολοκλήρωση των ποσοτήτων αυτών γύρω από την επιφάνεια του σώματος προκύπτει η συνολική δύναμη $\overrightarrow{R}$ και ροπή $\overrightarrow{M}$ που ασκείται στο σώμα.

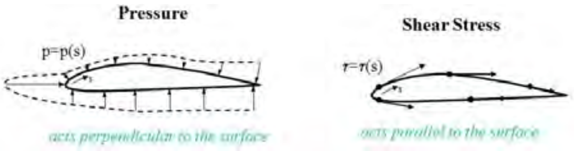

Σχήμα 7.1: *Κατανομή πίϵσης και διατμητικής τάσης σϵ σώμα κινούμϵνο μέσα σϵ ρευστό. [22]*

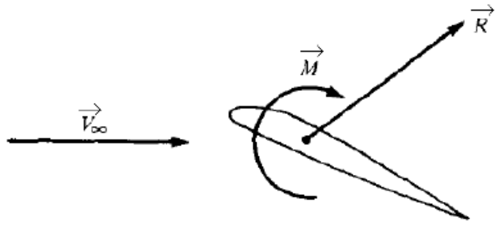

Σχήμα 7.2: *Δύναμη $\overrightarrow{R}$ και ροπή $\overrightarrow{M}$ που ασκείται σε σώμα κινούμενο μέσα σε ρευστό. [3]*

Η προκύπτουσα δύναμη $\overrightarrow{R}$ και ροπή $\overrightarrow{M}$ μπορεί να αναλυθεί στις τρείς συνιστώσες του συστήματος συντεταγμένων. Λαμβάνοντας υπόψη τη διεύθυνση του ελεύθερου ρεύματος $\overrightarrow{V_\infty}$, ορίζονται δυο βασικές δυνάμεις που ασκούνται στο σώμα, η δύναμη άνωσης και η οπισθέλκουσα. Για ένα διδιάστατο πρόβλημα, η άνωση είναι η δύναμη που ασκείται κάθετα στη διεύθυνση του ελεύθερου ρεύματος και οπισθέλκουσα η δύναμη που ασκείται παράλληλα σε αυτήν, όπως φαίνεται στο σχήμα 7.3.

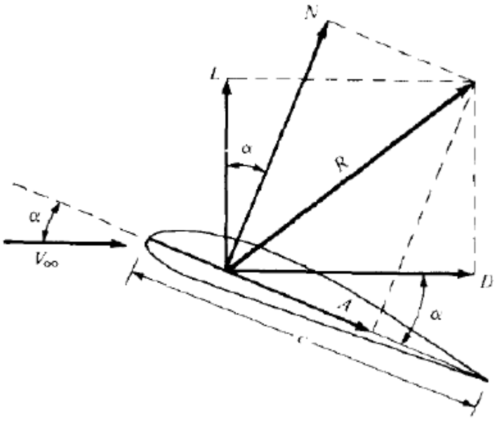

Σχήμα 7.3: *Συνιστώσες της δύναμης που ασκείται σε σώμα κινούμενο μέσα σε ρευστό. Με $\overrightarrow{L}$ συμβολίζεται η άνωση, δηλαδή η συνιστώσα της $\overrightarrow{R}$ κάθετη στη $\overrightarrow{V_\infty}$, με $\overrightarrow{D}$ η οπισθέλκουσα δηλαδή η συνιστώσα της $\overrightarrow{R}$ παράλληλη στην $\overrightarrow{V_\infty}$,[3].*

Σύμφωνα με τον παραπάνω ορισμό, η οπισθέλκουσα αποτελεί μια από τις δυνάμεις τις οποίες ένα σώμα πρέπει να υπερνικήσει προκειμένου να κινηθεί μέσα στο ρευστό. Στην περίπτωση οχήματος, η δύναμη αυτή ασκείται από τον αέρα και είναι μια από τις δυνάμεις την οποία η ισχύς του κινητήρα πρέπει να καλύψει ώστε το όχημα να κινηθεί. Επομένως, όσο μεγαλύτερη είναι η αεροδυναμική αντίσταση του οχήματος, τόσο μεγαλύτερη και η ενέργεια που δαπανάται για την κίνησή του και, άρα, η κατανάλωσή του. Είτε πρόκειται για ηλεκτροκίνητο όχημα ή για όχημα με συμβατικό κινητήρα εσωτερικής καύσης, είναι επιθυμητό η κατανάλωση ενέργειας κατά το δυνατόν να ελαχιστοποιηθεί. Γίνεται εμφανής λοιπόν ο λόγος για τον οποίο γίνεται η προσπάθεια ελαχιστοποίησης της αεροδυναμικής αντίστασης, η οποία μπορεί να εκφραστεί και αδιάστατα στη μορφή του συντελεστή αντίστασης C_D. Ο συντελεστής αντίστασης αποτελεί ένα από τα βασικά κριτήρια του επιτυχημένου ή μη αεροδυναμικού σχεδιασμού ενός οχήματος. Για ένα σώμα το οποίο κινείται μέσα σε ελεύθερο ρεύμα αέρα ταχύτητας $\overrightarrow{V_\infty}$ και πυκνότητας ρ_∞ ο συντελεστής αντίστασης ορίζεται ως

$$C_D = \frac{D}{q_\infty S} \tag{7.1}$$

όπου D το μέτρο της δύναμης αντίστασης, S η εμπρόσθια επιφάνεια του σώματος προβεβλημένη στο επίπεδο κάθετο στην ταχύτητα $\overrightarrow{V_\infty}$ και q_∞ η δυναμική πίεση για την οποία ισχύει το εξής:

$$q_\infty = \frac{1}{2}\rho_\infty V_\infty^2 \tag{7.2}$$

Η τιμή του συντελεστή αντίστασης C_D κυμαίνεται για επιβατικά αυτοκίνητα μεταξύ 0.2 και 0.4.

Αδιάστατοι συντελεστές ορίζονται με παρόμοιο τρόπο για όλες τις αεροδυναμικές δυνάμεις και ροπές που ασκούνται σε ένα σώμα. Μερικοί τέτοιοι συντελεστές είναι οι ακόλουθοι:

- Συντελεστής άνωσης $C_L = \frac{L}{q_\infty S}$
- Συντελεστής κάθετης δύναμης $C_N = \frac{N}{q_\infty S}$
- Συντελεστής ροπής $C_M = \frac{M}{q_\infty S l}$, όπου l μήκος αναφοράς

Ιδιαίτερα τα τελευταία χρόνια, με τη ραγδαία εξέλιξη των ηλεκτροκίνητων οχημάτων με περιορισμένη παροχή ενέργειας καθώς και την εισαγωγή αυστηρότερων κανονισμών και περιορισμών σχετικά με τον έλεγχο της έκλυσης καυσαερίων, η μείωση του συντελεστή αντίστασης έχει λάβει υψηλή προτεραιότητα στον τομέα της έρευνας και ανάπτυξης των αυτοκινητοβιομηχανιών.

7.1.2 Βελτιστοποίηση με τη Χρήση Υπολογιστικής Ρευστοδυναμικής

Η χρήση μεθόδων υπολογιστικής ρευστοδυναμική για την ανάλυση και βελτιστοποίηση αεροδυναμικών μορφών αποτελεί πλέον τον κυρίαρχο τρόπο υλοποίησης αεροδυναμικών μελετών ακόμα και στη βιομηχανία. Η ραγδαία μείωση του χρόνου υπολογισμού και του κόστους εφαρμογής τους, σε συνδυασμό με τη συνεχή μείωση του κόστους υπολογιστικής ισχύος και την εξέλιξη των υπολογιστικών αλγορίθμων καθιστά τον κλάδο της υπολογιστικής ρευστοδυναμικής εξαιρετικά χρήσιμο και αποδοτικό. Η δυνατότητα παραλληλοποίησης των προβλημάτων επιτρέπει τη δραματική μείωση του υπολογιστικού χρόνου με τη χρήση πολλών επεξεργαστών για την επίλυση των προβλημάτων, ή ακόμα και καρτών γραφικών (GPUs) για την ελαχιστοποίηση του χρόνου αναμονής του σχεδιαστή. Η ικανότητα τέλος των αλγορίθμων υπολογιστικής ρευστοδυναμικής να επιτυγχάνουν υψηλής ακρίβειας πρόλεξη της ροής με αποδεκτό υπολογιστικό κόστος καθιστά τις μεθόδους CFD μονόδρομο για τη βιομηχανία σήμερα.

Οι μέθοδοι βελτιστοποίησης διακρίνονται στις εξής δύο κατηγορίες, τις αιτιοκρατικές και τις στοχαστικές μεθόδους. Οι αιτιοκρατικές μέθοδοι ακολουθούν την κατεύθυνση που υπολογίζεται με την πρώτη (ή και δεύτερη) παράγωγο της αντικειμενικής συνάρτησης, με στόχο την ελαχιστοποίησή της. Η συνάρτηση αυτή ονομάζεται και συνάρτηση στόχος. Η προαναφερθείσα παράγωγος χρησιμοποιείται σε μεθόδους όπως αυτή της απότομης καθόδου ή η μέθοδος Newton.

Οι στοχαστικές μέθοδοι [21], από την άλλη, βασίζονται στην τυχαία ή τυχηματική αναζήτηση της βέλτιστης λύσης στο πεδίο των λύσεων. Ο όρος τυχηματική χρησιμοποιείται εδώ με την έννοια της στοχευμένης ή έξυπνης αναζήτησης της λύσης με χρήση μεθόδων ικανών να περιορίσουν ταχύτατα και αποτελεσματικά το πιθανό εύρος λύσεων και να εντοπίσουν τελικά το καθολικό ελάχιστο ή μέγιστο σημείο της συνάρτησης στόχου. Απαιτούν όμως μεγαλύτερο αριθμό αξιολογήσεων (τρεξιμάτων CFD) από τις αιτιοκρατικές μεθόδους.

Κάποια σημαντικά χαρακτηριστικά των δύο μεθόδων τα οποία τις καθιστούν κατάλληλες ή όχι για την εκάστοτε εφαρμογή είναι τα εξής. Σε αντίθεση με τις στοχαστικές μεθόδους, οι αιτιοκρατικές απαιτούν τον υπολογισμό της πρώτης ή δεύτερης παραγώγου της αντικειμενικής συνάρτησης ως προς τις μεταβλητές σχεδιασμού. Αυτό εισάγει κόστος στην υλοποίησή τους, το οποίο σε ορισμένες περιπτώσεις όπως λ.χ. στον υπολογισμό της δεύτερης παραγώγου ή στην περίπτωση μεγάλου αριθμού μεταβλητών σχεδιασμού, μπορεί ανάλογα με το πρόβλημα να καταστεί απαγορευτικό. Ένα άλλο μειονέκτημα των μεθόδων αυτών είναι ο κίνδυνος "εγκλωβισμού" τους σε κάποιο τοπικό ελάχιστο της συνάρτησης. Είναι όμως βέβαιο ότι με σωστό υπολογισμό της παραγώγου η μέθοδος θα οδηγήσει ταχύτατα σε κάποια βελτιωμένη λύση σε σχέση με την τρέχουσα. Οι στοχαστικές μέθοδοι από την άλλη δεν απαιτούν τον υπολογισμό κάποιας παραγώγου και είναι βέβαιο οτι με την πάροδο επαρκούς χρόνου θα εντοπίσουν το καθολικό ελάχιστο της συνάρτησης. Ο χρόνος όμως που μπορεί να απαιτηθεί ενδέχεται να είναι μεγάλος και σε ορισμένες περιπτώσεις μη-βιώσιμος για βιομηχανικές εφαρμογές.

Για την υλοποίηση ενός αλγορίθμου βελτιστοποίησης με τη χρήση CFD απαιτείται αρχικά η διακριτοποίηση του υπολογιστικου χωρίου με τη γένεση ενός υπολογιστικού πλέγματος. Στο υπολογιστικό αυτό πλέγμα γίνεται διακριτά η επίλυση των ροικών ε-

ξισώσεων από το λογισμικό αξιολόγησης. Από την επίλυση αυτή προκύπτουν τα πεδία (λ.χ. ταχύτητας και πίεσης) της ροής τα οποία είναι απαραίτητα για τον υπολογισμό της αντικειμενικής συνάρτησης.
Στη διπλωματική αυτή εργασία γίνεται υλοποίηση της μεθόδου της απότομης καθόδου με χρήση της συνεχούς συζυγούς μεθόδου [13], [14], [15] για τον υπολογισμό των απαιτούμενων παραγώγων. Η συνεχής συζυγής μέθοδος [16], [19], [4], της οποίας αναλυτική παρουσίαση και θεμελίωση ακολουθεί στο κεφάλαιο 2, διαθέτει το ισχυρό πλεονέκτημα οτι το κόστος υπολογισμού των παραγώγων δεν αυξάνεται με αύξηση του αριθμού των μεταβλητών σχεδιασμού. Η εφαρμογή της θα πραγματοποιηθεί με λογισμικό το οποίο έχει αναπτυχθεί από τη ΜΠΥΡ&Β/ΕΜΠ στο περιβάλλον OpenFOAM®.

7.1.3 Στόχος και Δομή της Διπλωματικής Εργασίας

Η διπλωματική εργασία στοχεύει στην εφαρμογή της συνεχούς συζυγούς μεθόδου για την αεροδυναμική βελτιστοποίηση μορφής ενός επιβατικού οχήματος. Με τον όρο βελτιστοποίηση μορφής νοείται η κατάλληλη μεταβολή της γεωμετρίας της εξωτερικής επιφάνειας του οχήματος με σκοπό την ελαχιστοποίηση της αεροδυναμικής του αντίστασης. Προηγείται επίλυση του ροικού προβλήματος και σύγκριση των αποτελεσμάτων τριών μοντέλων τύρβης (του k-ε, του k-ω SST και του Spalart-Allmaras) με στόχο την εύρεση του κατάλληλου για εφαρμογές ανάλυσης της ροής και βελτιστοποίησης σε συναφή προβλήματα. Στη συνέχεια, γίνεται εφαρμογή της συνεχούς συζυγούς μεθόδου για τον υπολογισμό των παραγώγων οι οποίες θα οδηγήσουν σε μια βελτιωμένη γεωμετρία. Σύμφωνα με τις παραγώγους αυτές μεταβάλλονται οι μεταβλητές σχεδιασμού, με τις οποίες το εργαλείο παραμετροποίησης μεταβάλλει το υπολογιστικό πλέγμα. Το λογισμικό παραμετροποίησης του CFD πλέγματος έχει αναπτυχθεί από τη ΜΠΥΡ&Β/ΕΜΠ και είναι συνδεδεμένο με τον κώδικα υπολογισμού παραγώγων ως ενιαίο αυτοματοποιημένο λογισμικό βελτιστοποίησης. Ως αποτέλεσμα αυτού λαμβάνεται το νέο σχήμα του αυτοκινήτου το οποίο οδηγεί σε μειωμένο συντελεστή αντίστασης από το αρχικό. Η παραπάνω διαδικασία εφαρμόζεται σε συγκεκριμένες, στοχευμένες περιοχές του οχήματος οι οποίες εντοπίζονται με χρήση των χαρτών ευαισθησίας.

Η δομή της διπλωματικής εργασίας έχει ως εξής:

- Στο κεφάλαιο 2 παρουσιάζονται οι εξισώσεις της ροής για ασυμπίεστο ρευστό και χρονικά μόνιμη, τυρβώδη ροή μαζί με τις εξισώσεις των τριών μοντέλων τύρβης που θα χρησιμοποιηθούν για την επίλυση του ροικού προβλήματος. Περιγράφεται επίσης το υπολογιστικό χωρίο και ο μορφοποιητής του. Γίνεται αναλυτική παρουσίαση της συνεχούς συζυγούς μέθοδου και εκφράζεται η αντικειμενική συνάρτηση, οι συζυγείς εξισώσεις μαζί με τις οριακές τους συνθήκες και, τέλος, ο τύπος υπολογισμού των παραγώγων ευαισθησίας.

- Στο κεφάλαιο 3 γίνεται αριθμητική πρόλεξη της ροής και ανάλυση των αποτελεσμάτων.
- Στο κεφάλαιο 4 παρουσιάζεται η επίλυση της συνεχούς συζυγούς μεθόδου και τα αποτελέσματα που προκύπτουν από αυτήν.
- Στο κεφάλαιο 5 παρουσιάζονται τα αποτελέσματα βελτιστοποίησης.
- Στο κεφάλαιο 6, τέλος, γίνεται ανακεφαλαίωση και παρουσιάζονται τα συμπεράσματα.

7.2 Διαδικασία Υπολογιστικής Ρευστοδυναμικής για την Πρόλεξη της Ροής

Στο κεφάλαιο αυτό γίνεται συνοπτική περιγραφή της διαδικασίας που ακολουθείται για την επίλυση του πρωτεύοντος και του συζυγούς προβλήματος καθώς και των βασικών χαρακτηριστικών αυτών. Παρουσιάζονται οι εξισώσεις που διέπουν τα δύο προβλήματα και τα βήματα για την υλοποίηση της βελτιστοποίησης. Ακόμη, γίνεται παρουσίαση του μορφοποιητή επιφάνειας αλλά και περιβάλλοντος πλέγματος.

7.2.1 Το Πρωτεύον Πρόβλημα

Διακριτοποίηση και Επίλυση των Εξισώσεων Ροής

Το πρωτεύον πρόβλημα συνίσταται στην αριθμητική επίλυση των εξισώσεων της ροής για ασυμπίεστο ρευστό και χρονικά μόνιμη, τυρβώδη ροή, οι οποίες είναι οι εξισώσεις διατήρησης μάζας και ορμής, ή αλλιώς εξισώσεις Reynolds Averaged Navier-Stokes (RANS) και γράφονται ως εξής:

Διατήρηση της Μάζας

$$R^p = -\frac{\partial v_j}{\partial x_j} = 0 \tag{7.3}$$

Διατήρηση της Ορμής

$$R_i^v = v_j \frac{\partial v_i}{\partial x_j} - \frac{\partial}{\partial x_j}\left[\left(\nu + \nu_t\right)\left(\frac{\partial v_i}{\partial x_j} + \frac{\partial v_j}{\partial x_i}\right)\right] + \frac{\partial p}{\partial x_i} = 0 \qquad i = 1, 2, 3 \tag{7.4}$$

όπου v_i είναι οι συνιστώσες της ταχύτητας, p η πίεση διαιρεμένη με τη σταθερή πυκνότητα ρ, ν η κινηματική συνεκτικότητα και ν_t η τυρβώδης συνεκτικότητα η οποία προκύπτει από την επιπλέον επίλυση των ΜΔΕ του μοντέλου τύρβης. Η γραφή τους ακολουθεί τη σύμβαση του Einstein σύμφωνα με την οποία επαναλαμβανόμενος δείκτης υποδηλώνει άθροιση.

Μοντελοποίηση της Τύρβης

Η ροή γύρω από το όχημα είναι τυρβώδης. Χαρακτηρίζεται δηλαδή από τυχαίες και χαοτικές μεταβολές των μεγεθών της πίεσης και της ταχύτητας στο πεδίο του χρόνου. Αυτές οι μεταβολές είναι απαραίτητο να ληφθούν υπόψη κατά την επίλυση της ροής. Η χρονική κλίμακα στην οποία λαμβάνει όμως χώρα η πλειονότητα των τυρβωδών φαινομένων και η υψηλόσυχνη ταλάντωσή των μεγεθών της ροής απαιτούν μεθόδους επίλυσης των εξισώσεων που αυξάνουν δραστικά το υπολογιστικό κόστος. Για την αποφυγή αυτού χρησιμοποιείται μοντελοποίηση και εμπειρικές σχέσεις για την περιγραφή τους. Έχουν αναπτυχθεί διάφορα μοντέλα τύρβης, καθένα από τα οποία χαρακτηρίζεται από συγκεκριμένες ιδιότητες οι οποίες το καθιστούν κατάλληλο ή όχι για διαφορετικές εφαρμογές. Στη διπλωματική αυτή εργασία έγινε χρήση και σύγκριση τριών διαφορετικών μοντέλων τύρβης, του $k-\epsilon$ [10], [11], του $k-\omega$ SST [6], [7], [8] και του Spalart-Allmaras [5], σε συνδυασμό με συναρτήσεις τοίχου [9].

Το Μοντέλο Τύρβης k-ϵ

Το μοντέλο τύρβης k-ϵ [10], [11] είναι ένα από τα πλέον διαδεδομένα μοντέλα τύρβης και χρησιμοποιείται σε μεγάλο εύρος εφαρμογών στην υπολογιστική ρευστοδυναμική. Είναι μοντέλο δύο ΜΔΕ, εισάγει δηλαδή δύο μεταβλητές για την έκφραση και περιγραφή της τύρβης, την τυρβώδη κινητική ενέργεια k και το ρυθμό καταστροφής της κινητικής ενέργειας ε. Οι εξισώσεις του είναι οι εξής:

$$\frac{\partial(kv_j)}{\partial x_j} = \frac{\partial}{\partial x_j}[\frac{\nu_t}{\sigma_k}\frac{\partial k}{\partial x_j}] + 2\nu_t E_{\mathrm{ij}}E_{\mathrm{ij}} - \varepsilon \tag{7.5}$$

$$\frac{\partial(ev_j)}{\partial x_j} = \frac{\partial}{\partial x_j}[\frac{\nu_t}{\sigma_\varepsilon}\frac{\partial \varepsilon}{\partial x_j}] + C_{1\varepsilon}2\frac{\varepsilon}{k}\nu_t E_{\mathrm{ij}}E_{\mathrm{ij}} - C_{2\varepsilon}\frac{\varepsilon^2}{k} \tag{7.6}$$

όπου $C_\mu = 0.09, C_{1\varepsilon} = 1.44, C_{2\varepsilon} = 1.92, \sigma_k = 1.0, \sigma_\varepsilon = 1.3$ είναι σταθερές ενώ η τυρβώδης συνεκτικότητα ν_t υπολογίζεται σύμφωνα με την εξίσωση

$$\nu_t = C_\mu \frac{k^2}{\varepsilon} \tag{7.7}$$

Το Μοντέλο Τύρβης $k-\omega$ SST

Το μοντέλο $k-\omega$ SST [6], [7], [8] είναι επίσης μοντέλο τύρβης δύο ΜΔΕ. Χρησιμοποιεί και αυτό μια ΜΔΕ για την τυρβώδη κινητική ενέργεια k, σε συνδυασμό με μια δεύτερη για την περιγραφή του ρυθμού καταστροφής της τύρβης ω. Οι εξισώσεις που διέπουν το μοντέλο αυτό είναι οι εξής:

$$\frac{\partial(kv_j)}{\partial x_j}=P_k-\beta^*k\omega+\frac{\partial}{\partial x_j}[(\nu+\sigma_k\nu_t)\frac{\partial k}{\partial x_j}] \tag{7.8}$$

$$\frac{\partial(\omega v_j)}{\partial x_j}=\alpha S^2-\beta\omega^2+\frac{\partial}{\partial x_j}[(\nu+\sigma_\omega\nu_t)\frac{\partial\omega}{\partial x_j}]+2(1-F_1)\sigma_{\omega 2}\frac{1}{\omega}\frac{\partial k}{\partial x_i}\frac{\partial\omega}{\partial x_i} \tag{7.9}$$

Η τυρβώδης συνεκτικότητα υπολογίζεται από τη σχέση

$$\nu_t=\frac{\alpha_1 k}{max(\alpha_1\omega,SF_2)} \tag{7.10}$$

Ισχύει ότι

$$\begin{aligned}&F_2=\tanh((max(\frac{2\sqrt{k}}{\beta^*\omega y},\frac{500\nu}{y^2\omega}))^2),P_k=min(\tau_{ij}\frac{\partial u_i}{\partial x_j},10\beta^*k\omega),\\&F_1=\tanh((min(max(\frac{\sqrt{k}}{\beta^*\omega y},\frac{500\nu}{y^2\omega}),\frac{4\sigma_{\omega 2}k}{CD_{k\omega}y^2}))^4),CD_{k\omega}=max(2\rho\sigma_{\omega 2}\frac{1}{\omega}\frac{\partial k}{\partial x_i}\frac{\partial\omega}{x_i},10^{-10}),\\&\phi=\phi_1F_1+\phi_2(1-F_1),\beta^*=\frac{9}{100}\end{aligned} \tag{7.11}$$

Τα μεγέθη $\alpha,\beta,\sigma_k,\sigma_\omega$ αποτελούν σταθερές του μοντέλου και εξαρτώνται από την περιοχή της ροής η οποία επιλύεται.

Το Μοντέλο Τύρβης Spalart-Allmaras

Το Spalart-Allmaras [5] είναι μοντέλο τύρβης μιας ΜΔΕ και ένα από τα πιο διαδεδομένα μοντέλα για εφαρμογές εξωτερικής αεροδυναμικής. Χρησιμοποιεί μια μεταβλητή για τη μοντελοποίηση της τύρβης η οποία μοιάζει με την τυρβώδη συνεκτικότητα και καλείται μεταβλητή Spalart-Allmaras, ή $\widetilde{\nu}$.

Ισχύουν τα εξής:

$$\nu_t=\widetilde{\nu}f_{v1} \tag{7.12}$$

όπου

$$f_{v1} = \frac{X^3}{X^3 + C_{v1}^3} \text{ και, } X = \frac{\widetilde{\nu}}{\nu} \tag{7.13}$$

Η μοναδική ΜΔΕ που επιλύεται είναι η ακόλουθη:

$$\frac{\partial(\tilde{\nu} v_j)}{\partial x_j} = C_{b1}(1 - f_{t2})\tilde{S}\tilde{\nu} - [C_{w1} f_w - \frac{C_{b1}}{\kappa^2} f_{t2}](\frac{\tilde{\nu}}{d})^2 + \frac{1}{\sigma}[\frac{\partial}{\partial x_j}((\nu + \tilde{\nu})\frac{\partial \tilde{\nu}}{\partial x_j}) + C_{b2}\frac{\partial \tilde{\nu}}{\partial x_i}\frac{\partial \tilde{\nu}}{\partial x_i}] \tag{7.14}$$

Τα μεγέθη $\sigma = 2/3, C_{b1} = 0.1355, C_{b2} = 0.622, \kappa = 0.41, C_{w1} = 3.239, C_{v1} = 7.1$ αποτελούν σταθερές του μοντέλου, ενώ d είναι η απόσταση από τον τοίχο. Οι ποσότητες $\tilde{S}, ft2, f_w$ υπολογίζονται σύμφωνα με τις παρακάτω εξισώσεις

$$\begin{aligned} \tilde{S} &= \Omega + \frac{\widetilde{\nu}}{\kappa^2 d^2} f_{v2}, & \Omega &= \sqrt{2W_{ij}W_{ij}}, \\ W_{ij} &= \frac{1}{2}(\frac{\partial v_i}{\partial x_j} - \frac{\partial v_j}{\partial x_i}) \end{aligned} \tag{7.15}$$

Επίσης ισχύει ότι

$$\begin{aligned} f_{v2} &= 1 - \frac{X}{1 + X f_{v1}}, & f_w &= g[\frac{1 + c_{w3}^6}{g^6 + c_{w3}^6}]^{1/6}, \\ g &= r + c_{w2}(r^6 - 6), & r &= \min[\frac{\widetilde{\nu}}{\tilde{S}\kappa^2 d^2}, 10], \\ f_{t2} &= c_{t3} e^{-c_{t4} X^2} \end{aligned} \tag{7.16}$$

Οριακές Συνθήκες

Για να είναι εφικτή η επίλυση του προβλήματος είναι απαραίτητος ο ορισμός συνθηκών για όλες τις μεταβλητές του συστήματος σε όλα τα όρια του χωρίου. Οι μεταβλητές του ροικού προβλήματος είναι το διάνυσμα της ταχύτητας v_i, η πίεση p και οι μεταβλητές του εκάστοτε μοντέλου τύρβης ($\tilde{\nu}$, k, ω, ϵ).

Στην είσοδο του χωρίου ορίζεται συνθήκη τύπου Dirichlet για την ταχύτητα και μηδενική συνθήκη Neumann για την πίεση. Σε οτι αφορά τις μεταβλητές των μοντέλων τύρβης στη είσοδο, η μεταβλητή $\tilde{\nu}$ υπολογίζεται από την τιμή της κινηματικής συνεκτικότητας του ρευστού ενώ οι τιμές των μεταβλητών k, ω και ϵ προκύπτουν από την ένταση της τύρβης Ι και την ταχύτητα του ρευστού στην είσοδο του χωρίου.

Στην έξοδο του χωρίου έχουμε μηδενική συνθήκη Dirichlet για την πίεση και μηδενική συνθήκη Neumann για την ταχύτητα και όλες τις μεταβλητές της τύρβης.
Στα στερεά όρια του χωρίου (την επιφάνεια του αυτοκινήτου και τον δρόμο) ορίζεται συνθήκη μη ολίσθησης για την ταχύτητα, μηδενική συνθήκη Neumann για την πίεση και κατάλληλες συναρτήσεις τοίχου για όλες τις μεταβλητές των μοντέλων τύρβης.

7.2.2 Το Συζυγές Πρόβλημα

Στη συνέχεια θα γίνει παρουσίαση του συζυγούς προβλήματος. Η συνεχής συζυγής μέθοδος [13], [15], [14], [16] αποτελεί μια μαθηματική μέθοδο υπολογισμού των παραγώγων μια συνάρτησης ως προς έναν αριθμό μεταβλητών. Η μαθηματική της θεμελίωση ξεκινά από τον ορισμό μιας αντικειμενικής συνάρτησης, η οποία εκφράζει την προς ελαχιστοποίηση ποσότητα. Η αντικειμενική αυτή συνάρτηση εξαρτάται αφενός από τις μεταβλητές κατάστασης του προβλήματος και αφετέρου από τις μεταβλητές σχεδιασμού οι οποίες τροποποιούνται από τον αλγόριθμο βελτιστοποίησης σε κάθε βήμα. Οι μεταβλητές κατάστασης όμως εξαρτώνται από τις μεταβλητές σχεδιασμού και, επομένως, μεταβάλλονται και αυτές σε κάθε κύκλο βελτιστοποίησης. Από τα παραπάνω γίνεται σαφές οτι η αντικειμενική συνάρτηση μεταβάλλεται αφενός άμεσα με τη μεταβολή των μεταβλητών σχεδιασμού και αφετέρου έμμεσα από την ανανέωση των μεταβλητών κατάστασης που προκύπτει ως συνέπεια της πρώτης αλλαγής. Ας είναι, λοιπόν, F η αντικειμενική συνάρτηση, για την οποία, σύμφωνα με τα ανωτέρω

$$F = F(\overrightarrow{U}(\overrightarrow{b}), \overrightarrow{b}) \tag{7.17}$$

όπου $\overrightarrow{U}$ είναι το διάνυσμα των μεταβλητών της ροής (μεταβλητών κατάστασης) και $\overrightarrow{b}$ το διάνυσμα των μεταβλητών σχεδιασμού.

Συνεπώς, η μεταβολή της F ως προς το $\overrightarrow{b}$ είναι

$$\frac{dF}{d\overrightarrow{b}} = \frac{\partial F}{\partial \overrightarrow{b}} + \frac{\partial F}{\partial \overrightarrow{U}} \frac{d\overrightarrow{U}}{d\overrightarrow{b}} \tag{7.18}$$

Στην περίπτωση της αεροδυναμικής βελτιστοποίησης μορφής ενός οχήματος μια τέτοια συνάρτηση μπορεί να είναι η οπισθέλκουσα δύναμη ή η άνωση που παράγει το αυτοκίνητο. Μεταβλητές κατάστασης είναι οι μεταβλητές του πρωτεύοντος προβλήματος δηλαδή η ταχύτητα και η πίεση σε όλο το υπολογιστικό χωρίο, ενώ μεταβλητές σχεδιασμού είναι οι μεταβλητές που περιγράφουν τη γεωμετρία του οχήματος. Σε κάθε αλλαγή των μεταβλητών σχεδιασμού κατά τη βελτιστοποίηση θα μεταβληθεί το σχήμα του αυτοκινήτου και με τη σειρά τους θα παραχθούν νέα πεδία ταχύτητας και πίεσης γύρω από αυτό. Στη διπλωματική αυτή εργασία, στόχος ήταν η ελαχιστοποίηση της αεροδυναμικής αντίστασης, επομένως αυτή είναι η αντικειμενική συνάρτηση του προβλήματος, και ορίζεται από τη σχέση

$$F = \int_{\S tar} [(p\delta_i^j - \tau_{ij})r_i]n_j dS \tag{7.19}$$

Στη συνέχεια προστίθεται η συνάρτηση αυτή στα χωρικά ολοκληρώματα των εξισώσεων κατάστασης του προβλήματος οι οποίες στην περίπτωσή μας είναι οι εξισώσεις της ροής, πολλαπλασιασμένες με τις λεγόμενες συζυγείς μεταβλητές. Οι εξισώσεις αυτές ικανοποιούνται σε ολόκληρο το υπολογιστικό χωρίο και, επομένως, η συνεισφορά τους στην αντικειμενική συνάρτηση είναι μηδενική. Εκφράζοντάς τες ως $\overrightarrow{R} = \overrightarrow{R}(\overrightarrow{U}, \overrightarrow{b})$ ισχύει ότι $\overrightarrow{R} = 0$ σε όλο το υπολογιστικό χωρίο. Λαμβάνεται έτσι η επαυξημένη αντικειμενική συνάρτηση. Στην εξίσωση $F_{aug} = F + \int_\Omega u_i R_i^v d\Omega + \int_\Omega q R^p d\Omega + \sum_{k=1}^{M} \int_\Omega \Psi_k R^k d\Omega$, Ω είναι το υπολογιστικό χωρίο ενώ u_i είναι οι συζυγείς συνιστώσες της ταχύτητας, q είναι η συζυγής πίεση και Ψ_k οι συζυγείς τυρβώδεις μεταβλητές, όπου $k = 1, M$ ο αριθμός των εξισώσεων της τύρβης που επιλύονται από το εκάστοτε μοντέλο τύρβης. Η ΜΠΥΡ&Β/ΕΜΠ έχει αναπτύξει τη συνεχή συζυγή μέθοδο στην οποία πραγματοποιείται διαφόριση των εξισώσεων της τύρβης για τα μοντέλα τύρβης Spalart-Allmaras, $k - \epsilon$, $k - \omega$ και $k - \omega$ SST [12], [14], [16], [17], [18].

Διαφορίζοντας την επαυξημένη αντικειμενική συνάρτηση (από την οποία, για λόγους συντομίας, αμελείται ο τελευταίος όρος) ως προς τις μεταβλητές σχεδιασμού λαμβάνεται η ολική παράγωγος ως προς $\overrightarrow{b}$ και προκύπτει έτσι ότι

$$\frac{\delta F_{aug}}{\delta b_n} = \frac{\delta F}{\delta b_n} + \frac{\delta}{\delta b_n} \int_\Omega u_i R_i^v d\Omega + \frac{\delta}{\delta b_n} \int_\Omega q R^p d\Omega \tag{7.20}$$

Στην παραπάνω εξίσωση, ο τελεστής $\delta()/\delta b_n$ αναφέρεται στην ολική αλλαγή της εκάστοτε ποσότητας λόγω μεταβολής του b_n. Αντίθετα, η μερική παράγωγος $\partial()/\partial b_n$ παριστά τη μεταβολή της εκάστοτε ποσότητας που οφείλεται σε μεταβολή της ροής, λόγω μεταβολής της γεωμετρίας, χωρίς να συνυπολογίζεται η μεταβολή της θέσης του σημείου στο οποίο αναφέρονται οι ποσότητες αυτές. Η σχέση που συνδέει τα δύο μεγέθη είναι η ακόλουθη [12]:

$$\frac{\delta \Phi}{\delta b_n} = \frac{\partial \Phi}{\partial b_n} + \frac{\partial \Phi}{\partial x_k} \frac{\delta x_k}{\delta b_n} \tag{7.21}$$

Έπειτα από κατάλληλους μαθηματικούς χειρισμούς προκύπτει:

$$
\begin{aligned}
\frac{\delta F_{aug}}{\delta b_n} = & \int_{S_W} (u_i v_j n_j + \tau_{a,ij} n_j - q n_i) \frac{\partial v_i}{\partial b_n} dS + \int_{S_W} (u_j n_j + n_j r_j) \frac{\partial p}{\partial b_n} dS + \\
& + \int_{S_W} [-(u_i n_j + r_j n_i)] \frac{\partial \tau_{ij}}{\partial b_n} dS + \\
& + \int_{S_{W_p}} [n_j r_i \frac{\delta x_k}{\delta b_n} (\frac{\partial p}{\partial x_m} \delta_i^j - \frac{\partial \tau_{ij}}{\partial x_m})] dS + \int_{S_{W_p}} [(p\delta_i^j - \tau_{ij}) r_j] \frac{\delta n_i}{\delta b_n} dS + \\
& + \int_{S_{W_p}} [(p\delta_i^j - \tau_{ij}) r_j] n_i \frac{\delta (dS)}{\delta b_n} + \int_{S_{W_p}} (u_i R_i^v + q R^p) \frac{\delta x_k}{\delta b_n} n_k dS + \\
& + \int_{\Omega} \left\{ u_j \frac{\partial v_j}{\partial x_i} - \frac{\partial (v_j u_i)}{\partial x_j} - \frac{\partial}{\partial x_j} \left[(\nu + \nu_t) \left(\frac{\partial u_i}{\partial x_j} + \frac{\partial u_j}{\partial x_i} \right) \right] + \frac{\partial q}{\partial x_i} \right\} \frac{\partial v_i}{\partial b_n} d\Omega + \\
& + \int_{\Omega} (-\frac{\partial u_j}{\partial x_j}) \frac{\partial p}{\partial b_n} d\Omega
\end{aligned} \tag{7.22}
$$

όπου S_W και S_{W_P} τα στερεά και παραμετροποιημένα όρια του χωρίου αντίστοιχα.

Συζυγείς Πεδιακές Εξισώσεις

Για την αποφυγή υπολογισμού των μερικών παραγώγων των p και v_i ως προς τις μεταβλητές σχεδιασμού στο εσωτερικό του χωρίου λόγω του υψηλού τους κόστους, μηδενίζονται οι αντίστοιχοι συντελεστές και προκύπτουν, έτσι, οι συζυγείς εξισώσεις τις ροής:

$$
R^q = -\frac{\partial u_j}{\partial x_j} = 0 \tag{7.23}
$$

$$
R_i^u = u_j \frac{\partial v_j}{\partial x_i} - \frac{\partial (v_j u_i)}{\partial x_j} - \frac{\partial}{\partial x_j} \left[(\nu + \nu_t) \left(\frac{\partial u_i}{\partial x_j} + \frac{\partial u_j}{\partial x_i} \right) \right] + \frac{\partial q}{\partial x_i} = 0 \ , \ i = 1, 2(, 3) \tag{7.24}
$$

Συζυγείς Οριακές Συνθήκες

Η εξίσωση (7.22) γίνεται

$$\begin{aligned}\frac{\delta F}{\delta b_n} = & \int_{S_{W_p}} (u_i v_j n_j + \tau_{a,ij} n_j - q n_i + \frac{\partial F_{S_k}}{\partial v_i} n_k) \frac{\partial v_i}{\partial b_n} dS + \int_S (u_j n_j + \frac{\partial F_{S_i}}{\partial p} n_i) \frac{\partial p}{\partial b_n} dS \\ & + \int_S (-u_i n_j + \frac{\partial F_{S_k}}{\partial \tau_{ij}} n_k) \frac{\partial \tau_{ij}}{\partial b_n} dS \\ & + \int_{S_{W_p}} n_i \frac{\partial F_{S_i}}{\partial x_m} n_m \frac{\delta x_k}{\delta b_n} n_k dS + \int_{S_{W_p}} F_{S_i} \frac{\delta n_i}{\delta b_n} dS + \int_{S_{W_p}} F_{S_i} n_i \frac{\delta (dS)}{\delta b_n} + \int_{S_{W_p}} (u_i R_i^v + q R^p) \frac{\delta x_k}{\delta b_n} n_k dS\end{aligned} \tag{7.25}$$

Στη σχέση (7.25) υπάρχουν οι όροι της κλίσης πίεσης και ταχύτητας στο όριο του υπολογιστικού χωρίου ως προς τις μεταβλητές σχεδιασμού των οποίων το κόστος είναι επίσης υψηλό. Επιδιώκεται επομένως ο μηδενισμός των συντελεστών τους από τον οποίο προκύπτουν οι συζυγείς οριακές συνθήκες, οι οποίες παρουσιάζονται παρακάτω. Εδώ διαφαίνεται το μεγάλο πλεονέκτημα της συνεχούς συζυγούς μεθόδου, μέσω της οποίας γίνεται δυνατός ο υπολογισμός των ζητούμενων παραγώγων χωρίς να είναι απαραίτητη η επίλυση τόσων συστημάτων εξισώσεων όσες και οι μεταβλητές σχεδιασμού του προβλήματος, εφόσον οι συντελεστές των αντίστοιχων όρων μηδενίζονται και παρακάμπτεται ο υπολογισμός τους.

- **Συζυγείς Οριακές Συνθήκες στο Επ'Απειρο Όριο**

Στην είσοδο του χωρίου (S_I) ισχύει $\delta v_i/\delta b_n = \partial v_i/\partial b_n = 0$, αφού $\delta x_k/\delta b_n = 0$, οπότε μηδενίζεται το πρώτο ολοκλήρωμα στο δεξί μέλος της εξίσωσης (7.25). Για να μηδενιστούν το δεύτερο και το τρίτο ολοκλήρωμα της εξίσωσης τίθενται:

$$u_{\langle n \rangle} = u_j n_j = -\frac{\partial F_{S_{I,i}}}{\partial p} n_i \tag{7.26α′}$$

$$u_{\langle t \rangle}^{I} = \frac{\partial F_{S_{I,k}}}{\partial \tau_{ij}} n_k t_i^I n_j + \frac{\partial F_{S_{I,k}}}{\partial \tau_{ij}} n_k t_j^I n_i \tag{7.26β′}$$

$$u_{\langle t \rangle}^{II} = \frac{\partial F_{S_{I,k}}}{\partial \tau_{ij}} n_k t_i^{II} n_j + \frac{\partial F_{S_{I,k}}}{\partial \tau_{ij}} n_k t_j^{II} n_i \tag{7.26γ′}$$

όπου τα t_i^I, t_i^{II} είναι οι συνιστώσες του εφαπτόμενου στην επιφάνεια διανύσματος και $u_{\langle t \rangle}^I, u_{\langle t \rangle}^{II}$ είναι οι αντίστοιχες συνιστώσες της συζυγούς ταχύτητας.

Στο όριο εξόδου της ροής (S_O), ισχύει $\delta p/\delta b_n = \partial p/\partial b_n = 0$, οπότε το δεύτερο ολοκλήρωμα της εξίσωσης (7.25) μηδενίζεται. Το τρίτο ολοκλήρωμα μπορεί να αμεληθεί αν υποτεθεί μία σχεδόν ομοιόμορφη κατανομή ταχύτητας στην επιφάνεια εξόδου. Τέλος, το πρώτο ολοκλήρωμα μπορεί να απαλειφθεί, μηδενίζοντας την ολοκληρωτέα ποσότητα, με αποτέλεσμα να προκύπτουν οι εξής οριακές συνθήκες:

$$u_i v_j n_j + (\nu + \nu_t)\left(\frac{\partial u_i}{\partial x_j} + \frac{\partial u_j}{\partial x_i}\right) n_j - q n_i + \frac{\partial F_{S_{O,k}}}{\partial v_i} n_k = 0, \quad i = 1, 2(, 3) \tag{7.27}$$

- **Συζυγείς Οριακές Συνθήκες στα Σταθερά και Παραμετροποιημένα Τοιχώματα του Χωρίου**

Για τα σταθερά τοιχώματα S_W, όπως και για την επιφάνεια S_I ισχύει $\delta x_k/\delta b_n = 0$, οπότε οι συζυγείς συνθήκες που ορίστηκαν στο όριο εισόδου της ροής (7.26) συνεχίζουν να ισχύουν αρκεί, όπου αναφέρεται η F_{S_I}, να χρησιμοποιηθεί η F_{S_W}.

Για τα παραμετροποιημένα τοιχώματα (S_{W_p}), καθώς έχει επιβληθεί $v_i = 0$, ισχύει $\delta v_i/\delta b_n = 0$. Ωστόσο, καθώς $\delta x_k/\delta b_n \neq 0$, από την εξίσωση (7.21) προκύπτει η

$$\frac{\partial v_i}{\partial b_n} = -\frac{\partial v_i}{\partial x_k} n_k \frac{\delta x_m}{\delta b_n} n_m \tag{7.28}$$

Αντικαθιστώντας την εξίσωση (7.28) στο πρώτο ολοκλήρωμα του δεξιού μέλους της εξίσωσης (7.25), αυτό γράφεται ως

$$\begin{aligned} &\int_{S_{W_p}} (u_i v_j n_j + \tau_{a,ij} n_j - q n_i + \frac{\partial F_{S_k}}{\partial v_i} n_k) \frac{\partial v_i}{\partial b_n} dS = \\ -&\int_{S_{W_p}} (u_i v_j n_j + \tau_{a,ij} n_j - q n_i + \frac{\partial F_{S_k}}{\partial v_i} n_k) \frac{\partial v_i}{\partial x_k} n_k \frac{\delta x_m}{\delta b_n} n_m dS \end{aligned} \tag{7.29}$$

όρος ο οποίος περιέχεται στην έκφραση της κλίσης της αντικειμενικής συνάρτησης. Το δεύτερο και τρίτο ολοκλήρωμα απαλείφονται ικανοποιώντας τις εξισώσεις

$$u_{\langle n \rangle} = -\frac{\partial F_{S_{W_p,i}}}{\partial p} n_i \tag{7.30α'}$$

$$u^{I}_{\langle t \rangle} = \frac{\partial F_{S_{W_p,k}}}{\partial \tau_{ij}} n_k t^{I}_i n_j + \frac{\partial F_{S_{W_p,k}}}{\partial \tau_{ij}} n_k t^{I}_j n_i \tag{7.30β'}$$

$$u^{II}_{\langle t \rangle} = \frac{\partial F_{S_{W_p,k}}}{\partial \tau_{ij}} n_k t^{II}_i n_j + \frac{\partial F_{S_{W_p,k}}}{\partial \tau_{ij}} n_k t^{II}_j n_i \tag{7.30γ'}$$

7.2.3 Γένεση Πλέγματος και Επίλυση των Εξισώσεων

Εφόσον οι προαναφερθείσες ΜΔΕ που δίεπουν το πρόβλημα δεν μπορούν να λυθούν αναλυτικά, είναι απαραίτητο να γίνει επίλυση τους σε διακριτή μορφή. Για το σκοπό αυτό, ο χώρος που ορίζεται από τη γεωμετρία του αυτοκινήτου και τις νοητές επιφάνεις που την περιβάλλουν κατακερματίζεται σε μικρότερους όγκους οι οποίοι ονομάζονται κελιά ή κυψέλες. Κάθε κελί ορίζεται από τα σημεία, τις ακμές και τις πλευρές του, τα οποία χαρακτηριστικά του προσδίδουν ένα συγκεκριμένο γεωμετρικό σχήμα. Το σύνολο των κελιών αποτελεί το υπολογιστικό πλέγμα. Ανάλογα με τον τύπο και τη διάταξη των κελιών του πλέγματος αυτό μπορεί να χαρακτηριστεί ώς πολυεδρικό, τετραεδρικό, καρτεσιανό κ.α. και έχει αντίστοιχες ιδιότητες, προτερήματα και μειονεκτήματα τα οποία το καθιστούν κατάλληλο ή όχι για συγκεκριμένες εφαρμογές. Οι διακριτοποιημένες ΜΔΕ επιλύονται σε κάθε σημείο (ή κόμβο) του υπολογιστικού πλέγματος. Η επίλυση γίνεται με μια παραλλαγή του αλγορίθμου SIMPLE.
Για την επίλυση του παρόντος προβήματος χρησιμοποιήθηκαν δυο παραλλαγές του πλέγματος, μια ολόκληρου και μια μισού αυτοκινήτου . [1]

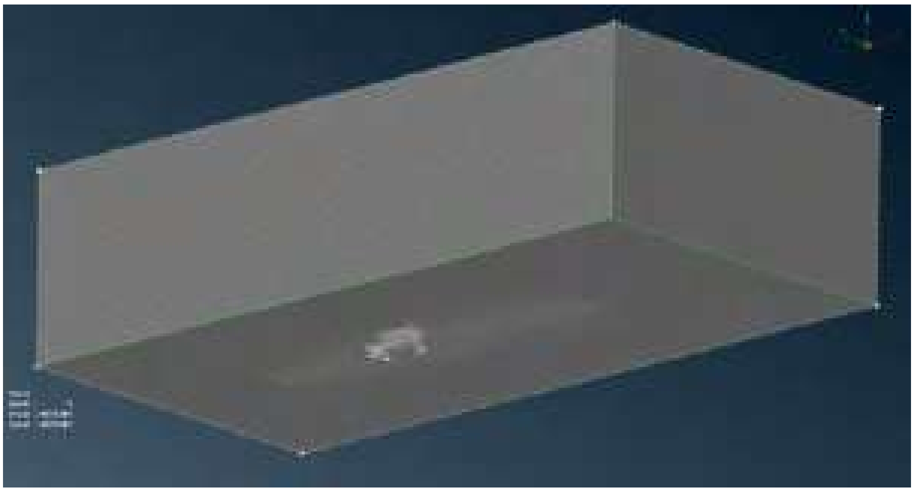

Σχήμα 7.4: *Υπολογιστικό Χωρίο.*

---

[1] Το επιφανειακό πλέγμα κατασκευάστηκε από την BETA CAE.

(α′) Γεωμετρία του οχήματος

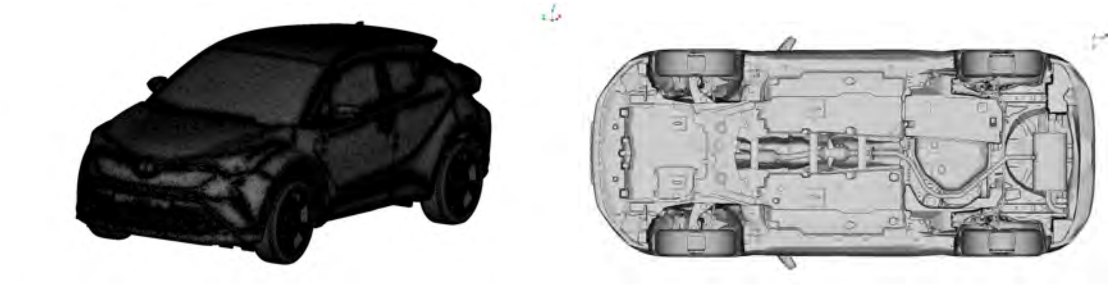

(β′) Επιφανειακό πλέγμα (γ′) Κάτω μέρος του οχήματος

Σχήμα 7.5: *Η γεωμετρία του αυτοκινήτου και το επιφανειακό πλέγμα.*

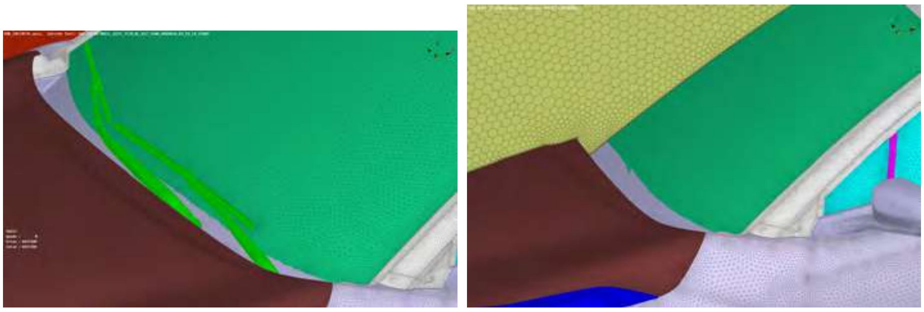

(α′) (β′)

Σχήμα 7.6: *Λεπτομέρεια στο εμπρόσθιο τζάμι στο μοντέλο ολόκληρης και μισής γεωμετρίας. Αριστερά - ολόκληρο το αυτοκίνητο με τους υαλοκαθαριστήρες, δεξιά - μισό αυτοκίνητο μετά την αφαίρεση των υαλοκαθαριστήρων.*

Η τιμή του y^+ των βαρυκέντρων των κυψελών που είναι σε επαφή με τα στερεά τοιχώματα στο πρόβλημα ήταν κατά μέσο όρο ίση με 25.

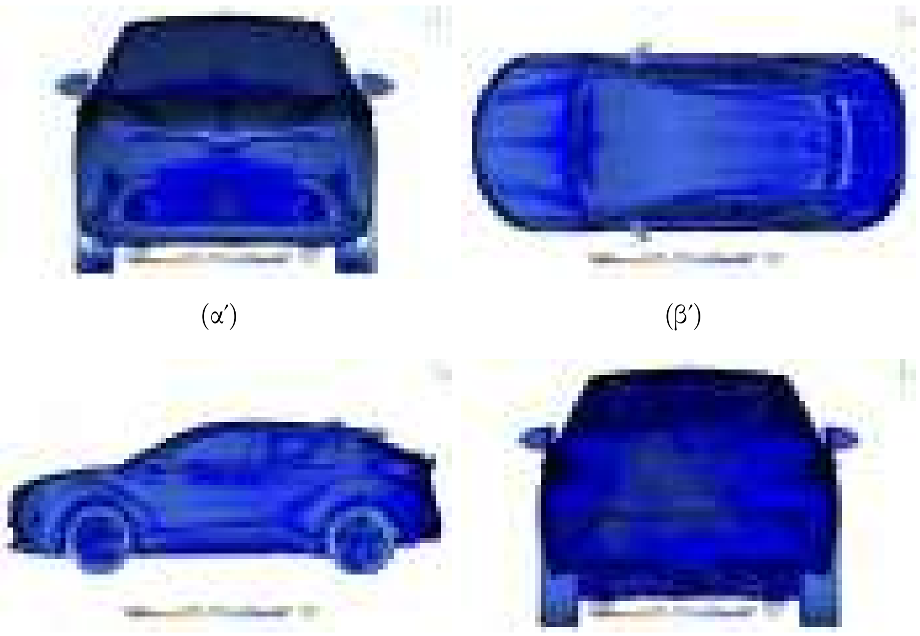

(α΄) (β΄)

(γ΄) (δ΄)

Σχήμα 7.7: y^+. *Πάνω αριστερά - εμπρόσθια όψη, πάνω δεξιά - κάτοψη, κάτω αριστερά - αριστερή όψη, κάτω δεξιά - πίσω όψη.*

Οι ΜΔΕ επιλύθηκαν σε διακριτή μορφή με μια παραλλαγή του αλγορίθμου SIMPLE, ενώ ο κώδικας υπολογισμού υπήρχε ήδη προγραμματισμένος. Ο SIMPLE αποτελεί έναν επαναληπτικό αλγόριθμο επίλυσης της ροής, ο οποίος στο OpenFOAM® κάνει χρήση της κεντρο-κυψελικής μεθόδου πεπερασμένων όγκων, σύμφωνα με την οποία ως όγκος ελέγχου λαμβάνεται ο όγκος κάθε κελιού του πλέγματος. Η επίλυση της ροής γίνεται θεωρώντας αρχικά γνωστό το πεδίο της πίεσης το οποίο είτε προκύπτει στο πρώτο βήμα από κάποια αρχικοποίηση, ή στη συνέχεια από το πεδίο που υπολογίστηκε κατά την προηγούμενη επανάληψη. Με αυτό γίνεται επίλυση της εξίσωσης της ορμής στις τρεις διαστάσεις χωρίς όμως να ικανοποιείται η εξίσωση της συνέχειας και λαμβάνεται το πεδίο της ταχύτητας. Ακολούθως, το πεδίο της πίεσης υπολογίζεται από την εξίσωση της συνέχειας και με αυτό πραγματοποιείται η διόρθωση του πεδίου της ταχύτητας κατά την επόμενη επανάληψη, καταλήγοντας τελικά στη σύγκλιση του συστήματος των εξισώσεων.

7.2.4 Μορφοποίηση της Γεωμετρίας

Η χρησιμότητα των υπολογιζομένων παραγώγων ευαισθησίας είναι διττή.

Αφενός, με τη γραφική απεικόνιση των παραγώγων της αντικειμενικής συνάρτησης ως προς την κάθετη μετατόπιση των επιφανειακών κόμβων του πλέγματος επάνω στην επιφάνεια του αυτοκινήτου κατασκευάζεται ο χάρτης ευαισθησίας του αυτοκινήτου.

Αφετέρου, οι παράγωγοι ευαισθησίας αυτές μπορούν να προβληθούν στα σημεία ελέγχου ογκικών B–Splines με τις οποίες έχει παραμετροποιηθεί το ογκικό και επιφανειακό υπολογιστικό πλέγμα [20]. Στην περίπτωση αυτή, οι μεταβλητές σχεδιασμού του συζυγούς προβλήματος είναι η μετατόπιση των σημείων ελέγχου των ογκικών B–Splines στις τρεις διαστάσεις. Ο μορφοποιητής πλέγματος ο οποίος εκτελεί την αυτοματοποιημένη διαδικασία παραμετροποίησης και μετατόπισης των σημείων του πλέγματος χωρίς την ανάγκη επαναπλεγματοποίησης έχει αναπτυχθεί από τη ΜΠΥΡ&Β/ΕΜΠ. Η χρήση αυτού για τη μορφοποίηση της γεωμετρίας συνίσταται στα παρακάτω βήματα:

- Ο προς βελτιστοποίηση χώρος περιβάλλεται από ένα δομημένο πλέγμα των σημείων ελέγχου των ογκικών B–Splines.
- Παραμετροποιούνται οι κόμβοι του επιφανειακού και ογκικού υπολογιστικού πλέγματος που περιλαμβάνονται στον παραπάνω χώρο σύμφωνα με τα σημεία ελέγχου.
- Τα σημεία ελέγχου των ογκικών B–Splines μετατοπίζονται σύμφωνα με τις υπολογισθείσες παραγώγους ευαισθησίας.
- Οι επιφανειακοί και ογκικοί κόμβοι του CFD πλέγματος μετατοπίζονται σύμφωνα με τη μετατόπιση των σημείων ελέγχου, μεταβάλλοντας το υπολογιστικό πλέγμα.

7.2.5 Αλγόριθμος Βελτιστοποίησης

Για την εκτέλεση μίας αυτοματοποιημένης διαδικασίας βελτιστοποίησης μορφής, χρησιμοποιείται ο επιλύτης του πρωτεύοντος και συζυγούς προβλήματος μαζί με το λογισμικό μορφοποίησης [20]. Η διαδικασία έχει ως εξής:

1. Ορίζεται ο χώρος που εμπεριέχει την υπό βελτιστοποίηση γεωμετρία. Ορίζεται το πλήθος των σημείων ελέγχου και ο βαθμός των συναρτήσεων βάσης με βάση τα παραπάνω. Έτσι δημιουργείται το δομημένο πλέγμα των σημείων ελέγχου.
2. Προσδιορίζονται τα σημεία του υπολογιστικού πλέγματος που εμπεριέχονται στο πλέγμα των σημείων ελέγχου. Για αυτά τα σημεία υπολογίζονται οι παραμετρικές συντεταγμένες.
3. Υπολογίζονται οι παραμετρικές συντεταγμένες των σημείων που βρέθηκαν κατά το βήμα 2.
4. Επίλυονται οι εξισώσεις ροής.
5. Υπολογίζεται η τιμή της αντικειμενικής συνάρτησης.
6. Επιλύονται οι συζυγείς εξισώσεις.
7. Υπολογίζεται η κλίση της αντικειμενικής συνάρτησης ως προς τους επιφανειακούς κόμβους τους πλέγματος $\frac{\delta F}{\delta x_m}$ (surface sensitivities).

8. Οι παράγωγοι αυτές προβάλλονται στα σημεία ελέγχου των ογκικών B–Splines με σκοπό τον υπολογισμό των παραγώγων ευαισθησίας ως προς αυτά.

9. Ανανεώνονται οι θέσεις των σημείων ελέγχου με τη μέθοδο της απότομης καθόδου.

10. Υπολογίζονται οι νέες θέσεις των επιφανειακών και ογκικών κόμβων του υπολογιστικού πλέγματος χρησιμοποιώντας τις ήδη υπολογισμένες παραμετρικές τους συντεταγμένες.

11. Επιστροφή στο βήμα 4.

7.3 Αποτελέσματα της Επίλυσης της Ροής

Στο κεφάλαιο αυτό θα γίνει παρουσίαση των αποτελεσμάτων της επίλυσης της ροής, ή αλλιώς του πρωτεύοντος προβλήματος. Θα γίνει σύγκριση και σύντομος σχολιασμός των πεδίων που προέκυψαν από την επίλυση των τριών μοντέλων τύρβης.

7.3.1 Σύγκριση των Τριών Μοντέλων Τύρβης

Το κάθε μοντέλο τύρβης χαρακτηρίζεται από ορισμένα βασικά στοιχεία τα οποία το καθιστούν κατάλληλο ή όχι για συγκεκριμένες εφαρμογές, συνθήκες και προβλήματα. Από την εργασία αυτή φάνηκε οτι οι λύσεις που προέκυψαν από τα δύο εκ των τριών μοντέλων που χρησιμοποιήθηκαν ήταν αρκετά ακριβείς και κοντά στις πειραματικές μετρήσεις. Αυτά ήταν το $k-\omega$ SST και το Spalart-Allmaras. Το μοντέλο $k-\epsilon$, από την άλλη, φαίνεται να υστερεί έναντι των άλλων δύο σε ότι αφορά την ακριβή πρόλεξη της αποκόλλησης και άλλων σημαντικών φαινομένων που συμβάλλουν στην εξέλιξη της ροής. Η ομοιότητα των πεδίων που προέκυψαν από την επίλυση του προβλήματος με χρήση των μοντέλων $k-\omega$ SST και Spalart-Allmaras είναι εμφανής και, όπως είναι αναμενόμενο, αντικατοπτρίζεται και στο συντελεστή αντίστασης που υπολογίσθηκε από αυτά. [2]

---

[2] Όλα τα αποτελέσματα έχουν κανονικοποιηθεί κατάλληλα για λόγους εμπιστευτικότητας.

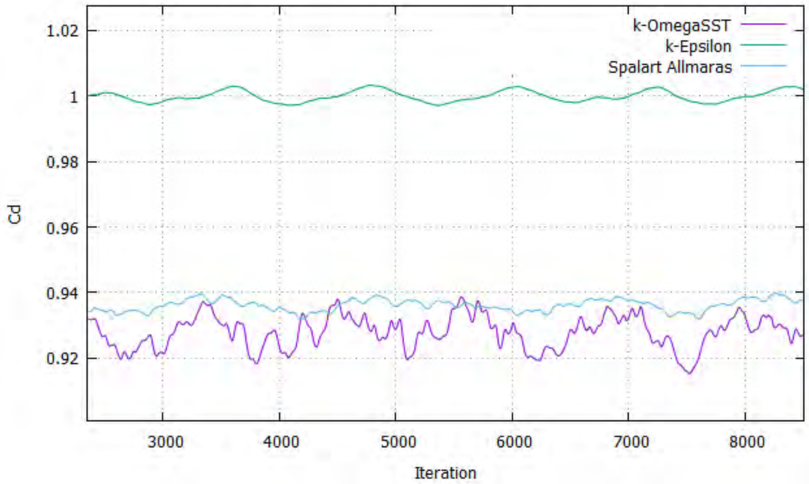

Σχήμα 7.8: *Σύγκριση των κανονικοποιημένων συντελεστών αντίστασης των τριών μοντέλων τύρβης. Τα αποτελέσματα έχουν κανονικοποιηθεί ως προς τη μέση τιμή του C_D που υπολογίσθηκε από το μοντέλο $k - \epsilon$.*

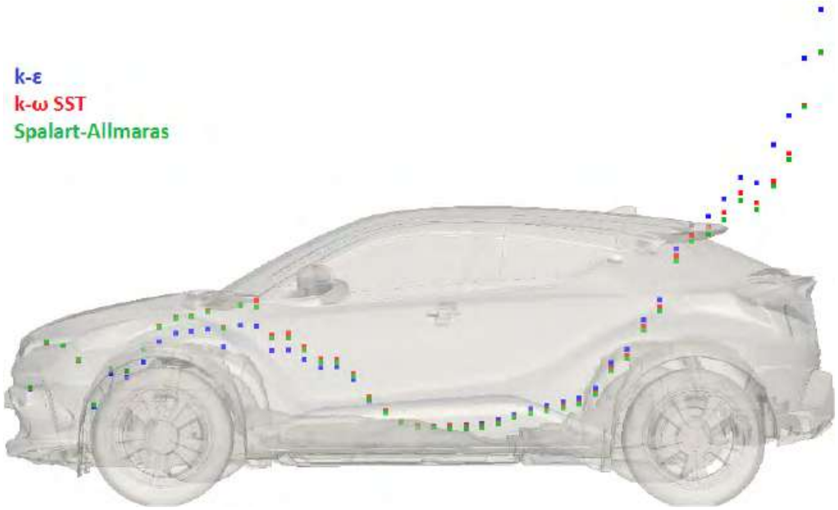

Σχήμα 7.9: *Σύγκριση του τοπικού συντελεστή αντίστασης των τριών μοντέλων τύρβης. Ο τοπικός συντελεστής αντίστασης δείχνει τη συνεισφορά του κάθε τμήματος του αυτοκινήτου κατά τον διαμήκη του άξονα, στην οπισθέλκουσά του.*

Στο σχήμα 7.9 φαίνεται ο τοπικός συντελεστής αντίστασης κατά μήκος του αυτοκινήτου, ο οποίος προκύπτει εάν η ολοκλήρωση των τάσεων που ασκούνται στην επιφάνεια δεν γίνει γύρω από τη συνολική επιφάνεια του αυτοκινήτου αλλά σε ισομήκη μικρά πλάτους διαστήματα κατά το διαμήκη του άξονα. Από τον συντελεστή αυτό, μπορούν να εντοπίστούν οι περιοχές κατά μήκος του αυτοκινήτου που συμβάλλουν περισσότερο στην αύξηση της οπισθέλκουσάς του. Στο σχήμα αυτό, το μοντέλο $k - \epsilon$ φαίνεται να υπολογίζει χαμηλότερες απώλειες λόγω αντίστασης στην περιοχή που το καπό ενώνεται με το εμπρόσθιο τζάμι (ανεμοθώρακα) και τους πυλώνες που ενώνουν το καπό με την οροφή, ενώ υπολογίζει μεγαλύτερο συντελεστή αντίστασης στο πίσω μέρος του αυτοκινήτου, σε σχέση με τα άλλα δύο μοντέλα. Το γεγονός αυτό οδηγεί στο συμπέρασμα οτι το μοντέλο αυτό υπολογίζει με μικρότερη ακρίβεια την αποκόλληση της ροής –και συγκεκριμένα μειωμένα σε σχέση με τα άλλα δυο– στη συγκεκριμένη εφαρμογή. Το τελικό C_D που υπολογίστηκε από το $k-\epsilon$ είναι περίπου 7% μεγαλύτερο από τα άλλα δύο μοντέλα.

Η υψηλότερη τιμή του συντελεστή αντίστασης όπως υπολογίσθηκε από το μοντέλο $k-\epsilon$ εξηγείται και από τα σχήματα 7.10 και 7.11, στα οποία φαίνεται η διατμητική τάση στην επιφάνεια του αυτοκινήτου και η στατική πίεση στο πίσω μέρος του αντίστοιχα. Χαρακτηριστικά ξεχωρίζει το μοντέλο $k-\epsilon$ σύμφωνα με το οποίο η διατμητική τάση στον τοίχο λαμβάνει αρκετά υψηλότερες τιμές. Η συνεισφορά όμως της τάσης λόγω συνεκτικότητας στον υπολογισμό της οπισθέλκουσας είναι περίπου μια τάξη μεγέθους μικρότερη απο αυτήν της στατικής πίεσης. Έτσι, παρότι η διατμητική τάση στον τοίχο είναι αρκετά υψηλότερη, αυτό δεν αντικατοπτρίζεται πλήρως στο υπολογιζόμενο C_D. Η χαμηλότερη πίεση, όμως, στο πίσω μέρος σε σχέση με τα δύο άλλα μοντέλα, όπως φαίνεται από το μπλέ χρώμα στα πίσω φανάρια του αυτοκινήτου στο σχήμα 7.11(γ′), συμβάλλει σημαντικά στην αύξηση της οπισθέλκουσας.

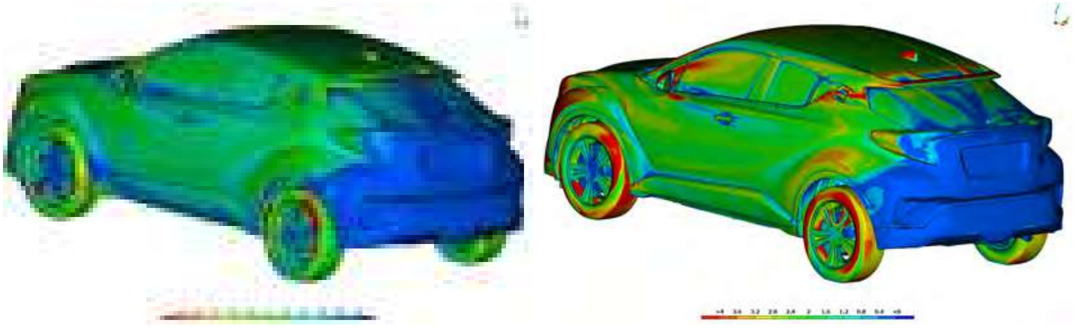

(α′) Spalart-Allmaras (β′) $k-\omega$ SST

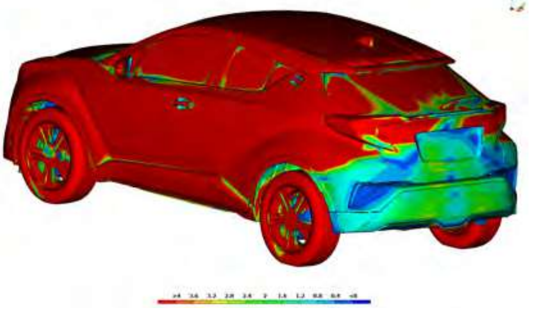

(γ′) $k-\epsilon$

Σχήμα 7.10: *Διατμητική τάση στην επιφάνεια του αυτοκινήτου.*

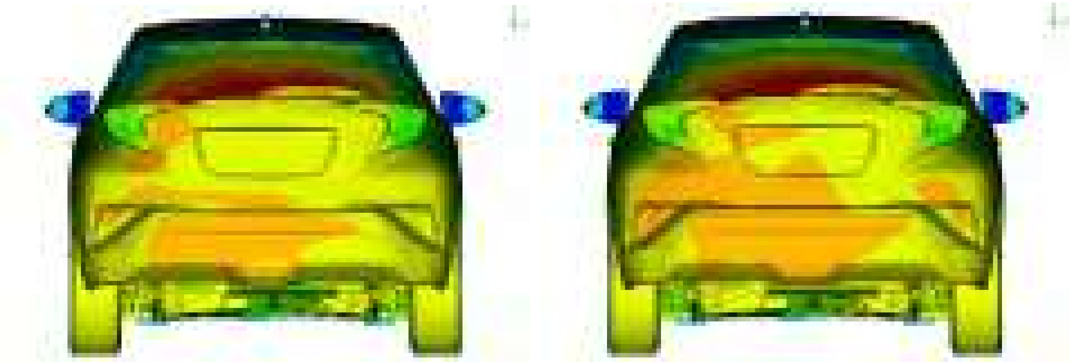

(α′) Spalart-Allmaras (β′) $k-\omega$ SST

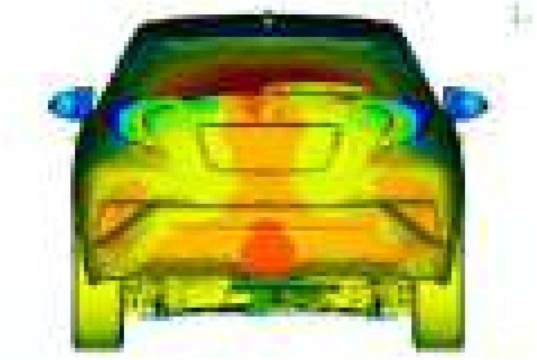

(γ′) $k-\epsilon$

Σχήμα 7.11: *Στατική πίεση στο πίσω μέρος του αυτοκινήτου. Φαίνεται η χαμηλότερη στατική πίεση όπως υπολογίσθηκε από το μοντέλο $k-\epsilon$ που δικαιολογεί τη χαμηλότερη τιμή του C_D από αυτό το μοντέλο.*

7.3.2 Εκτέλεση Πειράματος σε Αεροσήραγγα

Μετά την εκτέλεση των προσομοιώσεων της ροής με CFD και τη σύγκριση των αποτελεσμάτων τόσο μεταξύ τους όσο και με τα θεωρητικά αναμενόμενα πεδία γύρω από το αυτοκίνητο από τη βιβλιογραφία [1], [2], [3], επόμενο στάδιο της επιβεβαίωσης των αποτελεσμάτων ήταν η σύγκρισή τους με πειραματικές μετρήσεις. Για το σκοπό αυτό πραγματοποιήθηκαν πειράματα σε αεροσήραγγα. Δεδομένου του ότι η τελευταία δεν διέθετε μοντελοποίηση του κινούμενου εδάφους, τα CFD τρεξίματα επαναλήφθησαν με ακίνητο έδαφος αυτή τη φορά και υψηλότερη ταχύτητα εισόδου, ίση με αυτή του πειράματος. Τα συμπεράσματα της σύγκρισης κατέληξαν στο οτι τα μοντέλα $k-\omega$ SST και Spalart-Allmaras πλησιάζουν με αρκετά ικανοποιητική ακρίβεια τα πειραματικά αποτελέσματα.

7.4 Επίλυση του Συζυγούς Προβλήματος

7.4.1 Χάρτες Ευαισθησίας

Με βάση τα πεδία που προέκυψαν από την επίλυση του πρωτεύοντος προβλήματος με χρήση των τριών μοντέλων τύρβης έγινε επίλυση του συζυγούς προβλήματος. Ακολουθώντας τη διαδικασία που περιγράφηκε στο κεφάλαιο 2 είναι δυνατόν να υπολογισθεί η κλίση της αντικειμενικής συνάρτησης ως προς την κάθετη μετατόπιση των επιφανειακών κόμβων του πλέγματος. Γραφική απεικόνιση των παραπάνω παραγώγων επάνω στην επιφάνεια του οχήματος συνθέτει τον χάρτη ευαισθησίας του προβλήματος. Είναι προφανές οτι, ως απόρροια τριών διαφορετικών μεταξύ τους πεδίων ταχύτητας και πίεσης από τα τρία μοντέλα τύρβης, προκύπτουν αντίστοιχα τρία διαφορετικά πεδία συζυγών ταχυτήτων και πιέσεων και, άρα, τρείς διαφορετικοί χάρτες ευαισθησίας.

Σύγκριση των Τριών Χαρτών Ευαισθησίας

Ομοίως με το πρωτεύον πρόβλημα, ορισμένες βασικές παρατηρήσεις μπορούν να γίνουν με ένα πρώτο έλεγχο των τριών χαρτών, η βασική εκ των οποίων είναι η διαφορά του χάρτη ευαισθησίας που προέκυψε από το μοντέλο τύρβης $k-\epsilon$ σε σχέση με τους άλλους δύο. Στο σχήμα 7.12 φαίνεται η πλάγια πίσω όψη των τριών χαρτών ευαισθησίας, όπου με μπλέ είναι χρωματισμένες οι περιοχές που πρέπει να μετακινηθούν προς τα μέσα και κόκκινες οι περιοχές που πρέπει να ¨τραβηχθούν' προς τα έξω. Προς τα μέσα ορίζεται η κατεύθυνση από το ρευστό προς το στερεό όριο.

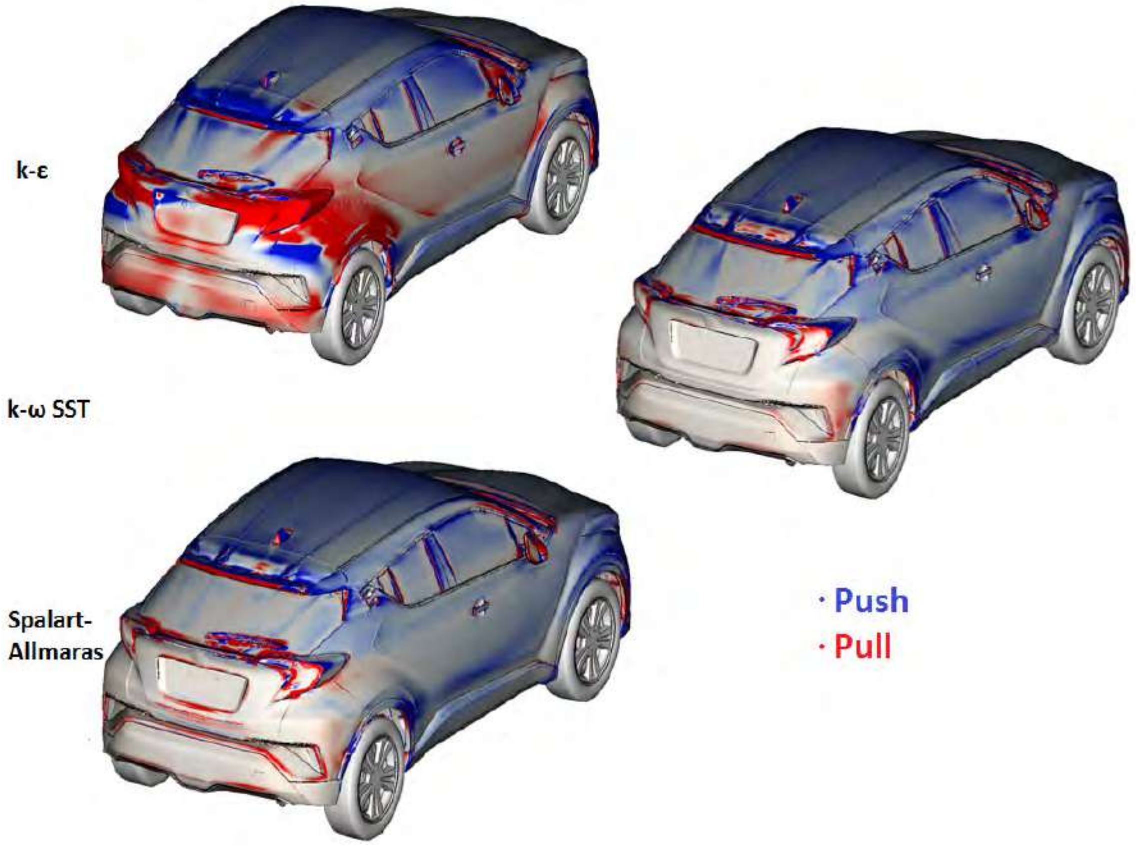

Σχήμα 7.12: *Σύγκριση των χαρτών ευαισθησίας από τα τρία μοντέλα τύρβης - Πίσω πλάγια όψη.*

Ποσοτικές διαφορές στο μέτρο της υπολογιζόμενης παραγώγου είναι υπαρκτές στο σύνολο της επιφάνειας του οχήματος και μεταξύ του συνόλου των χαρτών ευαισθησίας των τριών μοντέλων. Οι ποιοτικές όμως διαφορές, –οι οποίες εμφανίζονται μόνο μεταξύ του μοντέλου k-ϵ και των άλλων δύο– είναι συγκεντρωμένες στα πλαινά μέρη του οχήματος και, κυρίως, στο πίσω μέρος του, εκεί δηλαδή που εμφανίζονται έντονα τυρβώδη συνεκτικά φαινόμενα και αποκόλληση της ροής.

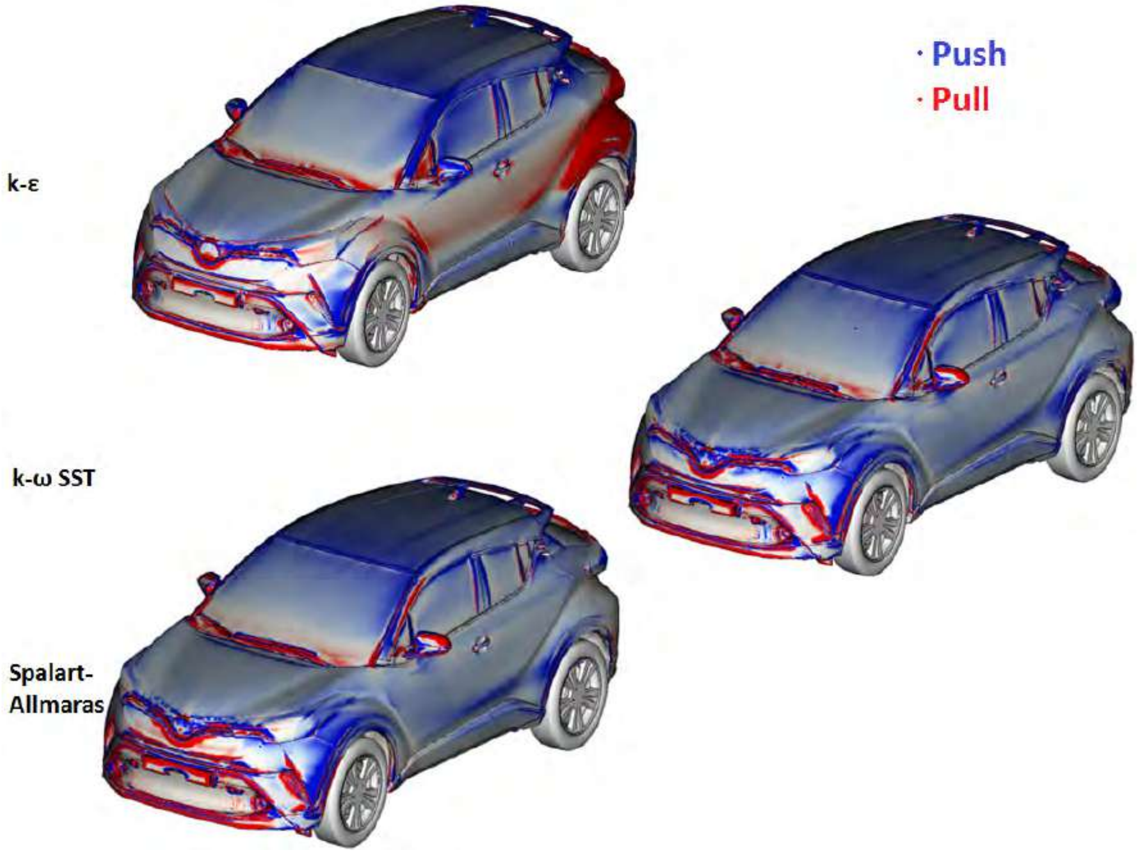

Σχήμα 7.13: *Σύγκριση των χαρτών ευαισθησίας από τα τρία μοντέλα τύρβης - Εμπρόσθια πλάγια όψη.*

Μια άλλη παρατήρηση που μπορεί να γίνει πάνω στους χάρτες αυαισθησίας είναι οτι οι παράγωγοι του μοντέλου $k - \epsilon$ είναι πολύ πιο έντονες (λαμβάνουν υψηλότερες τιμές) στο πίσω μέρος του αυτοκινήτου σε σχέση με τα άλλα δύο, που σημαίνει οτι όποια αλλαγή στο σχήμα του αυτοκινήτου πραγματοποιηθεί σε εκείνη την περιοχή, θα επιφέρει μεγάλη μεταβολή στο συντελεστή αντίστασης. Αυτό συμβαίνει διότι η ροή (όπως γίνεται εμφανές από το σχήμα 7.10) αποκολλάται και επαναπροσκολλάται σε μεγάλο εύρος του πίσω μέρους του αυτοκινήτου σύμφωνα με το μοντέλο τύρβης αυτό. Εκεί που λαμβάνει χώρα η αποκόλληση είναι και εκεί που αναμένεται να είναι και πιο μεγάλες οι τιμές των παραγώγων.

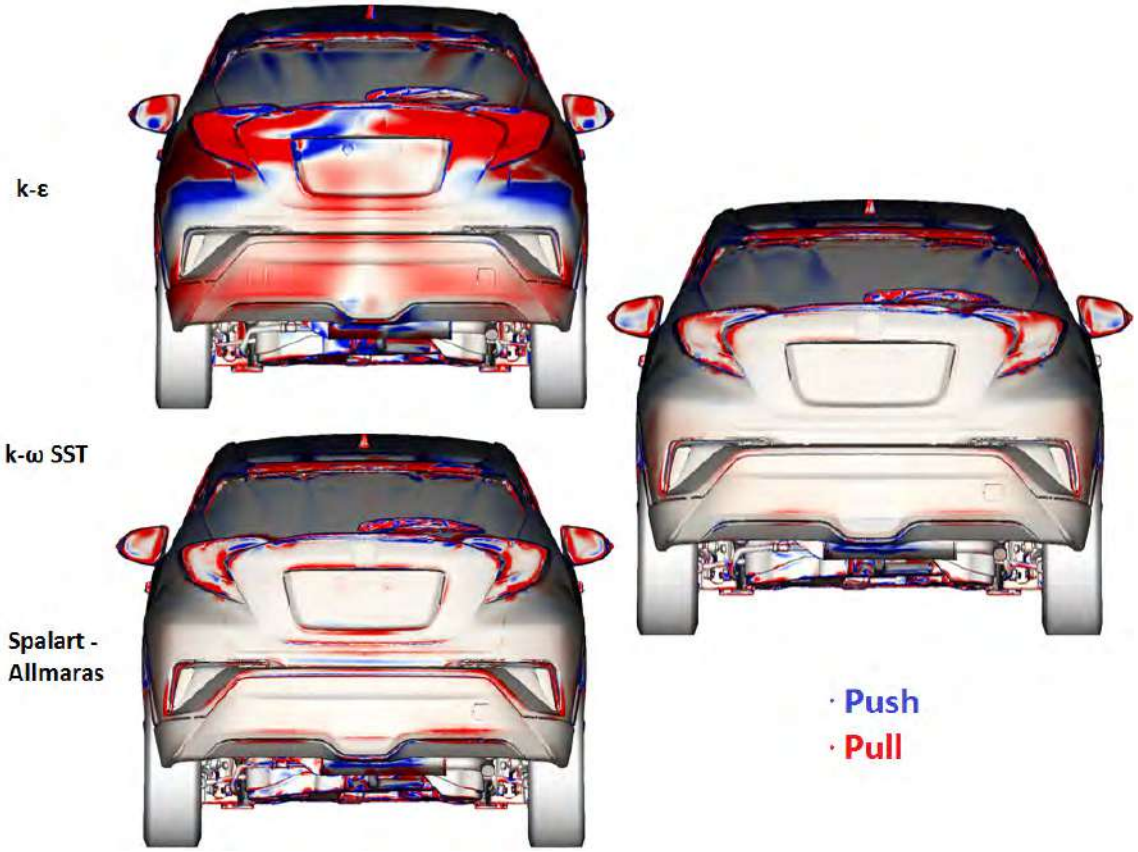

Σχήμα 7.14: *Σύγκριση των χαρτών ευαισθησίας από τα τρία μοντέλα τύρβης - Πίσω όψη.*

Καταλήγοντας, αξίζει να αναφερθεί η έντονη ασυμμετρία του χάρτη ευαισθησίας από το μοντέλο τύρβης $k - \epsilon$, η οποία ακολουθεί το μοτίβο του πρωτεύοντος προβλήματος του οποίου τα πεδία είναι επίσης μη-συμμετρικά ως προς το XZ επίπεδο. Μπορεί μάλιστα να γίνει ο ισχυρισμός οτι τα συζυγή πεδία οξύνουν την όποια ασυμμετρία μπορεί να υπάρχει στα πεδία που προκύπτουν από την επίλυση του πρωτεύοντος προβλήματος. Αυτό διαφαίνεται και στο σχήμα 7.15, όπου στο πάνω μέρος φαίνεται, σε κάτοψη, η στατική πίεση στην επιφάνεια του αυτοκινήτου ενώ, στο κάτω μέρος, η συζυγής πίεση, μεταξύ των οποίων παρατηρείται αύξηση της ασυμμετρίας.

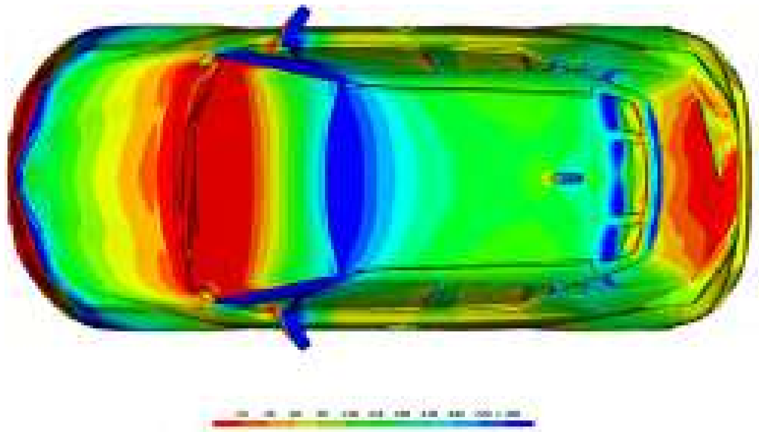

(α΄) Στατική πίεση

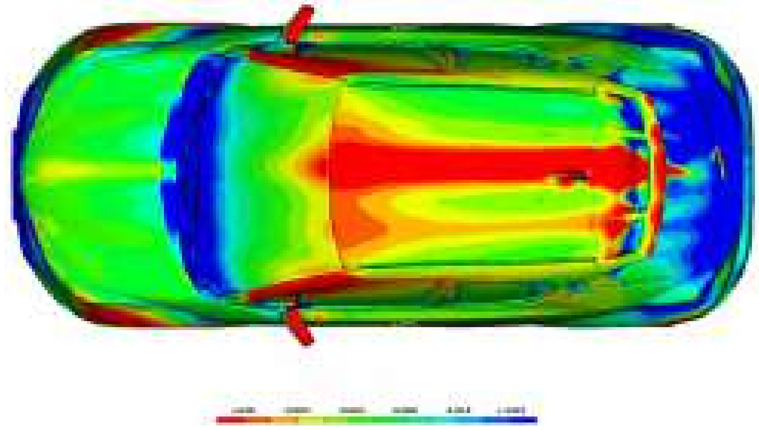

(β΄) Συζυγής πίεση

Σχήμα 7.15: *Σύγκριση των κατανομών στατικής και συζυγούς πίεσης - Κάτοψη - μοντέλο τύρβης Spalart Allmaras.*

7.5 Βελτιστοποίηση Μορφής του Αυτοκινήτου μέσω CFD

Κατόπιν της δημιουργίας και ανάλυσης των χαρτών ευαισθησίας από τα τρία μοντέλα τύρβης έγινε εντοπισμός των περιοχών που φαίνεται να έχουν τη μεγαλύτερη επίδραση στη μείωση του συντελεστή αντίστασης. Αυτό οδήγησε στην επιλογή ορισμένων περιοχών οι οποίες μορφοποιήθηκαν και βελτιστοποιήθηκαν με τον μορφοποιητή πλέγματος της ΜΠΥΡ&Β/ΕΜΠ. Τα αποτελέσματα μίας βελτιστοποίησης θα παρουσιαστούν στη συνέχεια.

Όπως έχει ήδη γίνει σχετική αναφορά, ο μορφοποιητής του πλέγματος ο οποίος λειτουργεί αυτοματοποιημένα σε συνδυασμό με τον επιλύτη του πρωτεύοντος και συζυγούς

προβλήματος απαιτεί ορισμένες βασικές ρυθμίσεις από την πλευρά του χρήστη. Ακολούθως, έπειτα από κάθε μεταβολή του πλέγματος εκτελείται κατάλληλος έλεγχος για την ποιότητα του παραγόμενου πλέγματος.
Οι ρυθμίσεις που απαιτούνται από την πλευρά του χρήστη αφορούν τα εξής:

- Αριθμός των σημείων ελέγχου των ογκικών B–Splines σε κάθε κατεύθυνση.
- Βαθμός των συναρτήσεων βάσης
- Προαιρετικός περιορισμός της μετακίνησης συγκεκριμένων σημείων ελέγχου προς συγκεκριμένες κατευθύνσεις.

Η τελευταία παράμετρος είναι ιδιαίτερα χρήσιμη για εφαρμογές βελτιστοποίησης μορφής, τόσο για προβλήματα εξωτερικής όσο και εσωτερικής αεροδυναμικής. Περιορισμοί σχεδιασμού σε εξωτερική αεροδυναμική ή γεωμετρικών προδιαγραφών σε εσωτερική αεροδυναμική αφήνουν πολλές φορές ελάχιστα περιθώρια μεταβολής της γεωμετρίας. Εξυπακούεται οτι, στις περιπτώσεις αυτές, επιβάλλονται συγκεκριμένοι περιορισμοί στην κίνηση των σημείων ελέγχου για τον βέλτιστο έλεγχο της τελικής γεωμετρίας.

Στη βελτιστοποίηση που θα ακολουθεί χρησιμοποιήθηκαν δύο κουτιά ελέγχου –δηλαδή δομημένα πλέγματα σημείων ελέγχου των ογκικών B–Splines– που παραμετροποιούν την επιφάνεια του οχήματος στην περιοχή του εμπρόσθιου προφυλακτήρα. Συνολικά αποτελούνταν από 7X9X7 σημεία ελέγχου ενώ οι συναρτήσεις βάσης ήταν τρίτου βαθμού και στις τρεις διευθύνσεις. Το πλέγμα ελέγχου των σημείων ελέγχου φαίνεται παρακάτω στα σχήματα 7.16(α′) και 7.16(β′). Το μοντέλο τύρβης που χρησιμοποιήθηκε ήταν το Spalart-Allmaras.

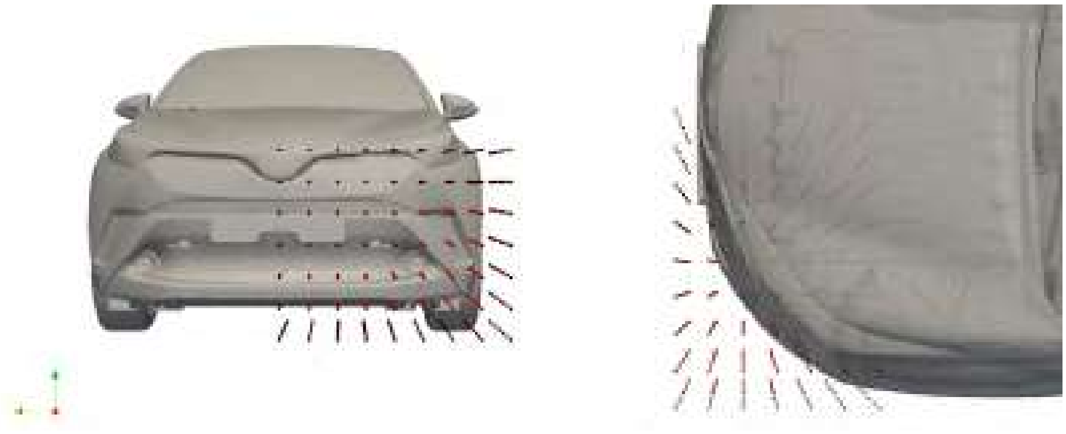

(α′) Μπροστά όψη

(β′) Κάτοψη

Σχήμα 7.16: *Δομημένο πλέγμα σημείων ελέγχου των ογκικών B–Splines.*

Πραγματοποιήθηκαν δύο κύκλοι βελτιστοποίησης με σχήματα διακριτοποίησης δεύτερης τάξης τόσο για τις εξισώσεις του πρωτεύοντος όσο και για αυτές του συζυγούς προβλήματος. Η συνολική μείωση του συντελεστή αντίστασης ήταν της τάξης του 2%, όπως φαίνεται παρακάτω στο σχήμα 7.17.

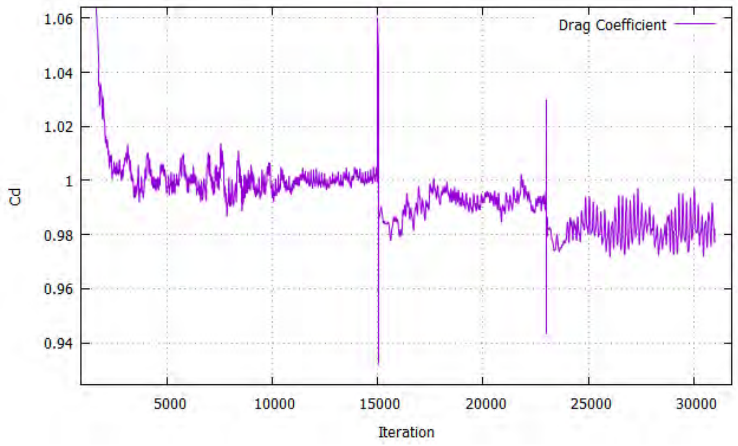

Σχήμα 7.17: *Διάγραμμα σύγκλισης του συντελεστή αντίστασης κατά τις επαναλήψεις του επαναληπτικού αλγορίθμου επίλυσης.*

Ακόμη, η σύγκλιση των εξισώσεων του πρωτεύοντος και συζυγούς προβλήματος φαίνεται στα σχήματα 7.18(β′) και 7.18(α′) που ακολουθούν.

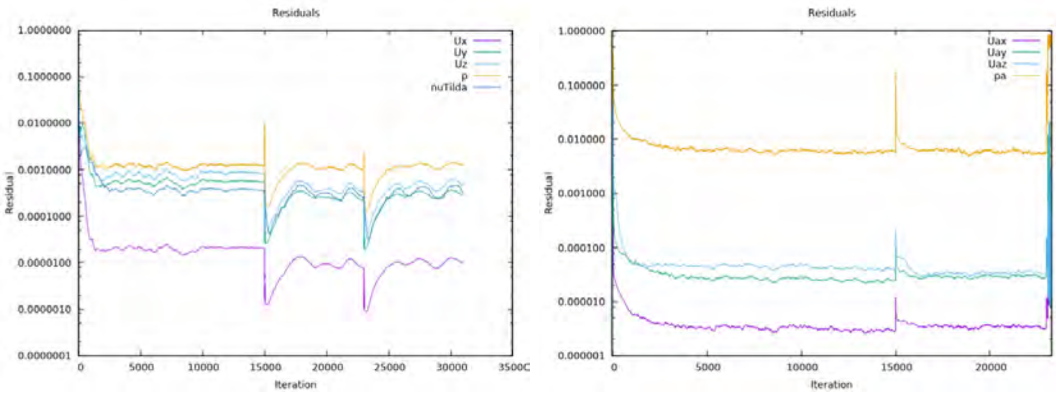

(α′) (β′)

Σχήμα 7.18: *Διάγραμμα σύγκλισης των εξισώσεων της ροής (αριστερά) και των συζυγών εξισώσεων (δεξιά) κατά τη βελτιστοποίηση.*

Η τελική γεωμετρία φαίνεται παρακάτω στο σχήμα 7.19, ενώ στο σχήμα 7.20 φαίνεται χρωματισμένη κατάλληλα η επιφάνεια του οχήματος ανάλογα με το μέτρο της μετατόπισης των επιφανειακών σημείων του πλέγματος. Στο σχήμα αυτό, με κόκκινο φαίνονται χρωματισμένες οι περιοχές οι οποίες παραμορφώθηκαν περισσότερο ενώ με μπλέ αυτές που παρέμειναν πρακτικά ακίνητες.

Σχήμα 7.19: *Σύγκριση αρχικής και βελτιωμένης γεωμετρίας - Μπροστά όψη - Βελτιωμένη γεωμετρία στα δεξιά του σχήματος.*

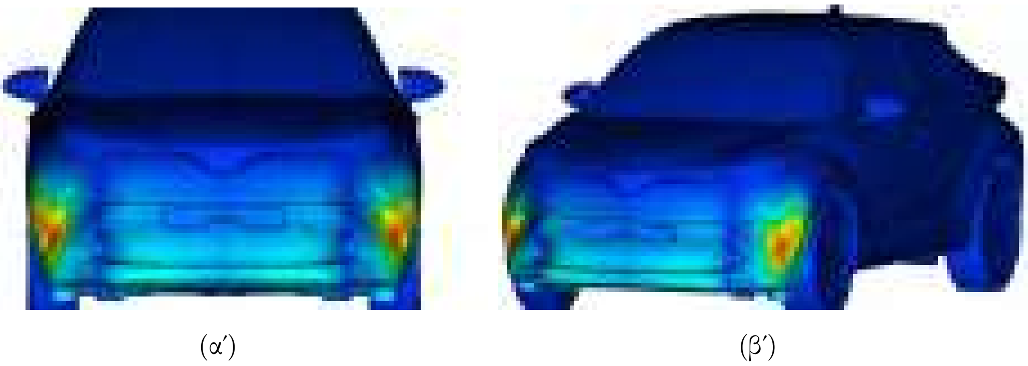

(α′) (β′)

Σχήμα 7.20: *Ένταση της κίνησης των σημείων της επιφάνειας του αυτοκινήτου κατά τη βελτιστοποίηση. Αριστερά - εμπρόσθια όψη. Δεξιά - πλάγια εμπρόσθια όψη.*

Το τελικό σχήμα είναι αρκετά ομαλό χωρίς ατέλειες ή ασυνέχειες ενώ η μέγιστη μετατόπιση του πλέγματος ήταν περίπου 2 εκατοστά.

7.6 Ανακεφαλαίωση–Συμπεράσματα

Στη διπλωματική αυτή εργασία πραγματοποιήθηκε βελτιστοποίηση μορφής ενός επιβατικού αυτοκινήτου με χρήση της συνεχούς συζυγούς μεθόδου, η οποία έχει αναπτυχθεί από τη ΜΠΥΡ&Β/ΕΜΠ, με στόχο την ελαχιστοποίηση του συντελεστή αντίστασής του.

Αρχικά πραγματοποιήθηκε ανάλυση της ροής γύρω από το υπό εξέταση αυτοκίνητο στο περιβάλλον ανοιχτού λογισμικού OpenFOAM®. Το πρόβλημα διέπεται από τις εξισώσεις RANS για ασυμπίεστο ρευστό και χρονικά μόνιμη, τυρβώδη ροή, ενώ η επίλυση τους έγινε με χρήση μίας παραλλαγής του επαναληπτικού αλγορίθμου SIMPLE. Έγινε χρήση τριών μοντέλων τύρβης, του $k-\epsilon$, του $k-\omega$ SST και του Spalart-Allmaras και σύγκριση των αποτελεσμάτων με βάση την ακρίβεια του καθενός στην ακριβή πρόλεξη του συντελεστή αντίστασης και των πεδίων ταχύτητας, πίεσης και τυρβώδους κινηματικής συνεκτικότητας. Παράλληλα, έγινε σύγκριση των αποτελεσμάτων των προσομοιώσεων με μετρήσεις από πειράματα τα οποία διεξήχθησαν σε αεροσήραγγα. Αποτέλεσμα της σύγκρισης ήταν οτι το μοντέλο $k-\epsilon$ υστερεί των άλλως δύο σε ότι αφορά τα παραπάνω σε προβλήματα εξωτερικής αεροδυναμικής, ενώ ο συντελεστής αντίστασης από το μοντέλο αυτό ήταν 7% υψηλότερος από τα άλλα δύο.

Στη συνέχεια, με βάση τις λύσεις των τριών μοντέλων ακολούθησε επίλυση του συζυγούς προβλήματος. Έγινε υπολογισμός των παραγώγων ευαισθησίας, των παραγώγων δηλαδή της οπισθέλκουσας του αυτοκινήτου ως προς την κάθετη μετατόπιση των επιφανειακών κόμβων του πλέγματος και, στη συνέχεια, δημιουργία των αντίστοιχων χαρτών ευαισθησίας. Έγινε σύγκριση των χαρτών ευαισθησίας από τα τρία μοντέλα τύρβης και στη συνέχεια, σύμφωνα με αυτούς, επιλέχθηκαν και βελτιστοποιήθηκαν μεμωνομένες περιοχές του αυτοκινήτου. Πέραν αυτού, στο πλήρες κείμενο της εργασίας αυτής σχολιάστηκαν θέματα που σχετίζονται με τη σύγκλιση και την ευστάθεια κατά την αριθμητική επίλυση του συζυγούς προβλήματος, τη συμμετρία των αποτελεσμάτων και την ακρίβεια των υπολογισμών. Σύγκριση των χαρτών ευαισθησίας οι οποίοι κατασκεύαστηκαν έπειτα από επίλυση του προβλήματος ροής με πρώτης και δεύτερης τάξης ακρίβειας σχήματα διακριτοποίησης έδειξε ότι η τελευταία παίζει σημαντικό ρόλο στον ακριβή υπολογισμό των παραγώγων και μπορεί να οδηγήσει ακόμα και σε λανθασμένο πρόσημο αυτών. Η λήψη μέσων τιμών πάνω σε σημαντικό αριθμό επαναλήψεων της λύσης του πρωτεύοντος προβλήματος -αφότου ο επαναληπτικός αλγόριθμος έχει συγκλίνει- αποδείχθηκε να συμβάλλει στην αύξηση της συμμετρίας της λύσης καθώς επίσης και στη σύγκλιση του συζυγούς προβλήματος. Τέλος, το συζυγές πρόβλημα φάνηκε να ενισχύει την όποια ασυμμετρία υπάρχει στο πρωτεύον πρόβλημα καθώς επίσης και τις διαφορές μεταξύ των αποτελεσμάτων από τα τρία μοντέλα τύρβης.

Τέλος, με βάση τις ενδείξεις από τους χάρτες ευαισθησίας επιλέχθηκαν αποσπασματικά περιοχές του αυτοκινήτου με υψηλή ευαισθησία ως προς τη μείωση του συντελεστή αντίστασης και βελτιστοποιήθηκαν με χρήση του αυτόματου λογισμικού μορφοποίησης, το οποίο έχει αναπτυχθεί από τη ΜΠΥΡ&Β/ΕΜΠ. Τα αποτελέσματα έδειξαν ότι ακόμη και μικρός αριθμός κύκλων και περιορισμένη μετακίνηση των επιφανειακών κόμβων οδηγεί σε αξιοσημείωτη μείωση του συντελεστή αντίστασης. Βελτιστοποίηση του εμπρόσθιου προφυλακτήρα κατέληξε σε 2% μείωση του C_D με μέγιστη μετατόπιση των σημείων του CFD πλέγματος μικρότερη των 2cm. Επισημαίνεται ότι, στο πλαίσιο της διπλωματικής αυτής εργασίας έγινε επέκταση του λογισμικού μορφοποίησης σε ότι αφορά την ελευθερία κίνησης των σημείων ελέγχου των ογκικών B–Splines.

Βιβλιογραφία

[1] D. Hummel, *On the vortex formation over a slender wing at large angles of incidence*, AGARD-CP-247, Paper 15, 1978.

[2] S.r Ahmed, G. Ram, G. Faltin, *Some salient features of the time averaged ground vehicle wake*, Dokumentation Kraftfahrtwesen e.V. 1984.

[3] J. D. Anderson, Jr. *Fundamentals of Aerodynamics, Second Edition. McGraw-Hill*, 1991.

[4] W. Anderson, V. Venkatakrishnan, *Aerodynamic design optimization on unstructured grids with a continuous adjoint formulation.*, Institute for Computer Applications in Science and Engineering (ICASE), 1997.

[5] P. R. Spalart, S. R. Allmaras, *A One-Equation Turbulence Model for Aerodynamic Flows*, 30th Aerospace Sciences Meeting and Excibit, Reno, NV, U.S.A. , 1992.

[6] F. R. Menter, *Zonal Two Equation k-ω Turbulence Models for Aerodynamic Flows*, AIAA Fluid Dynamics Conference, Orlando, FL, U.S.A. , 1993.

[7] F. R. Menter, *Two-Equation Eddy-Viscosity Turbulence Models for Engineering Applications*, AIAA Journal, Vol. 32, No.8, 1994.

[8] D. C. Wilcox, *Formulation of the k–ω Turbulence Model Revisited*, AIAA Journal, Vol 46, No 11, 2008.

[9] H. K. Versteeg, W. Malalasekera, *An Introduction to Computational Fluid Dynamics: The Finite Volume Method. Harlow, England: Pearson Education Ltd*, 2007.

[10] W. P. Jones, B. E. Launder, *The Prediction of Laminarization with a Two-Equation Model of Turbulence. International Journal of Heat and Mass Transfer, Volume 15, Issue 2*, 1972.

[11] B. E. Launder, B. I. Sharma, *Application of the Energy-Dissipation Model of Turbulence to the Calculation of Flow Near a Spinning Disc*, Letters in Heat and Mass Transfer, Vol. 1, Issue 2, 1974.

[12] E.M. Papoutsis–Kiachagias, *Adjoint Methods for Turbulent Flows, Applied to Shape or Topology Optimization and Robust Design.* PhD Thesis, NTUA, 2013.

[13] K.C. Giannakoglou, D.I. Papadimitriou, E.M. Papoutsis–Kiachagias, C. Othmer, *Adjoint methods in CFD-based optimization - Gradient computation & beyond.* ECCOMAS 2012–European Congress on Computational Methods in Applied Sciences and Engineering, pp. 8523-8539, 2012.

[14] E.M. Papoutsis–Kiachagias, K.C. Giannakoglou, C. Othmer, *Adjoint wall functions: Validation and application to vehicle aerodynamics Authors of Document.*. 11th World Congress on Computational Mechanics, WCCM 2014, 5th European Conference on Computational Mechanics, ECCM 2014 and 6th European Conference on Computational Fluid Dynamics, ECFD 2014, pp. 7593-7604, 2014.

[15] K.C. Giannakoglou, D.I. Papadimitriou, E.M. Papoutsis–Kiachagias, I.S. Kavvadias, *Adjoint methods for shape optimization and robust design in fluid mechanics.* OPT-i 2014 - 1st International Conference on Engineering and Applied Sciences Optimization, Proceedings, pp. 2252-2265, 2014.

[16] E.M. Papoutsis–Kiachagias, K.C. Giannakoglou, *Continuous Adjoint Methods for Turbulent Flows, Applied to Shape and Topology Optimization: Industrial Applications,* Archives of Computational Methods in Engineering, Volume 23, Issue 2, pp 255–299, 2014.

[17] E.M. Papoutsis–Kiachagias, A.S. Zymaris, I.S. Kavvadias, D.I. Papadimitriou, K.C. Giannakoglou *The continuous adjoint approach to the k–ϵ Turbulence model for shape optimization and optimal active control of turbulent flows.* Engineering Optimization, 47 (3), pp. 370-389, 2015.

[18] I.S. Kavvadias, E.M. Papoutsis–Kiachagias, G. Dimitrakopoulos, K.C. Giannakoglou, *The continuous adjoint approach to the k–ω SST turbulence model with applications in shape optimization.* Engineering Optimization, 47 (11), pp. 1523-1542, 2015.

[19] E.M. Papoutsis–Kiachagias, N. Magoulas, J. Mueller, C. Othmer, K.C. Giannakoglou, *Noise reduction in car aerodynamics using a surrogate objective function and the continuous adjoint method with wall functions.* Computers and Fluids, 122, pp. 223-232, 2015.

[20] E.M. Papoutsis–Kiachagias, K.C. Giannakoglou, *A parameterization and mesh movement strategy based on volumetric B-splines. Applications to shape optimization.* NTUA/PCOpt/2015/01 REPORT, Athens, Greece, 2015.

[21] K.C. Giannakoglou. Optimization Methods in Aerodynamics. Notes, National Technical University of Athens, 2005 (in Greek).

[22] D. Soban, *Review of Basic concepts*
The vocabulary of design